NMR studies of fluoropolymers and of polyaniline

Stefan A. Reinsberg

How to cite:

Reinsberg, Stefan A. (1998) NMR studies of fluoropolymers and of polyaniline. Masters thesis, Durham University.

NMR Studies of Fluoropolymers and of Polyaniline

by

Stefan A. Reinsberg

A thesis submitted in partial fulfilment of the requirements for the degree of Master of Science

University of Durham,
Department of Chemistry &
Department of Physics

1998

NMR Studies of Fluoropolymers and of Polyaniline

Stefan A. Reinsberg, Submitted for the degree of Master of Science, 1998

Abstract

This thesis presents a study of two polymers, poly(trifluoroethylene) (PTrFE) and polyaniline (PANi), by means of Nuclear Magnetic Resonance Spectroscopy (NMR).

The first part of the thesis focusses on investigations in connection with the fluoro polymer. Using known assignments of the fluorine solution-state spectrum the defect level could be determined as well as a high degree if atacticity confirmed. Solid-state NMR concentrated, on the one hand, on the detection of heterogeneities in the polymer and, on the other hand, on the investigation of cross-polarisation dynamics of abundant spin systems, namely $^{1}H \rightarrow {}^{19}F$ CP. To account for the two different kinds of fluorine in PTrFE a three-spin-bath model based on the usual spin-temperature approach has been developed, numerically investigated and applied to PTrFE. The success, however, was limited by the influence of coherent polarisation transfer in the early stage of the CP. The transient oscillations in $^{1}H \rightarrow {}^{13}C$ CP curves have been used in order to determine bond distances and, subsequently, to detect motion of the polymer chain. The onset of motion has been confirmed by comparing the measured axially symmetric fluorine shielding anisotropy tensor with the asymmetric tensor obtained from ab initio calculations carried out on the rigid molecule.

The second part is concerned with NMR of polyaniline with emphasis on proton wideline NMR of leucoemeraldine. Spin-lattice relaxation data inferred heterogeneity in the powder polymer with a fast relaxing component of about 5% intensity. Impurities as a source of this heterogeneity as well as partial crystallinity have been excluded on the basis of solution-state NMR results and X-ray results, respectively. Furthermore, proton spin-diffusion experiments suggest that the domains having different relaxation characteristics are in close contact, although no definite particle size has been determined. Experiments at elevated temperatures show an increase of the intensity of the fast relaxing component. A reversible transformation of regions with inherent motional heterogeneity has been inferred.

Memorandum

The Research presented in this thesis has been carried out in the Department of Chemistry and the Department of Physics, University of Durham, and in the Department of Physics, University of Leipzig, Germany, between October 1997 and October 1998. Unless stated otherwise it is the original work of the author. None of this work has been submitted for any other degree.

Acknowledgements

I would foremost like to thank my supervisor Professor R.K.Harris. I am indebted to him because of his constant guidance and support in all matters. My thanks are also extended to my supervisor Dr. Andy Monkman, whose useful advice and helpful suggestions are greatly appreciated.

Without Dr. Peter Holstein, whose help was invaluable during my stays at the Department of Physics in Leipzig, most of the work on polyaniline would not have been viable. His unselfish cooperation made the collaboration work. He opened my eyes to a more objective view on matters in NMR and life. I am thankful to Dr.Shinji Ando, who willingly shared his knowledge about polymers with me. He made nights at the spectrometer so enjoyable, with talks about Japanese culture and most of all cuisine (including the real thing).

I have been fortunate to work with Dr. Gustavo A. Monti, Dr. Eric Hughes, Dr. Jérôme Hirschinger, Dr. Alan Kenwright, Dr. Phil Adams and Barry Say, who helped me with their technical expertise.

I am grateful to Alison, Susan, Helen, Lindsey, Jonathan and Julian, who made life in the lab exciting, and patiently answered questions about life, the universe and everything. Of course, I have to thank Anna who read most of the thesis and polished its English.

I thank my family and Annegret for their help and support, which has made this one-year-stay in Durham possible. To them this thesis is dedicated ...

Contents

Introduction

Poly(trifluoroethylene) (PTrFE) belongs to the family of fluoropolymers, which are part of the group of electroactive polymers. The special interest in these substances is grounded in their electrical properties and their application in industry. Apart from poly(vinylidene fluoride) (PVDF), the most extensively studied system, the copolymer of trifluoroethylene and vinylidene fluoride has been the target of considerable research. PTrFE itself exhibits pyro- and piezo-electricity and also ferroelectricity, as shown by Oka and Kouzumi[OK83, OK84, OK85]. These properties are closely related to chemical and geometrical structure. The combined effort of NMR spectroscopists, crystallographers and polymer scientists is aimed at elucidating these structures in an attempt to further improve the features of these polymers.

Polyaniline (PAni) is the generic term given to the products of the oxidative coupling of aniline, which under certain conditions exhibit a high level of electrical conductivity. Because of the potential of an environmentally stable conducting polymer, it has been the subject of substantial scientific inquiry. Possible applications as a conductor with the processibility of a yoghourt pot catalyse research efforts into understanding the structure and conducting processes. One oxidation state of polyaniline is fully reduced leucoemeraldine base. Although this polymer is not conducting as is its partially protonated analogue, emeraldine base, it serves as a model substance because of its simpler structure.

These two organic polymers, PTrFE and PAni, are of very different nature considering their chemical structure, their properties and their possible application. However, questions put to the NMR spectroscopist are quite similar when asked to investigate these polymers. Solid-state NMR can reveal structural information on a scale ranging from a few Å to μm, thus complementing results obtained from other methods such as X-ray diffraction, transmission electron microscopy or UV/VIS spectroscopy. That is why the emphasis of this work has been on applying some of the innumerable experiments massaging the spin system under scrutiny.

The second chapter of this thesis is concerned with structural investigations of PTrFE. Solid-state peaks have been assigned using reported solution-state assignments. As is suggested by the knowledge about related fluoro compounds, heterogeneities due to partial crystallinity and different crystalline conformations are expected in PTrFE. These heterogeneities manifest themself in different levels of mobilities of the polymer chain in rigid and mobile domains. The ultimate aim was to detect these regions of different mobilities using methods already applied to PVDF by others[HSH97, HHS97]. The principles of these schemes are presented and the results of their application are analysed. As the selecting pulse sequences rely on different relaxation rates, which in turn show characteristic dependence on temperature, variable temperature experiments are presented as well. The high mobility of the polymer even below the glass transition is evidenced by a small linewidth and only marginal influence of proton decoupling on the fluorine spectrum. The nature of this mobility is investigated by comparing calculated and measured fluorine shielding anisotropy patterns.

Cross polarisation (CP) is undoubtedly one of the most widely used tools to enhance polarisation of rare nuclei with low magnetogyric ratios. Furthermore, it also plays a major role in determining structure and connectivity. That is why CP is also applied to the detection of nuclei without an obvious gain in signal intensity. Dipolar dephasing experiments and inversion-recovery CP experiments, well-known from $^{1}H \rightarrow ^{13}C$ CP, are applied to other pairs of nuclei. For that it is indispensable to understand the dynamics of the magnetisation transfer.

The dynamics of this process are well-understood for CP of rare nuclei, such as $^{1}H \rightarrow ^{13}C$ CP. However, systems with more than one abundant nuclide such as fluorinated polymers pose new questions, as they are not completely describable with the usual approach for CP dynamics. In most cases one can find features of two limits of polarisation transfer. On the one hand, coherent transfer, which has been observed in ferrocene and described by Müller et al.[MKBE74], governs the early stage of cross-polarisation dynamics. A number of authors used these techniques to measure heteronuclear couplings and hence distances[HH94, RHGG97]. On the other hand, CP in systems with sufficiently distributed heteronuclear coupling constants and fast spin diffusion is best described by a spin-temperature approach. This approach is justified if based on assumptions such as the dilution of the nuclei the magnetisation is transferred to.

Two circumstances complicate CP dynamics and analysis in fluoro compounds. Firstly, the superposition of coherent as well as incoherent transfer obscures the determination of cross-relaxation rates as well as spin-lattice relaxation times in the rotating frame from variable contact-time experiments. It is questionable whether these time constants can be understood in the same fashion they are used to characterise CP from abundant I to rare S spins. Secondly, the approximation of dilute S spins is not fulfilled. This and the coherent polarisation transfer mentioned above raise doubts about the validity of the spin-temperature approach.

The first part of chapter three tries to sketch the theoretical background of the CP experiment already known. The closer scrutiny of the assumptions for the spin-temperature approach is an attempt to outline the possible points of departure for a description of CP dynamics of abundant nuclei. A model of three spin baths, which is tailored to the situation of PTrFE, is then developed and analysed. In the second part of that chapter this model is applied to PTrFE and compared to analysis with the standard CP model. Also, coherent transfer in the $^{19}\mathrm{F} \rightarrow {}^{13}\mathrm{C}$ CP experiment at different temperatures is investigated in order to determine internuclear distances and detect motion.

The last chapter is devoted to polyaniline. Standard experiments such as solution-state carbon NMR and UV/VIS spectroscopy are applied to characterise the synthesised polymer. Using proton wideline NMR, motional heterogeneity is detected in leucoemeraldine base, a type of polyaniline. The source of this heterogeneity is investigated by trying to exclude possible reasons for this behaviour. Partial crystallinity can be detected by powder X-ray techniques. Spin-diffusion experiments monitor the diffusion of magnetisation over distances in the nm to μm scale. They can reveal whether the regions of interest are in contact on that sort of scale.

UV/VIS-spectroscopy shows that emeraldine base can be excited by light. It is known that this motion induces rapid ring rotation. As emphasised above, NMR is a unique tool to detect and characterise motion by measuring relaxation times strongly influenced by mobility of the nuclei in question and the parts of the molecule attached to it. An experiment has been devised which combines light excitation and observation of proton resonances of static emeraldine base films in collaboration with the Dr. Holstein, a member of the polymer physics group in Leipzig, Germany. The results of this experiment, which has the potential to be expanded, e.g. to measure life times of these excitated states, form the last part of that chapter.

The fundamentals of NMR are now very well-known, for application to both solutions and solids[Abr61, Meh83, Sli78, SM94, SRS94]. Consequently they will not be discussed in this dissertation, which will rather concentrate on the use of specific pulse sequences. However, experimental aspects of NMR, including brief descriptions of the spectrometers used to study the polymer systems in question, are given in Chapter one, below.

Chapter 1

Experimental

1.1 Nuclear Magnetic Resonance Experiments

1.1.1 CMX Spectrometer

Most of the NMR experiments have been done on a triple-channel Chemagnetics CMX 200 spectrometer, operating at 200.13 MHz for ^{1}H and 188.29 MHz for ^{19}F. Proton and fluorine spectra were recorded on a purpose-built HF probe, whereas carbon spectra were recorded on a triple-channel HFX probe.

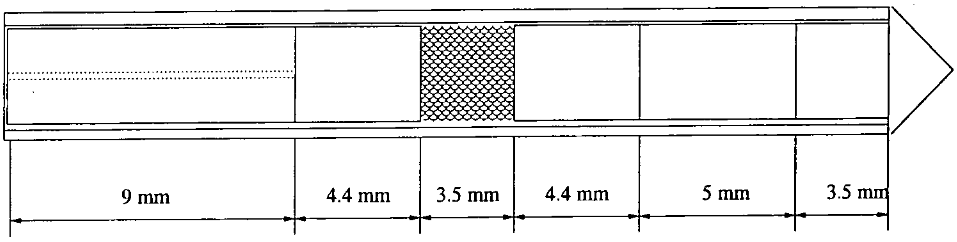

Figure 1.1: 4 mm o.d. pencil rotors used in the HF probe. Note the further confinement by the two 'inner' spacers of 4.4 mm length. This decreases the length of the sample from 12.3 mm down to 3.5 mm

A commercial (Chemagnetics) double-tuned APEX MAS probe for simultaneous ^{19}F and ^{1}H operation has been used. It accepts 4 mm o.d. zirconia rotors with drive tips made from vespel. Endcaps and spacers made from Teflon or Vespel were used depending on whether proton or fluorine spectra were recorded, respectively. The sample had to be confined in order to reduce the inhomogeneity in B_1 (see Figure 1.1), especially for the measurements of B_1-dependent relaxation parameters ($T_{1\rho}$, T_{HF} etc.). This causes a reduction in signal intensity by ca. 70%. According to

Hughes[Hug98], the sample confined in this way, is exposed to a B_1-field between 70 and 83 kHz, at maximum power. Without confinement a B_1-field spread from approximately 40 to 83 kHz, also at maximum power, occurs. In order to acquire an NMR response whilst decoupling on the other channel (frequency separation 6%) two ^{1}H and ^{19}F high-power bandpass filters were applied, additionally to the trap circuit in the probe.

For carbon observation, an HFX probe, in conjunction with 7.5 mm o.d. zirconia rotors, was utilised. For ^{1}H→ ^{13}C CP Kel-F drive tip and endcaps were used. In the case of ^{19}F→ ^{13}C CP Vespel drive tip and endcaps were used. Boron nitride spacers were always utilised. A high-power low-pass filter on the carbon channel and standard 200 MHz bandpass filters were applied. For carbon detection a further 100 MHz low-pass low-power filter was inserted between the earthed diodes and the first pre-amplifier.

Pulse durations for 90° pulses were set by adjusting the rf power on the amplifiers until the null signal for a 180° pulse was observed. The spectra were referenced according to the following table

	Referenced to	Via	Assumed chemical shift
^{1}H-spectra	TMS 0 ppm	PDMSO	0 ppm
^{19}F-spectra	$CFCl_3$ 0 ppm	C_6F_6	-166.4 ppm
^{13}C-spectra	TMS 0 ppm	adamantane	-33.8 ppm (high-freq.^{y} peak)

The two probes have been used at variable temperatures (VT). In order two achieve different temperatures in the sample, nitrogen gas is passed over it. The gas is cooled via a passage through a copper coil immersed in liquid nitrogen and is afterwards heated to the required temperature inside the variable-temperature stack. To operate the spectrometer at higher than ambient temperature the nitrogen gas is heated without prior cooling in liquid nitrogen. The temperatures quoted are temperatures measured by a thermocouple inside the VT stack. These nominal temperatures have not been calibrated.

The preparation of samples is explained in the respective chapters. Non-standard pulse-sequences are detailed elsewhere in this thesis.

1.1.2 MSL spectrometer

The static proton experiments on polyaniline were performed on a double-channel BRUKER MSL 100 spectrometer, operating at 100.13 MHz for ^{1}H. A static ^{1}H probe with high-power bandpass filters was utilised. The experimental setup for light excitation during NMR experiments is described in section 4.7.2. Referencing and setting of pulse durations were done as described in the preceding section.

1.1.3 Solution-State spectrometer

Solution-state ^{19}F NMR spectra were acquired using a Varian Inova 500 spectrometer operating at a fluorine frequency of 470 MHz. When ^{1}H-decoupling was applied, WALTZ-16 was used. Solution-state ^{1}H and ^{13}C NMR spectra were acquired on a Varian VXR-400S spectrometer operating at a frequency of 399.97 MHz for proton and 100.57 MHz for carbon. Again WALTZ-16 was utilised for proton decoupling. All experiments were done at ambient temperature, which was around 296 K.

1.2 X-ray Experiments

Two kinds of diffractometer have been used to acquire X-ray patterns:

The diffractometer working at lower voltages was a software-controlled Philips PW1050 powder X-ray system. The software was called 'Traces' and was produced by Diffraction Technology, Australia.

Higher intensities could be reached on an Enraf Nonius FR571 High Energy Rotating (molybdenum) Anode X-ray Generator, which was supplied with 60 kV accelerating voltage at a current of 300 mA current. The generator vacuum system was working at a vacuum pressure of 10^{-7} Torr (10^{-10} bar). The X-ray beam passed through a flat pyrolytic, Huber 151, single-crystal graphite monochromator. The image (2D Debye-Scherrer ring diffraction pattern) was collected on an image plate consisting of a 250 μm support layer under a 150 μm layer of photo-sensitive phosphor material covered by protective coating (10 μm) (FUJIUFILM imaging plate BAS-IP SR2040, produced by Fuji Photo-Film Co., Ltd.). The image plate was read by an image-plate reader (FUJIFILM BAS 1500) and transferred to a processing PC (software BASreader) to analyse the data further (software TINA v2.08e, raytest Isotopenmeßgeräte GmbH, Straubenhardt, Germany)). Samples were put into small capillaries (0.5 mm or 1.5 mm) and sealed if necessary. The capillaries were mounted on a sample holder, which was adjusted to the beam centre. In the case of poly(trifluoroethylene) bigger flakes of the substance were available. These could be directly mounted on the sample holder, thus avoiding amorphous background from the glass wall.

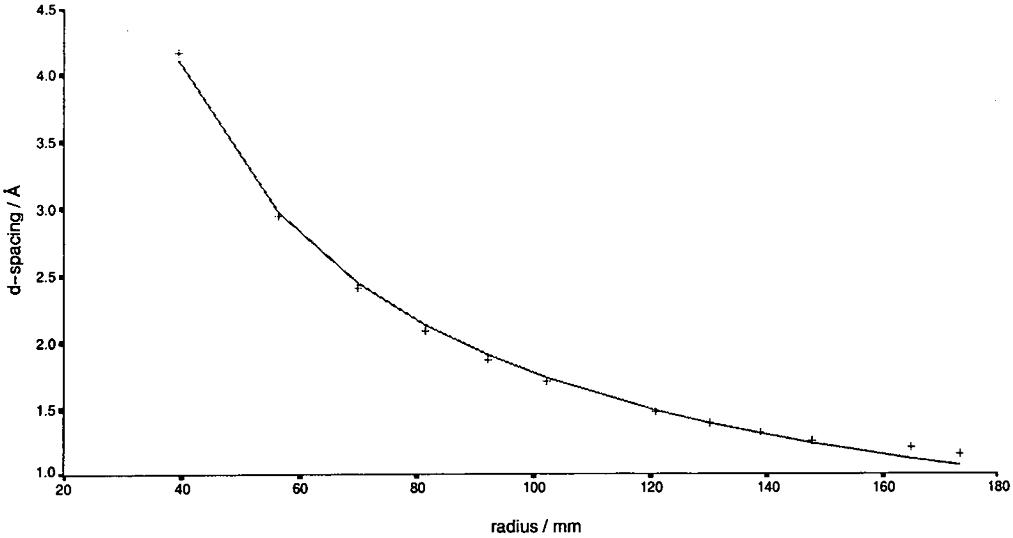

Figure 1.2: Plot of known d-spacing of LaB_6[Sut] vs. measured radii of diffraction rings. The fitted curve is an exponential function: d-spacing(r)=$115.35 \cdot r^{-0.90774}$

The reference sample was LaB_6. The pattern was measured under exactly the same conditions as for the actual samples. The recorded pattern (radius of diffraction ring) yielded, via known d-spacing, the dependence of d-spacing for the present experimental apparatus upon the measured radius. Figure 1.2 shows this dependence together with a fit, which has been used to determine the d-spacings of polyaniline and polytrifluoroethylene.

1.3 UV/VIS Spectroscopy

A series of UV/VIS spectroscopy experiments has been performed on films of polyaniline(PAni). The preparation of these films is described in section 4.2.1 and 4.2.2. The spectra were recorded with a Lambda 19 PERKIN ELMER UV/VIS/IR spectrometer. The spectrometer consists of two lamps, one for the visible/infra-red region and one for the ultraviolet region. The changeover between the two lamps was set to 319 nm. A background spectrum without the film and the substrate was obtained and was subtracted from the scan. The scan rate was 240 nm/min.

Chapter 2

Structural Investigation of PTrFE

Solid polytrifluoroethylene (PTrFE), which is a semicrystalline polymer, exhibits interesting electrical characteristics. Considerable effort has been made in order to investigate the electret properties of PTrFE [OK83, OK84, OK85]. Oka et al. performed X-ray and IR studies on PTrFE, which had undergone different crystallisation treatments. By rapidly quenching or slowly cooling, a polymer with a crystallinity ranging from 18 % to 46 % was produced[OK84].

There seems to be disagreement about the crystal structure and chain conformation of PTrFE: Tashiro et al.[TTK+84] proposed a disordered all-*trans* conformation with an orthorombic chain packing. These results were deduced from studies on ferroelectric phase transitions in copolymers of poly(vinylidene fluoride - trifluoroethylene) (P(VDF/TrFE)). A feature of these phase transitions was the final transformation on heating into a paraelectric phase, which can be observed for PTrFE at about 100-120 °C.

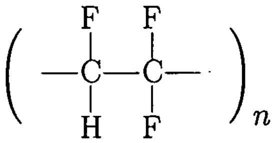

$\left(-\underset{H}{\overset{F}{C}}-\underset{F}{\overset{F}{C}}- \right)_n$

PTrFE

Lovinger et al.[LC84], however, claimed that PTrFE has a disordered conformation of TG, T$\overline{G}$, and TT groups and a hexagonal packing. The proposed structure was claimed to be analogous to the paraelectric phase of the P(VDF/TrFE) copolymers.

Oka et al.[OK86] disagree with both proposals for the following reason: The observed density of 2.026 g cm^{-3} exceeds the crystal density of PTrFE of 1.979 g cm^{-3}, based on Tashiro's structure and his crystal parameters. PTrFE is semicrystalline and the density of the amorphous phase is always *lower* than that of the crystalline phase. Therefore the average (observed) density must be *lower* than the crystal density. Oka concludes that the assumed crystal parameters, i.e. d-spacings, could be too small. On the other hand, Lovinger's structures gives reasonable results for the density and allows estimation of a crystallinity of ca 67 % (cf. X-ray result of 46 %). The problem with this structure is that it is nonpolar, like the paraelectric phases of P(VDF/TrFE). This contradicts findings by Oka and others.

Finally Oka et al.[OK86] postulated a structure which complies with density measurements and polar properties: The chain conformation should consist of T and G groups instead of being all-*trans*. The two crystalline phases which have been detected by X-ray and polarisation-current measurement were termed D- and S-phases. The S-phase is characterised by a single peak in the X-ray pattern, shows ferroelectric order and a comparatively high amount of polarisation. This phase especially occurs in quenched samples as it has a lower nucleation temperature than the D-phase. The latter is stable in slowly cooled PTrFE-samples and has been detected by a double peak in the X-ray spectrum. Both phases can be reversibly interconverted. This is particularly obvious in the polarisation-current experiment. As the electric field is lowered, the high-polarisation S-phase passes through partial depolarisation to the low-polarisation D-phase at zero field and further to a high-polarisation S-phase with reversed polarisation.

2.1 Solution-State NMR

In order to determine the chemical structure of PTrFE, solution-state NMR experiments have been performed (see sketch of chemical structure above). The sample was dissolved in deuterated acetone. Linewidths of viscous solutions of polymers tend to decrease if higher temperatures are used due to motional averaging. However, as the viscosity of the prepared PTrFE sample seemed low enough, experiments have been carried out at ambient temperature.

In Figure 2.1 the carbon spectra of the two available PTrFE samples are compared. As shown, no significant difference in the ^{13}C-spectra can be seen. The same applies for the comparison of proton and fluorine spectra (not shown). As expected, two major groups of peaks corresponding to the CFH-carbon and the CF_2-carbon can be observed ($\delta_C(CF_2) \approx 116$ ppm, $\delta_C(CFH) \approx 85$ ppm). Figures

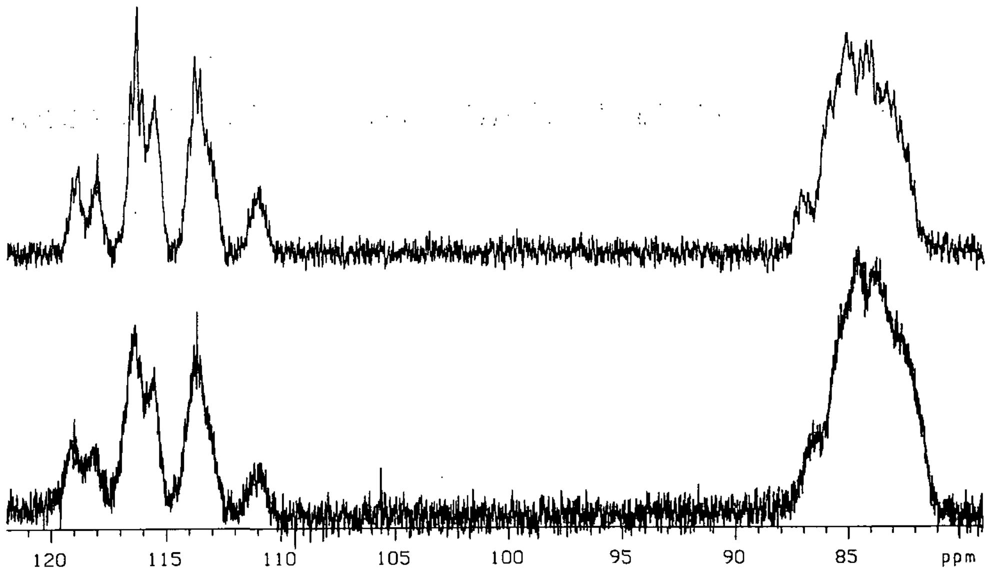

Figure 2.1: comparison of ^{13}C-spectrum of the ICI-sample(top) and the elf atochem sample(bottom) of PTrFE, ^{1}H-decoupled, referenced via acetone to the signal of TMS ($delta_C$=29.8 ppm)

2.2 and 2.3 show the ^{19}F-spectrum coupled and ^{1}H-decoupled, respectively. Tonelli et al.[TSC82], and Cais et al.[CK84] have attempted to assign the solution-state ^{19}F spectrum of PTrFE synthesised in their laboratory. Their prediction of chemical shifts based on the rotational isomeric state (RIS) approximation showed good agreement with their experimental data. They synthesised PTrFE by reductive dechlorination of Kel-F and thus obtained a highly regioregular polymer. Although we had an industrially synthesised polymer with supposedly high regioirregularity at our disposal, we can still base our assignments on the results of Tonelli, Cais and co-workers.

Two regions of peaks ascribed to the CF_2 fluorines (-128 to -117 ppm) and CFH fluorine (-219 to -208 ppm) should be noted. Peaks at lower frequencies of both groups are due to monomer inversion of the kind H-H:T-T. PTrFE, like other fluoro polymers, is atactic. The CF_2 resonance is sensitive to stereosequence dyads, therefore a singlet should be observed for the geminal fluorines in the racemic dyad. Tonelli [TSC82] predicts and observes that peak. At higher fields two peaks in this regions can be observed: -121.9 ppm and -122.1 ppm. The singlet is split because of sensitivity to tetrad stereosequences. The magnetically nonequivalent CF_2 fluorines give rise to an AB quartet with $J_{gem} \approx 300$ Hz. The peak positions for this quartet are -117.9 ppm, -118.5 ppm, -120.2 ppm and -120.9 ppm. The true chemical shifts can be calculated to be -118.2 ppm and 120.5 ppm.

As mentioned before, peaks at lower frequencies of the CFH group are due to inversions. More exactly, the peak at the lowest frequency (-218.7 ppm) arises from the racemic tail-to-tail fluorine. The meso fluorine causes a peak whose intensity is lower, so that we can infer a favoured racemic arrangement of the -CFH-CFH- units. RIS calculations predict a splitting of the stereo-regular peaks due to stereochemical triads, with pentad fine structure on the heterotactic and isotactic peaks. Six peaks, viz, -210.4 ppm (rr), -212.1 ppm (rm), -212.7 ppm (rm), -213.1 ppm (mm), -213.6 ppm (mm), -214.1 ppm (mm), can be assigned that way. Comparison of the fluorine spectrum of highly regioregular PTrFE with the spectrum of our sample suggests that the peaks at -208.2 ppm, -208.6 ppm, -211.1 ppm and -211.6 ppm arise from monomer inversions.

It is noteworthy to point out the small influence of proton decoupling. Only some fluorine resonances in the CFH region show this effect, for example at 210.4 ppm (J=34 Hz), 214.1 ppm (J=38 Hz).

Based upon the assignment of peaks an attempt has been made to estimate the defect level. The definition for the defect level given by Cais et al.[CK84] has been used. Three observationally distinct syndioregic CFH-centered regiosequence pentads can be found in PTrFE. The respective chemical shifts have been predicted by Tonelli et al.[TSC82] as follows:

A: -207...-210 ppm (-CF_2-CF_2-CFH-CF_2-CFH-),

B: -210...-214 ppm (-CFH-CF_2-CFH-CFH-CF_2-),

C: -215...-219 ppm (-CF_2-CF_2-CFH-CFH-CF_2-),

Peak integration yields the following approximated probabilities for regions A, B and C: A 1.5% , B 11.5% , C 7.5%. The total contribution of the -CFH- resonance area has to be normalised to 0.5. Following Cais' definition, the polymer present has a defect level of $\frac{1}{2}(1.5\% + 11.5\%) + 7.5\% = 13.5\%$

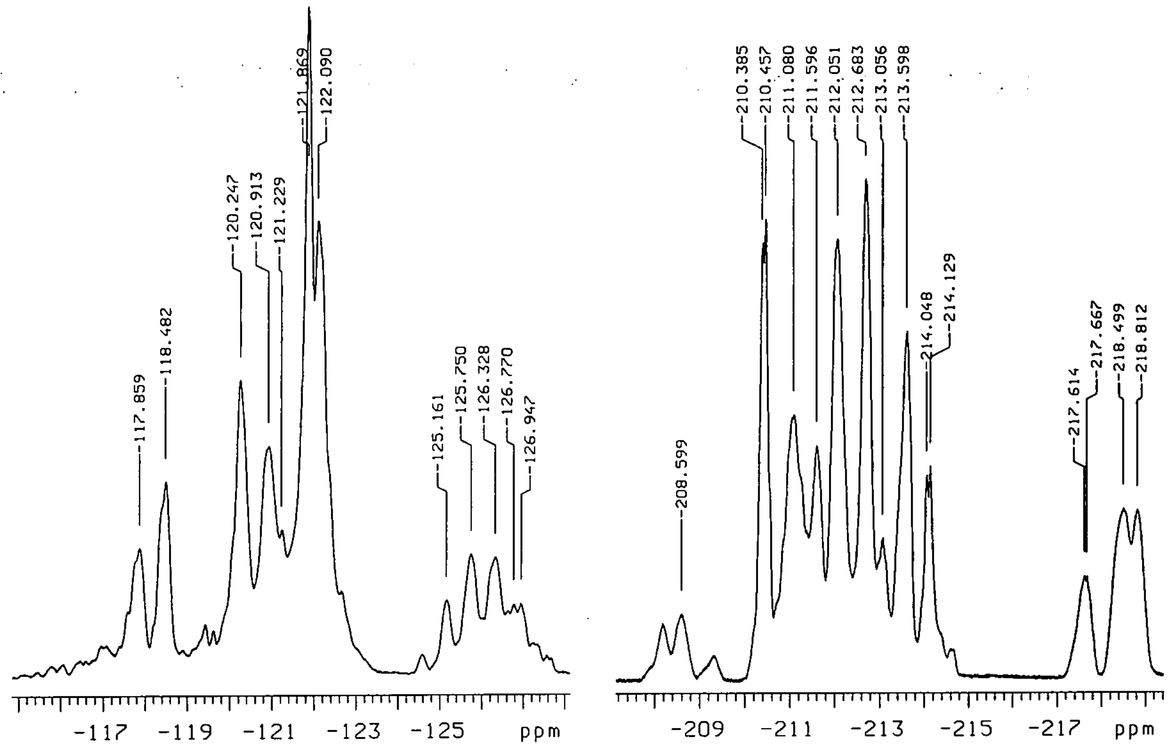

Figure 2.2: 470.2 MHz ^{19}F-spectrum of PTrFE without decoupling, referenced internally to $CFCl_3$

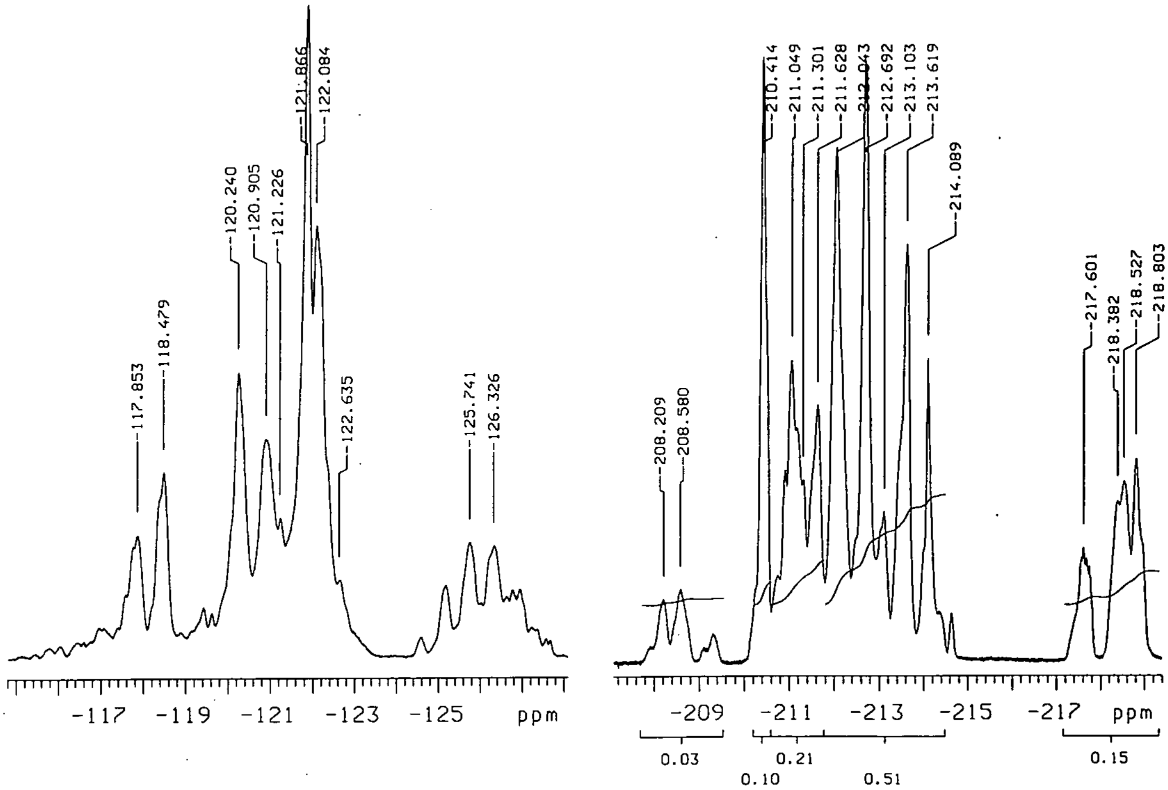

Figure 2.3: 470.2 MHz ^{19}F-spectrum of PTrFE with proton decoupling, referenced internally to $CFCl_3$

2.2 Solid-State NMR

Solution-state NMR can reveal valuable information about the chemical structure of compounds. However, to get insight into the stereochemical structure of the solid phase different methods must be used. To the author's knowledge only few solid-state NMR-studies on PTrFE have been reported. Slichter[Sli57] did motional studies on fluorine derivatives of polyethylene by measuring T_1, T_2 and $T_{1\rho}$ relaxation data for proton and fluorine in the temperature range 70...350 K . McBrierty et al.[MDF82] discussed the same relaxation parameters (for proton) and observed three relaxations in PTrFE.

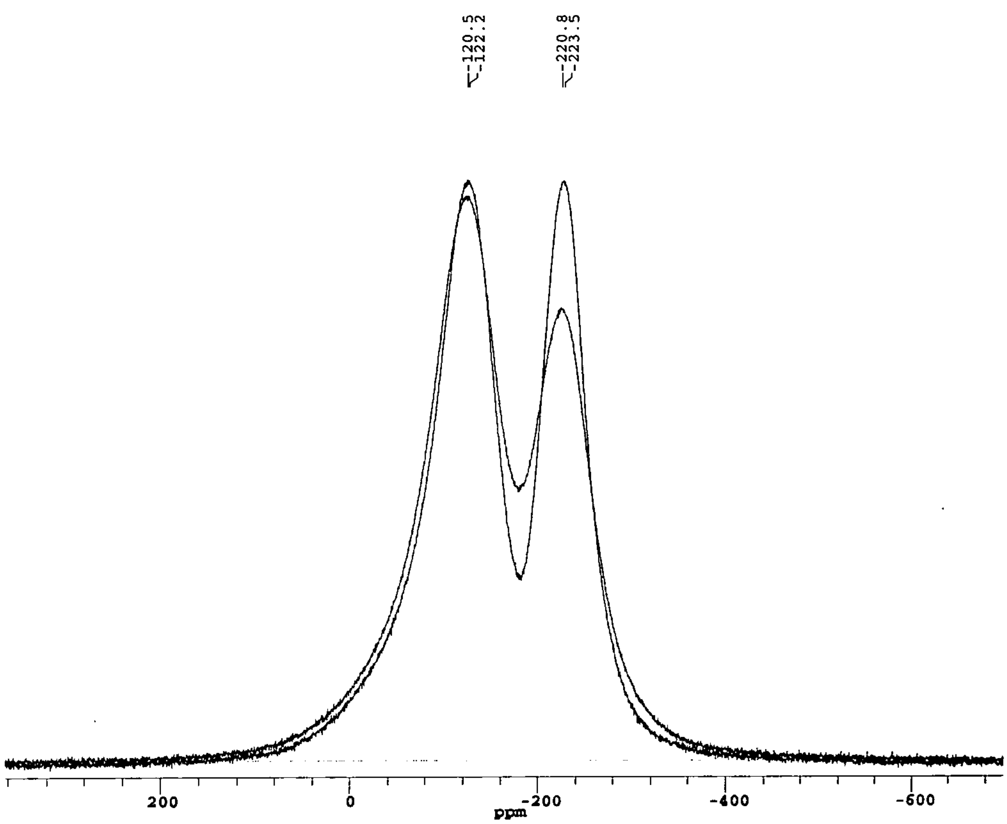

Figure 2.4: Static ^{19}F-spectrum with (top) and without (bottom) ^1H decoupling obtained under identical conditions and plotted in absolute intensity mode (spectrometer frequency 188.288 MHz, $B_1 \simeq 83$ kHz, dwell time 5 μs, 64 transients, recycle delay 2.5 s)

Figure 2.4 shows a static direct polarisation ^{19}F-spectrum of PTrFE. Proton decoupling narrows the lines only marginally. Naturally, the CFH peak is affected more by ^1H decoupling than the CF_2-peak. However, a considerable broadening of the lines remains. This broadening of the two peaks at 120 and 220 ppm must be mostly due to dipolar ^{19}F coupling and can be substantially suppressed by MAS as

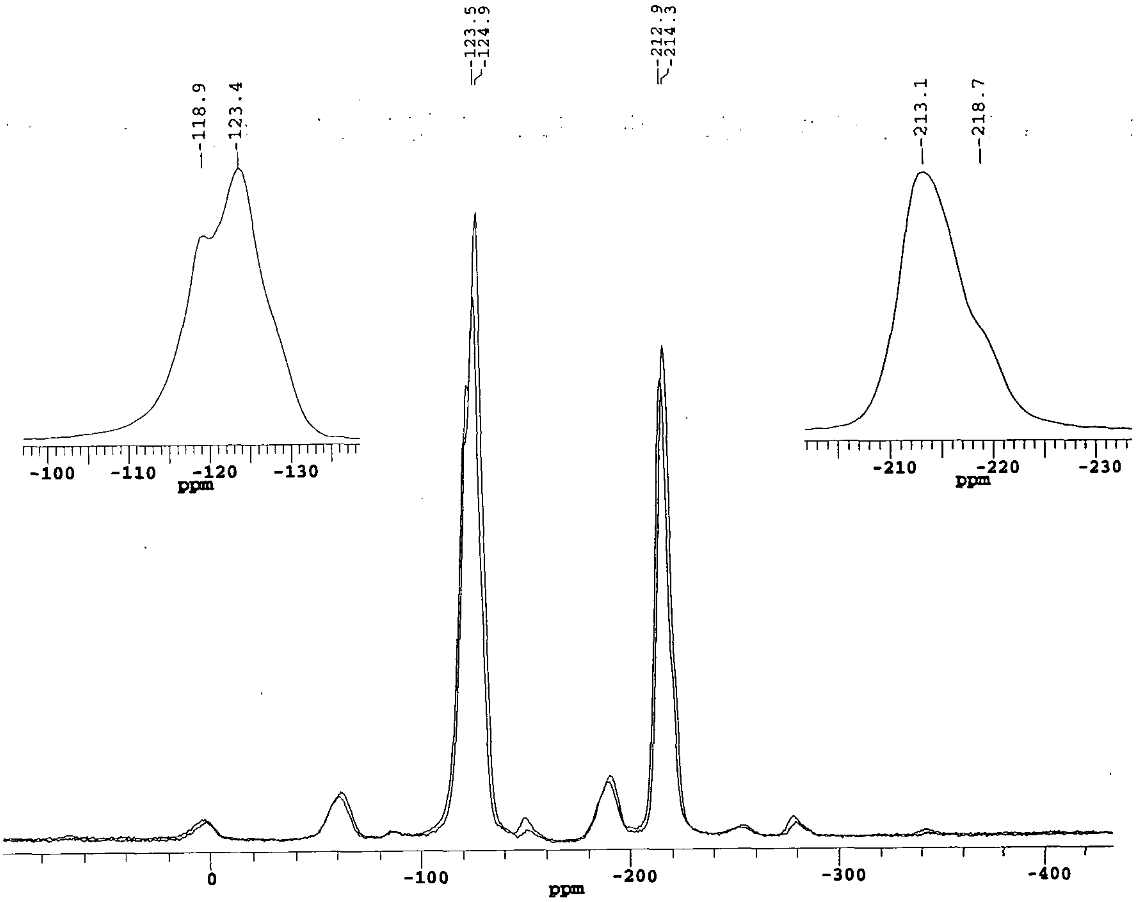

Figure 2.5: Direct polarisation ^{19}F-spectrum with (top) and without (bottom) ^{1}H decoupling under MAS 12 kHz (spectrometer frequency 188.288 MHz, $B_1 \simeq 83$ kHz, dwell time 10 μs, 16 transients, recycle delay 2.5 s). The insets show the CF$_2$-peak and the CFH-peak on the left and right, respectively, in greater detail (without decoupling)

shown in Figure 2.5.

Further examination of the fluorine spectrum reveals a small peak at -119 ppm (in the case of no decoupling). Also, a little shoulder (-127 ppm) shifted to lower frequencies of the peak at approximately -123 ppm can be seen. The separation of 4 ppm in both cases (ca. 750 Hz) is too big to be caused by J-coupling. The CFH-peak at -213 ppm is by the same account neither purely lorentzian nor purely gaussian because of a small shoulder at -219 ppm. Experience from studies on polyvinylidene fluoride (PVDF) suggests that these additional peaks could be due to conformational heterogeneities of PTrFE, e.g. different crystalline and amorphous phases. Also they could stem from a heterogeneous chemical chain-structure. This could well be, if one considers the approximate positions of peaks in the ^{19}F solution-state spectrum (see page 14). Thus, we would tentatively assign peaks in the solid-state spectrum as follows:

- -119 ppm: high frequency doublet of the AB quartet, which is due to sensitivity to stereosequence dyads; -123 ppm low-frequency doublet of the same AB quartet and singlet for fluorines in the racemic dyad; shoulder at ca. -127 ppm: head-to-head monomer inversions.
- -213 ppm: all peaks, which arise from isoregular fluorines; shoulder at -219 ppm: head-to-head monomer inversions.

In order to test the hypothesis of different domains within the polymer it is obviously desirable to select one of the phases to observe spectra of crystalline and amorphous regions separately.

It is interesting to note that ^{1}H decoupling has no influence on the spectrum obtained from the spinning sample. Only a Bloch-Siegert-shift of about 2 ppm to lower frequencies can be noted for the static as well as for the MAS case. (cf. double peak picking in Figure 2.5 on the main peaks)

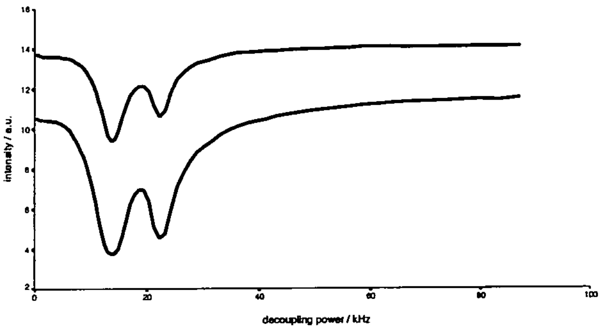

Figure 2.6: Peak intensity of CF_2(top) and CFH-peak(bottom) vs. proton decoupling power. Direct polarisation ^{19}F spectrum, MAS 12 kHz

Figure 2.6 shows how the intensity of the ^{19}F single-pulse spectrum changes with varying proton decoupling power. The decoupling power was changed in small but variable steps. The calibration of the digital power scale (running from 0 to 255) was done by measuring the duration of a π-pulse. The digital value 255 is equivalent to a B_1-field of 83 kHz. Two pronounced minima can be noted at ca. 12 kHz and 22 kHz. These minima are attributed to interference of spinning frequency (ν_r = 12 kHz) and frequency of the B_1-decoupling field.

Figure 2.7 shows a static spectrum of PTrFE recorded with an MREV-8 sequence. The transmitter spike which is still visible at 130 ppm (caused by an exponential decay of the FID baseline) has been removed by correcting the baseline. The pulse-sequence removes any homonuclear dipolar fluorine interaction and leaves us with the shielding anisotropy as the dominating line-broadening mechanism. We observe two well-defined axially symmetrical chemical shielding anisotropy (CSA) powder patterns.

The parameters of the CSA tensors are as follows:

CF_2-peak: δ_{iso}=-110 ppm, $\sigma_{\|}$=-147.5 ppm, $\sigma_{\perp}$=-35 ppm

CFH-peak: δ_{iso}=-210 ppm, $\sigma_{\|}$=-198.5 ppm, $\sigma_{\perp}$=-233 ppm

A slight effect of proton decoupling (not shown) can be noted. Without decoupling, the edges of the lineshapes are smeared out even more than they are under proton decoupling (Figure 2.7). However, broadening due to heteronuclear proton-fluorine coupling is still comparatively small (cf. Figure 2.4 showing static fluorine spectra of PTrFE).

To establish whether motion or inherent molecular geometry causes the observed axial symmetry of the powder patterns mentioned above, an attempt should be made to freeze out any possible motion and to repeat the experiment at low temperatures. Another approach to this problem was to determine the shielding parameters from ab initio calculations using Gaussian 94[GFT$^+$95]. The input structures were a syndiotactic and a regiotactic fluorinated alkane consisting of two monomer units and end-capped with CF_3 groups. Figure 2.8 shows the two optimised structures, which were the basis for the calculation. The geometrical structure was optimised with the 3-21G basis set. NMR parameters, as listed in the table below, were calculated with the larger polarised 6-31G* basis set, which is the recommended minimum basis set for calculating NMR shielding tensors[CTKF96].

It is interesting to note that the syndiotactic chain part turns out to be optimal at near *trans-trans* conformation, whereas the regiotactic polymer prefers *trans-gauche* conformation. Some of the shortest internuclear distances are given in Table 2.2.

Table 2.1 quotes the calculated shielding tensor values. Note that the reliability of relative shielding values is much higher than that of the absolute values. From Table 2.1 it can be seen that asymmetric fluorine shielding tensors should be observed. However, Figure 2.7 clearly shows that the expected asymmetries of 0.44 or 0.59 are higher than fitted. That indicates that an averaging process, possibly rotation about the molecular chain axis, must occur at ambient temperatures.

	CF_2			CFH		
	σ_{iso}	$\Delta\sigma$	η	σ_{iso}	$\Delta\sigma$	η
regiotactic	348	55	0.019	437	58	0.167
	362	106	0.590	442	52	0.419
syndiotactic	359	90	0.444	440	45	0.565

Table 2.1: Calculated shielding tensors for regiotactic and syndiotactic PTrFE. Note that the absolute shielding for $CFCl_3$ (0 ppm relative shift) is 195.6 ppm according to Hindermann et al.[HC68]. Definitions for shielding parameters are as follows: isotropic shielding $\sigma_{iso} = \frac{1}{3}(\sigma_{xx} + \sigma_{yy} + \sigma_{zz})$, anisotropy $\Delta\sigma = \sigma_{zz} - \frac{1}{2}(\sigma_{xx} + \sigma_{yy})$ and asymmetry $\eta = \frac{\sigma_{yy} - \sigma_{xx}}{\sigma_{zz}}$

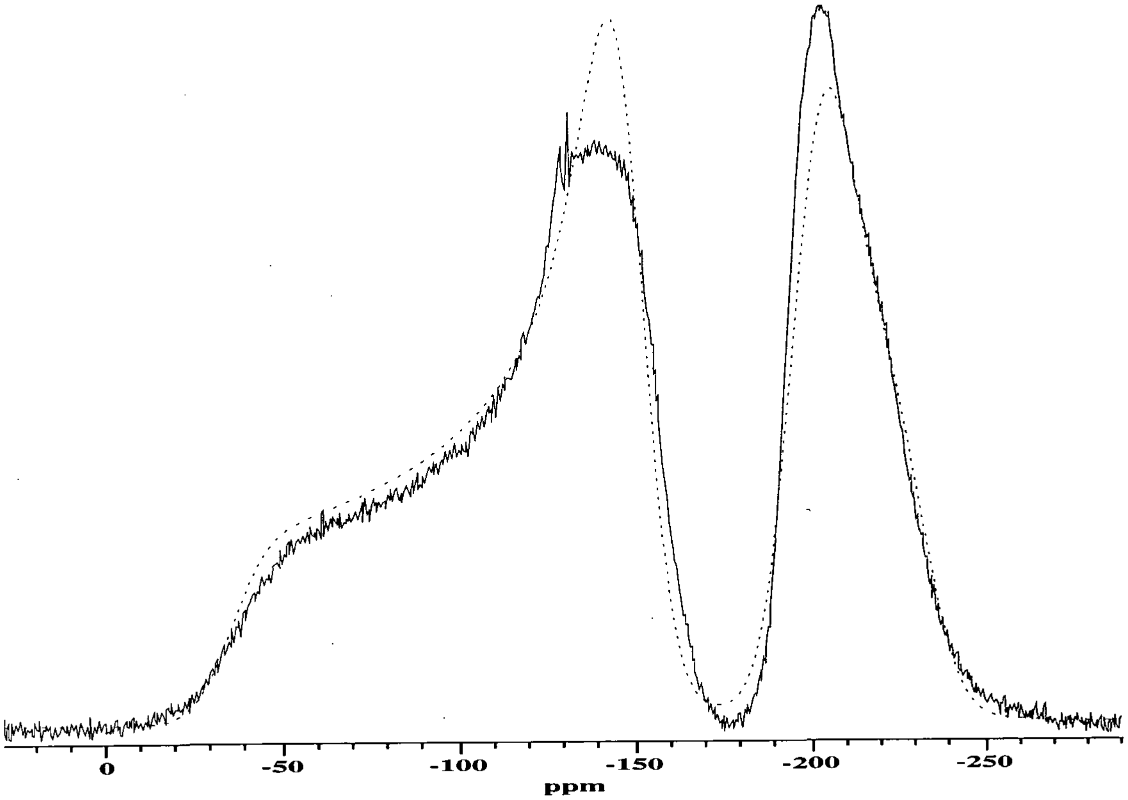

Figure 2.7: ^{19}F-MREV8-spectrum of PTrFE. The dashed line is the theoretical fit to the experimental lineshape (parameters see text) with 2000 Hz Gaussian linebroadening. 2048 points of FID. Experimental conditions were: pulse duration 1.4 μs, 64 scans, pulse delay 3 s, 512 points acquisition length, τ-delay 3 μs, proton decoupling with π-pulses on the proton channel (pulse duration 2.47 μs)

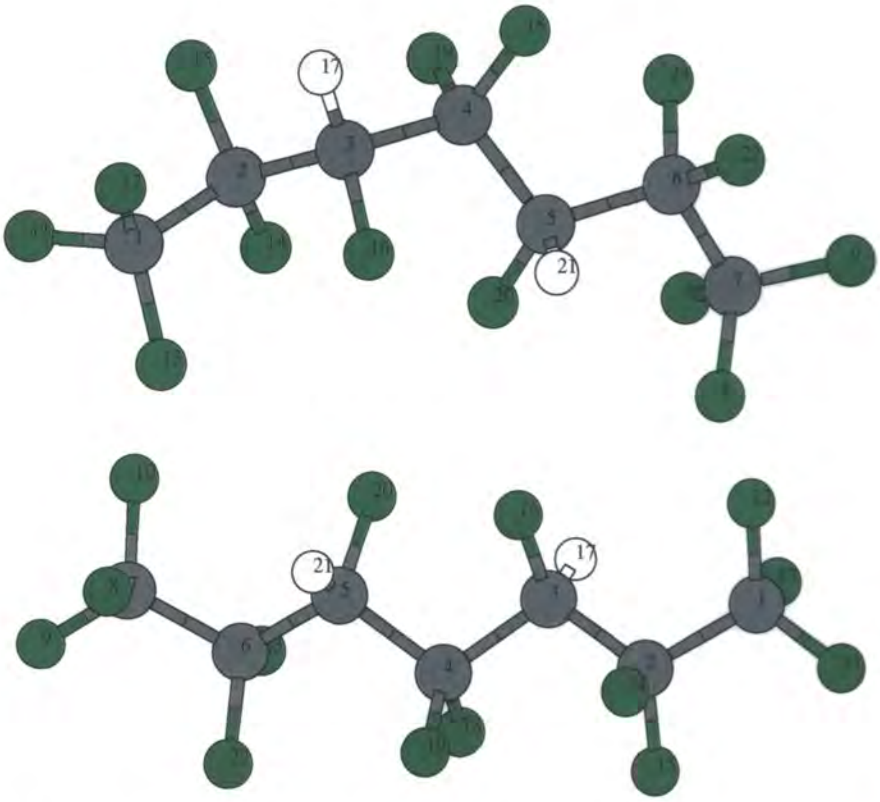

Figure 2.8: Calculated geometrical structure of a part of PTrFE as basis for shielding tensor calculation, top: regiotactic polymer, bottom: syndiotactic polymer

bond type	regiotactic polymer	syndiotactic polymer
carbon–proton	1.07	1.07
carbon–fluorine		
CFH	1.39	1.39
CF_2	1.36	1.36
proton-fluorine		
at CFH-site(e.g. 20-21)	2.022	2.035
next monomer(e.g. 16-21)	>2.23	2.498
same monomer/trans(e.g. 17-18)	2.357...2.826	2.450

Table 2.2: Table of selected calculated bond distances in syndiotactic and regiotactic PTrFE

2.2.1 Schemes of Selection

The selection methods mentioned in the preceding section have been exploited to a great extent in PVDF by Holstein and co-workers [HHS97]. Their bases are different relaxation efficiencies in different regions of the heterogeneous sample due to differences in mobility:

1. ^{1}H Spin-locking relaxation is slower for rigid regions than for amorphous ones.
2. Heteronuclear cross-relaxation (magnetisation transfer under Hartmann-Hahn match condition) is more effective for immobile regions.
3. Fluorine magnetisation of the rigid region dephases faster than that of the mobile region when not decoupled from protons.

Based on this knowledge experiments can be devised to select either the mobile or immobile region. The corresponding pulse sequences are depicted in the following graph 2.9.

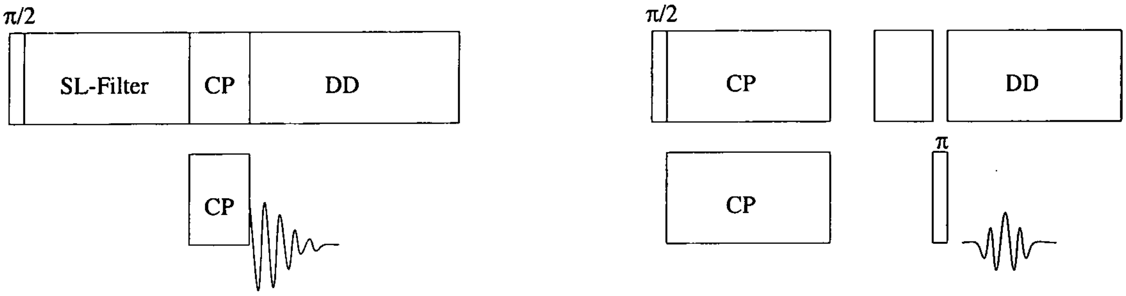

Figure 2.9: Pulse sequences which select phases of different mobilities: $T_{1\rho}$-filter selecting rigid regions (left) and dipolar dephasing experiment emphasising amorphous domains (right)

- The immobile (crystalline) region can be selected by a long proton spin-lock (cf. 1.) prior to a short cross polarisation time (cf. 2.), the so called $T_{1\rho}$-filter. However, the cross-polarisation time has to be chosen so that spin diffusion between different domains is avoided as well as sufficient polarisation transfer to spins at greater distance from protons (e.g. CF_2) is enabled.
- The mobile (amorphous) region is emphasised by a dipolar dephasing experiment (in essence a delayed acquisition after cross polarisation in the absence of ^{1}H decoupling with a moderately long contact time, cf. 2.) when the magnetisation of the crystalline region rapidly decays (cf. 3.).

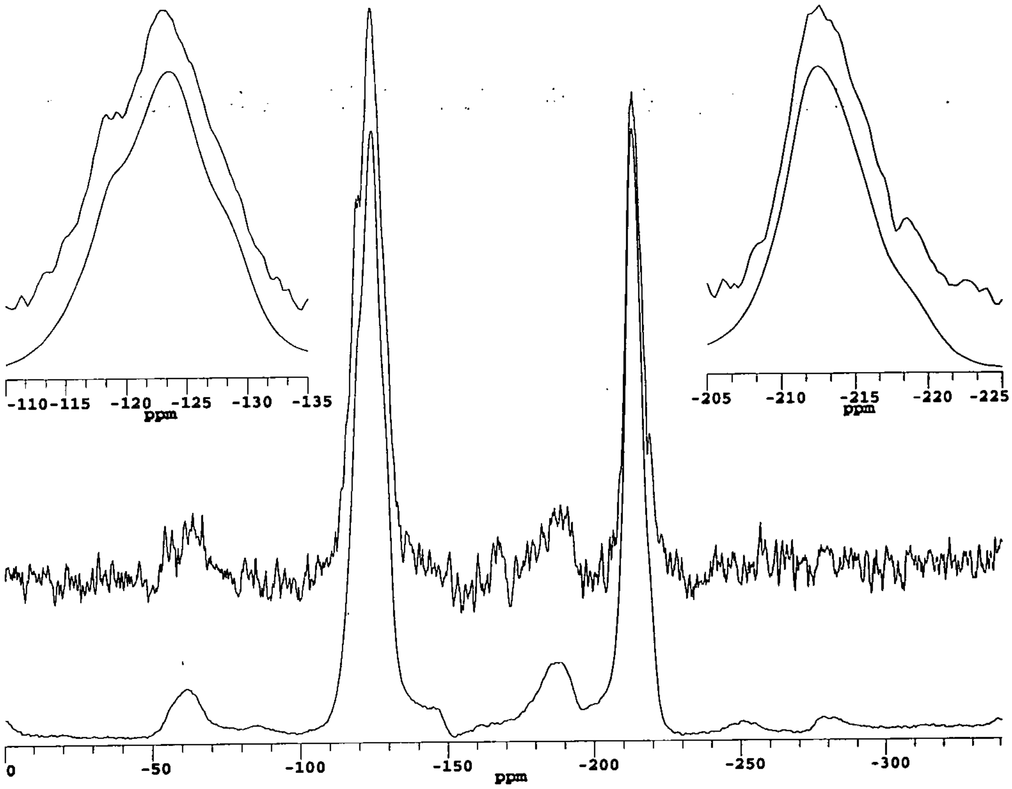

Figure 2.10: $T_{1\rho}^{H}$-filter prior to CPMAS experiment of PTrFE, MAS at 12 kHz,^{1}H-decoupled, top: spin lock of 20 ms, bottom: no spin lock for comparison, contact time $t_c = 0.2$ ms. The two spectra are normalised to the same height for the tallest peak

These experiments, with ^{19}F detection, have been applied to PTrFE with only limited effect. Figure 2.10 shows the effect of a $T_{1\rho}$-filter at ambient temperature. The top spectrum shows more pronounced peaks at -117 ppm, -207 ppm, and -222 ppm, whose intensity is increased compared to the main centre-peaks (at -124 ppm and -213 ppm).

The results of a different experiment which should reveal signals of mobile regions are shown in Figure 2.11. Especially in comparison with the $T_{1\rho}$-filter experiment, which favours crystalline domains as opposed to amorphous domains in the dipolar dephasing experiment, no real influence of selection can be detected.

2.2.2 Comparison with Results at Elevated Temperatures

It has been shown by Monti et al.[HM97] that the selection of crystalline and amorphous regions in PVDF ceases to work when the sample is cooled below the glass transition temperature $T_G(\text{PVDF}) = -35$ °C. As described in 2.2.1, all experiments

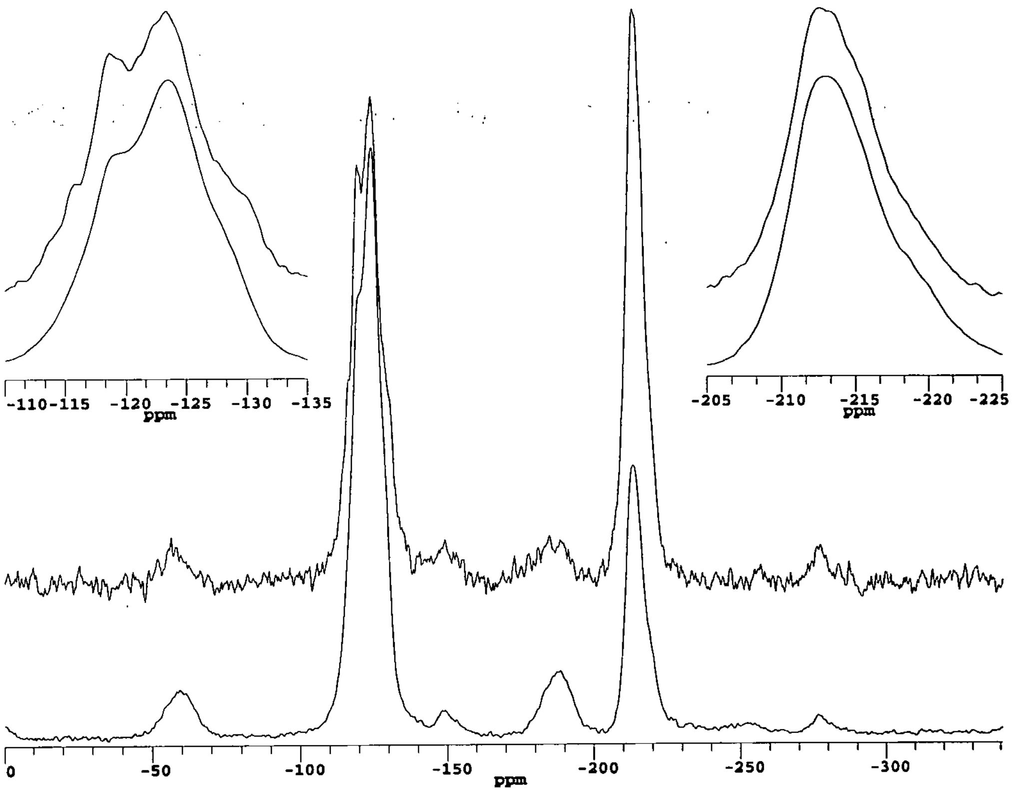

Figure 2.11: Dipolar dephasing experiments of PTrFE, MAS at 12 kHz, ^{1}H-decoupled, contact time $t_c = 0.5$ ms, top: dipolar dephasing for 500 μs, bottom: no dephasing for comparison. The two spectra are normalised to the same height for the tallest peak

for suppressing signals from certain domains rely on different mobilities. Below the glass transition temperature these mobilities are similar in crystalline and amorphous phase whereas above T_G they differ by an order of magnitude, at least for PVDF.

Experiments have therefore been attempted at elevated temperatures in order to induce motion in the amorphous (mobile) region. Different glass transition temperatures have been reported for PTrFE. Gaur[GW83] et al. state a glass transition at 31 °C for PTrFE. They also found the glass transition for PVDF to be -61 °C. However, other workers[Nal91] quote a glass transition of T_G(PVDF)=-40 °C. The discrepancy could be explained by the fact that glass transitions measured by different methods differ in their value. The given glass transition temperature *relevant for NMR experiments* must therefore be considered to lie in the range of $T_G(\text{PTrFE}) = 30\ldots50$ °C.

Figure 2.12 shows the effect of a $T_{1\rho}$-filter at 100 °C, which must be well above the glass transition. The corresponding dipolar dephasing experiment at 100 °C

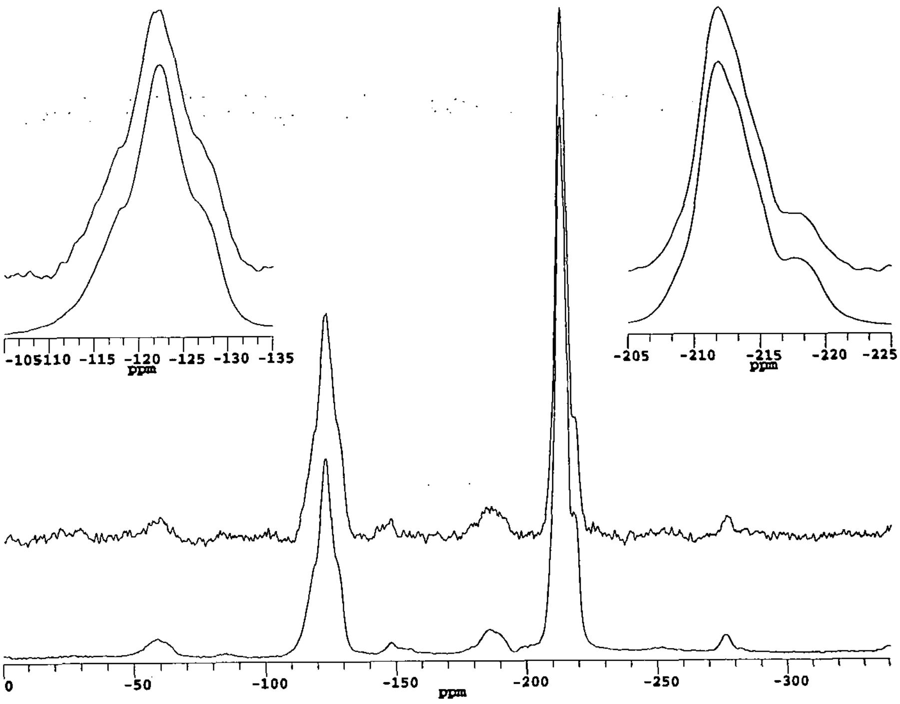

Figure 2.12: $T_{1\rho}^{H}$-filter prior to CPMAS experiment of PTrFE at T=100 °C, MAS at 12 kHz,^{1}H-decoupled, top: spin lock of 20 ms, bottom: no spin lock for comparison, contact time t_c = 0.2 ms. The two spectra are normalised to the same height for the tallest peak

is displayed in Figure 2.13. Different parameters (longer $T_{1\rho}$-spin-locks etc.) have been tried with the same result. Both experiments indicate that no selection has taken place. It could be argued that the spectrum with a longer dephasing time in Figure 2.13 shows a more pronounced shoulder at the CF_2 resonance which has been assigned to head-to-head imperfections. These are expected to be found in the amorphous region and should therefore show up more clearly. Considering the spectra observed on PVDF with similar experiments, it has to be said that clear selection did not take place by either $T_{1\rho}$-filter or dipolar dephasing experiment.

The comparison between single-pulse and the CP spectra (see Figure 2.15) exhibit a sudden change upon heating to higher temperatures. Linewidths are naturally smaller. Note that peaks for the CF_2-resonance arise at -117, -122, and -127 ppm and for the CFH-resonance at -211 and -218 ppm. Insofar chemical shifts are concerned no difference to ambient-temperature spectra can be noted. The considerable difference between CP and single-pulse spectra is readily explained by the reduced CP efficiency of the CF_2-group at higher temperature: Fluorines in the CF_2-group are allowed to move relatively to the proton. On the other hand we find, neglecting

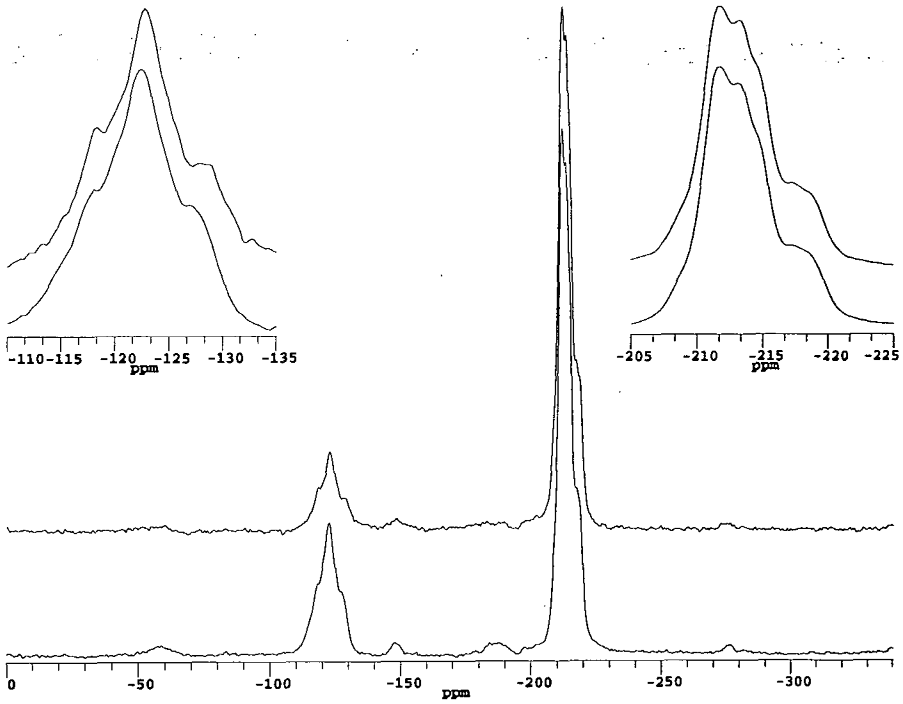

Figure 2.13: Dipolar dephasing experiments of PTrFE at T=100 °C, MAS at 12 kHz, ^{1}H-decoupled, contact time $t_c = 0.5$ ms, top: dipolar dephasing for 500 μs, bottom: no dephasing for comparison. The two spectra are normalised to the same height for the tallest peak

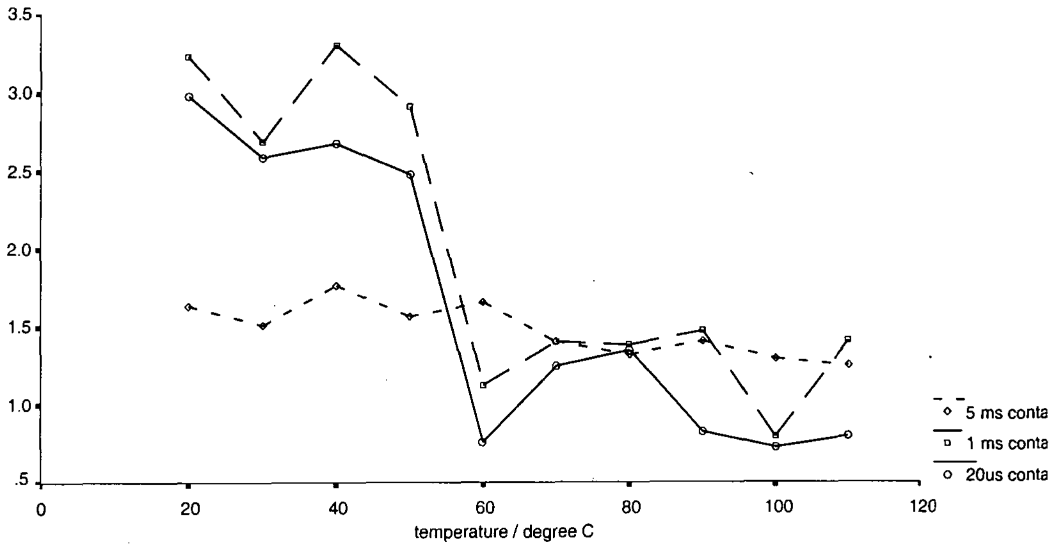

Figure 2.14: Ratio, r, of integrals over peaks for CFH and CF_2 resonance in a CP experiment vs. temperature: $r = \frac{I_{CF_2}}{I_{CFH}}$. The three different curves represent ratios of intensities at different contact times.

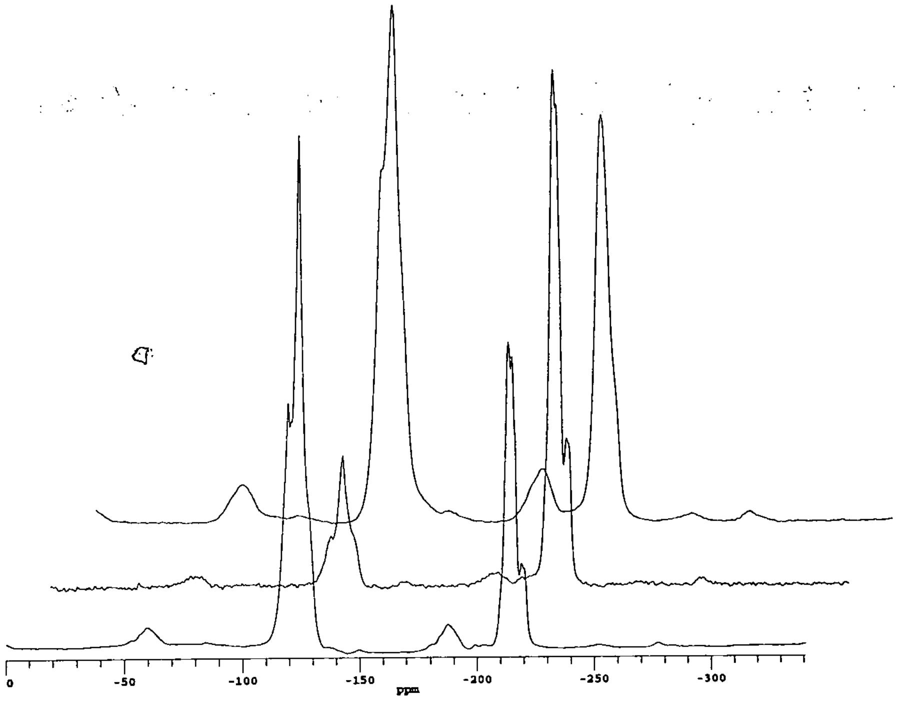

Figure 2.15: ^{19}F single-pulse(bottom) and $^{1}H \rightarrow {}^{19}F$ CP-spectrum(middle) (contact time $t_c = 0.5$ ms) of PTrFE at T=130 °C, MAS at 12 kHz. The ^{19}F single-pulse spectrum at ambient temperature is displayed for comparison(top). All spectra are ^{1}H-decoupled.

vibrational motion, that the triangular CFH-group is rigid and retains its capability to cross polarise, provided the whole group does not undergo liquid-like rapid motion and thus average heteronuclear coupling completely. The onset of motion is monitored by the dependence of the ratio of peaks upon temperature (see Figure 2.14. For short contact times a steep decrease in the intensity of the CF_2 resonance for temperatures higher than 55 °C can be noted. This temperature threshold coincides with the expected glass transition.

2.3 X-ray Diffraction

As mentioned earlier in this chapter, X-ray investigations have been performed in order to determine the crystalline structure of PTrFE [OK83]. This has been done in an attempt to understand the ferroelectric order of this compound.

In the present case the interest in X-ray data has been of a different nature. As will be discussed in the following chapter, it is desirable to have a rather homogeneous polymer to study cross-polarisation dynamics without the added intricacies of different phases. That is why it has been attempted to apply different treatments to the sample as purchased from Elf Atochem. It has been tried to precipitate PTrFE from a solution by water.[1] Experimental details are described in section 1.2.

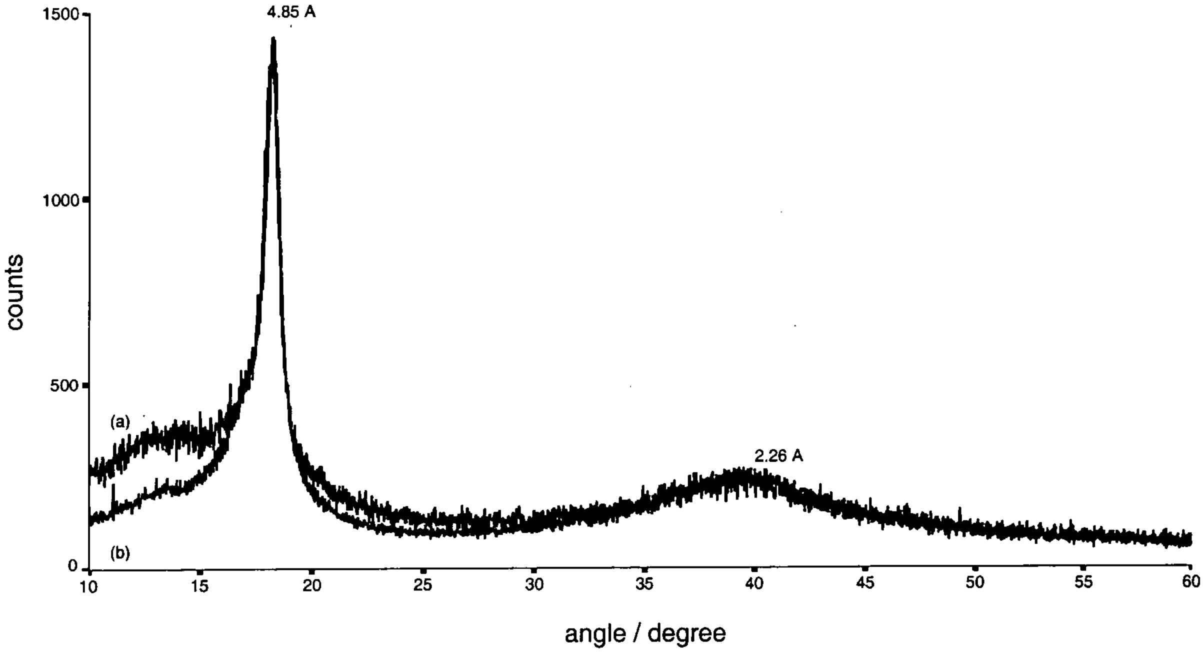

Figure 2.16: X-ray spectrum of (a) untreated, and (b) precipitated PTrFE. Numbers give d-spacing in Å.

Figure 2.16 shows the powder X-ray pattern of PTrFE as a plot of intensity versus angle. Both spectra are essentially the same - the treatment had no influence on the degree of crystallinity. Two peaks can be found with values for the d-spacing of 4.85 Å and 2.26 Å. Lovinger and Cais[LC84] discuss structure and morphology of PTrFE. According to their X-ray results of various uniaxially stretched PTrFE samples the 4.85 Å-peak is a strong equatorial reflection, which has been indexed

---

[1] This work has kindly been done by Dr.Shinji Ando.

as 100 of a hexagonally based lattice. They report two more equatorial peaks (at 2.81 Åand 2.43 Å), which are not observable in Figure 2.16. The other 2.26 Å-peak is found to be a meridional peak which is attributed to a 3/1-helical conformation. As can be seen this peak is extremely broad and diffuse. This is explained by small crystallites and the high level of atacticity in the molecules.

From the broad and diffuse appearance of the meridional peak and the lack of peaks expected for a *all-trans* conformation Lovinger and Cais[LC84] conclude that PTrFE does not crystallise in one of the regular conformation (*all-trans* or 3/1 helical). Instead it is inferred that PTrFE consists of an irregular succession of TG, $T\overline{G}$ and TT sequences. Owing to this disordered conformation, PTrFE chains will pack like cylinders in a hexagonal lattice. The relatively sharp peak of the equatorial peak supports this conclusion.

2.4 Summary

Prior to solid-state spectroscopy on PTrFE, solution-state fluorine spectra have been interpreted, based on previous assignments of peaks[TSC82]. A defect level (percentage of monomer inversions) of 13.5% has been calculated. Peaks of the solid-state fluorine spectrum have been assigned with respect to the chemical structure of PTrFE.

It has been shown that conventional selection by means of a $T_{1\rho}$-filter and dipolar dephasing fails to select regions of different mobilities in PTrFE even at temperatures higher than the given glass transition stated in the literature. Selection is aggravated by the fact that the fluorine spectrum does not show resolved features of crystalline and amorphous peaks. It could be shown that an onset of motion occurs around 55 °C, which is ascribed to the glass transition. Via ab initio calculation an asymmetric shielding anisotropy tensor for fluorine has been calculated. However, an axially symmetric tensor is observed. This observation and the low efficiency of proton decoupling indicate that considerable motion occurs already at ambient temperature. Thus, PTrFE undergoes a gradual change over a range of temperatures around the glass transition stated above.

The X-ray results of section 2.3 agree with the findings of Lovinger[LC84]. His interpretation and ab initio calculation of the geometrical structure suggest a conformation of TG, $T\overline{G}$, and TT groups. Whether this leads to a polar structure as proposed by Oka et al.[OK83, OK84, OK85] can not be decided on the basis of the present data. However, the high degree of stereo-irregularity and atacticity raises some doubt about a regular arrangement of TG, $T\overline{G}$, and TT groups. It seems more likely that a disordered succession of conformational groups is present, leading to PTrFE chains in the shape of cylinders, which are packed hexagonally[LC84].

Chapter 3

CP - Dynamics of Fluorinated Compounds

At the centre of the present work stands the investigation of cross-polarisation(CP) dynamics in fluorinated compounds. Section 3.1 will clarify the theoretical background of this problem. Section 3.2 will try to support models proposed and outline the discrepancies encountered.

3.1 Theory

3.1.1 Phenomenological Spin-Temperature Approach

Let us begin with a phenomenological spin temperature approach. Although there are a number of objections (see section 3.1.2) to its applicability to an abundant

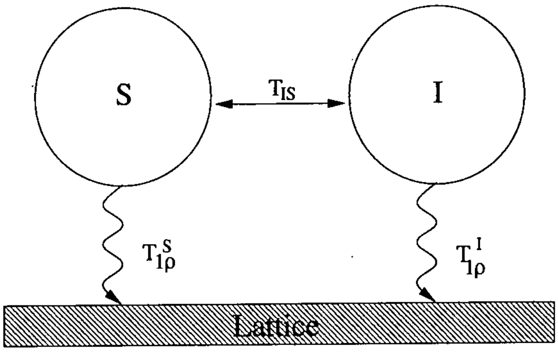

Figure 3.1: Schematic representation of two spin reservoirs $I(N_I, \gamma_I, \beta_I = \hbar/kT_I)$ and S $(N_S, \gamma_S, \beta_S = \hbar/kT_S)$ coupled to each other (expressed via T_{IS}) and to the lattice $(T_{1\rho}^{I}, T_{1\rho}^{S})$

spin system, it may still prove useful to get a feel for the complex behaviour of spin systems of this kind.

Figure 3.1 depicts schematically how the two spin baths interact. The concept of spin temperature has been frequently used by many authors to describe NMR experiments[Meh83, Abr61]. Therefore a brief introduction to this idea should suffice. The high temperature approximation for the density matrix, ρ, is given by

$$\rho = Z^{-1}(1 - \beta\mathcal{H})$$

where $\mathcal{H}$ denotes the Hamiltonian and

$$Z = \mathrm{Tr}\{\mathbf{1}\} = (2I+1)^{N_I}(2S+1)^{N_S}$$

and

$$\beta = \hbar/kT.$$

We can define the magnetisation M based on the density matrix ρ:

$$M_i = \hbar\gamma\mathrm{Tr}\{\rho I_i\} \qquad i = x, y, z$$

Assuming just a Zeeman interaction $\mathcal{H} = -\gamma B \cdot I_i$ we find

$$M_i = \beta C \cdot B, \qquad \text{where} \qquad C = \frac{1}{3}N \cdot I(I+1)\gamma^2\hbar. \tag{3.1}$$

The inverse lattice temperature $\beta_L = \frac{\hbar}{kT_L}$ is related to the initial magnetisation of the S and I nuclei $M_{0I} = \beta_L C_I B_0$ and $M_{0S} = \beta_L C_S B_0$. In the CP experiment, the magnetisation M_{0I} is flipped into the xy-plane by a $\frac{\pi}{2}$-pulse and can then be spin-locked with a field $B_I \ll B_0$. Thus, the new inverse spin temperature β_{I0} is given by

$$M_{0I} = \beta_L C_I B_0 = \beta_{I0} C_I B_I$$

where we find $\beta_{I0}/\beta_L = B_0/B_I \gg 1$. We have now arrived at the starting point of cross polarisation. The I spins are cooled to a low temperature (big values of β) in th rotating frame by the initial pulse on the I channel. The S spins have an initial inverse spin temperature of zero (no polarisation in the xy-plane, $M_{x,y}$=0). The two spin baths are brought into contact via the Hartmann-Hahn match. Equation 3.1 reminds us that magnetisation and inverse spin temperature are synonymous in the sense that they are proportional. It is now that the thermodynamic argument for

CP dynamics comes in to play. Ignoring relaxation at the first stage we can invoke energy (magnetisation) conservation in the rotating frame:

$$\frac{d}{dt}\beta_I + \epsilon\frac{d}{dt}\beta_S = 0$$

In other words magnetisation is exchanged only between the two baths. At this point it seems sensible to assume rate equations for this exchange, i.e. magnetisation exchange is proportional to population differences. This leads us to a system of differential equations of the following form

$$\frac{d}{dt}\beta_S = -\frac{1}{T_{IS}}(\beta_S - \beta_I) - \frac{1}{T_{1\rho}^S}\beta_S \tag{3.2}$$

$$\frac{d}{dt}\beta_I = -\frac{\epsilon}{T_{IS}}(\beta_I - \beta_S) - \frac{1}{T_{1\rho}^I}\beta_I \tag{3.3}$$

where the two last terms are appended in order to take account of spin-lattice relaxation in the rotating frame. The boundary conditions are, as described in the text above:

$$\beta_S(0) = 0 \qquad \text{and} \qquad \beta_I(0) = \beta_{I0}$$

This system of coupled differential equations is solved in appendix A. We simply quote the solution here:

$$\beta_S(t) = \beta_{I0}\frac{1}{a_+ - a_-}(\exp(-\frac{a_-t}{T_{IS}}) - \exp(-\frac{a_+t}{T_{IS}})) \tag{3.4}$$

$$\begin{aligned}\beta_I(t) = \beta_{I0}\frac{1}{a_+ - a_-}\Big((1 + \frac{T_{IS}}{T_{1\rho}^S} - a_-)\exp(-\frac{a_-t}{T_{IS}}) \\ -(1 + \frac{T_{IS}}{T_{1\rho}^S} - a_+)\exp(-\frac{a_+t}{T_{IS}})\Big)\end{aligned} \tag{3.5}$$

where $a_\pm$ are functions of T_{IS}, $T_{1\rho}^S$, $T_{1\rho}^I$ and $\epsilon = \frac{N_S}{N_I}$ for exact match. Now the limiting cases of these solutions can be investigated, as has been thoroughly done by Mehring[Meh83]. Therefore, the present discussion is restricted only to the most common form of the above equations. This is the case for most ^{1}H→ ^{13}C CP experiments, where dilute and negligibly relaxing S spins can be found ($\epsilon \to 0; T_{1\rho}^S \gg T_{1\rho}^I$):

$$\beta_S(t) = \beta_{I0}\frac{T_{1\rho}^I}{T_{1\rho}^I - T_{IS}}(\exp(-\frac{t}{T_{1\rho}^I}) - \exp(-\frac{t}{T_{IS}}))$$

3.1.2 Analysis of Underlying Assumptions

In the following section we will not try to repeat the derivation of cross-relaxation dynamics, which has been extensively dealt with in the literature[DTW75, Meh83]. Instead, let us consider in greater depth the assumptions which lead to the thermodynamic approach, concentrating on the crucial steps of the derivation of Demco et al. Thus we will discuss some of the derivations of Demco and co-workers in a more qualitative light.

The high-field double-resonance Hamiltonian in the laboratory frame of reference is given by[1]

$$\mathcal{H} = \mathcal{H}_I + \mathcal{H}_S + \mathcal{H}_{IS} + \mathcal{H}_{rf}(t)$$

where the first two terms include the Zeeman interaction, the chemical shift interaction and magnetic interaction between like spins:

$$\mathcal{H}_I = \mathcal{H}_{ZI} + \mathcal{H}_{CI} + \mathcal{H}_{II} \quad \text{and} \quad \mathcal{H}_S = \mathcal{H}_{ZS} + \mathcal{H}_{CS} + \mathcal{H}_{SS}$$

The term $\mathcal{H}_{IS}$ describes heteronuclear interaction between spins I and S. And the interaction with the external rf field is included with

$$\mathcal{H}_{rf}(t) = -2\omega_{1I} I_x \cos\omega_I t - 2\omega_{1S} S_x \cos\omega_S t.$$

Before the Hamiltonian is transformed into a more convenient frame of reference we shall rid ourselves of terms which can be neglected. The homonuclear interaction between S spins, $\mathcal{H}_{SS}$, is negligible, presuming that the effective field applied to the S spins is much greater than the local field produced by other S spins. It should be borne in mind that this might not always be justified in the case of ^{1}H→ ^{19}F CP. If we consider single S spins we can include the chemical shift term $\mathcal{H}_{CS}$ into the Zeeman interaction term $\mathcal{H}_{ZS}$. The irradiation described by $\mathcal{H}_{rf}(t)$ can be rewritten as superposition of two counter-rotating rf fields:

$$2\cos\omega t = e^{i\omega t} + e^{-i\omega t}$$

We can neglect one of these counter-rotating rf fields, assuming that it is off-resonance by $\approx 2\omega$.

---

[1] For convenience Hamiltonians are given in angular frequency units. In accordance with the *Système Internationale d'Unités* (SI) $\hbar$ is *not* set equal to 1.

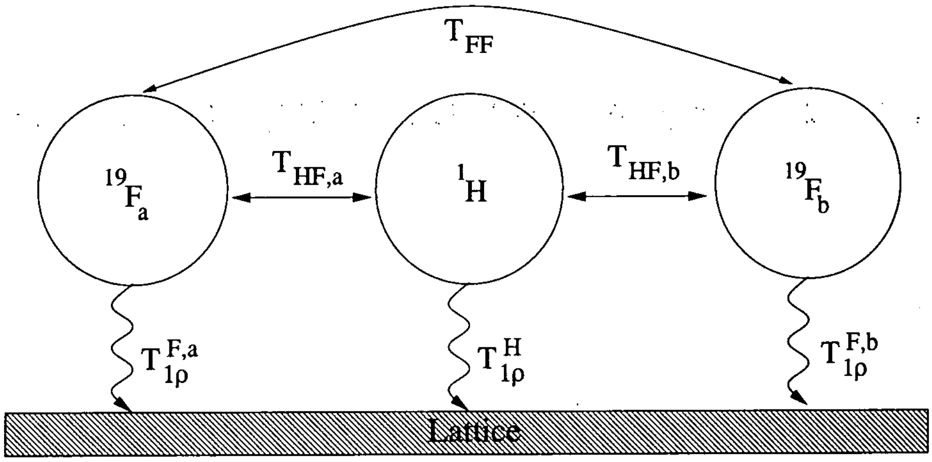

Figure 3.2: Schematic representation of three spin reservoirs exemplified by one proton and two fluorine spin baths: $^1H(N_H, \gamma_H)$, ^{19}F $(N_{F_{19},a}, \gamma_F)$ and ^{19}F $(N_{F_{19},b}, \gamma_F)$ coupled to each other (expressed via T_{FF}, $T_{HF,a}$, and $T_{HF,b}$) and to the lattice ($T_{1\rho}^H$, $T_{1\rho}^{F,a}$, and $T_{1\rho}^{F,b}$)

3.1.3 Thermodynamic Approach for Three Spin Baths

Now that we have seen in the preceding section under what circumstances the thermodynamic approach is valid, we are setting out to extend the phenomenological model for a two-spin-bath situation. Our motivation is that we find in PTrFE a situation with two distinct fluorine types. The two sites show different spin-lattice relaxation behaviour in the rotating frame. The cross-relaxation times are distinctly different because the proton-fluorine distance is much shorter for the CFH group compared to the CF_2 group.

By analogy to the schematic representation of two spin baths depicted in Figure 3.1 we can extend the model as depicted in Figure 3.2. Although it is shown for the special case of ^{1}H→ ^{19}F CP, this three-spin-bath model is, of course, not restricted to these nuclei.

If we want to develop the phenomenological transport equations we need to ensure two principles: Firstly, in the limit of an infinite cross-relaxation time for one bath we should obtain the already known set of equations 3.2 and 3.3. Secondly, for infinite spin-lattice relaxation, the energy conservation law must be obeyed. The following system fulfills these requirements:

$$\frac{d}{dt}\beta_H = -\frac{\epsilon_{HF,a}}{T_{HF,a}}(\beta_H - \beta_{F,a}) - \frac{\epsilon_{HF,b}}{T_{HF,b}}(\beta_H - \beta_{F,b}) - \frac{1}{T_{1\rho}^H}\beta_H \tag{3.8}$$

$$\frac{d}{dt}\beta_{F,a} = -\frac{1}{T_{HF,a}}(\beta_{F,a} - \beta_H) - \frac{\epsilon_{FF}}{T_{FF}}(\beta_{F,a} - \beta_{F,b}) - \frac{1}{T_{1\rho}^{F,a}}\beta_{F,a} \tag{3.9}$$

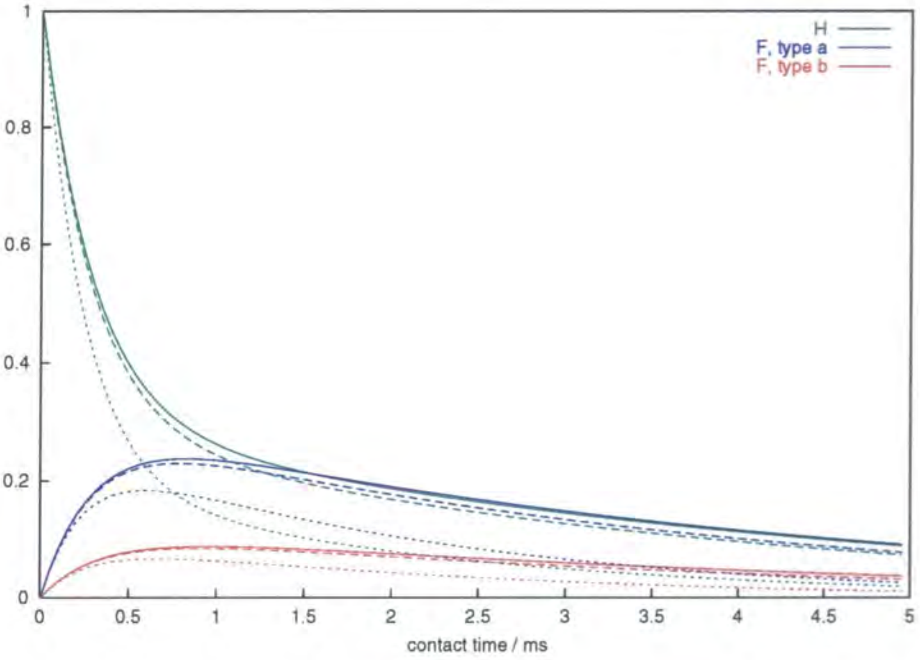

Figure 3.3: Simulation of a system of three spin baths. Parameters are $T_{1\rho}^{F,a} = 5$ ms, $T_{1\rho}^{F,b} = 5$ ms, $T_{HF,a} = 1$ ms, $T_{HF,b} = 3$ ms, $T_{FF} = 10$ ms, $\epsilon_{HF,a} = 2$ and $\epsilon_{HF,b} = 1$. $T_{1\rho}^{H}$ was varied: 10 ms (solid), 5 ms (dashed) and 1 ms (dotted)

$$\frac{d}{dt}\beta_{F,b} \;=\; -\frac{1}{T_{HF,b}}(\beta_{F,b} - \beta_H) - \frac{1}{T_{FF}}(\beta_{F,b} - \beta_{F,a}) - \frac{1}{T_{1\rho}^{F,b}}\beta_{F,b} \qquad (3.10)$$

Spin temperatures β_H, $\beta_{F,a}$ and $\beta_{F,b}$ are defined as in section 3.1.1. Relative heat capacities ϵ are given by the following set of equations, if we assume an on-resonance Hartmann-Hahn condition:

$$\epsilon_{HF,a} = \frac{N_{F,a}}{N_H}, \quad \epsilon_{HF,b} = \frac{N_{F,b}}{N_H} \quad \text{and} \quad \epsilon_{FF} = \frac{N_{F,b}}{N_{F,a}} = \frac{\epsilon_{HF,b}}{\epsilon_{HF,a}}$$

Now, if $T_{1\rho}^{H}, T_{1\rho}^{F,a}, T_{1\rho}^{F,a} \to \infty$ then energy conservation can be invoked

$$\frac{d}{dt}(\beta_H + \epsilon_{HF,a}\beta_{F,a} + \epsilon_{HF,b}\beta_{F,b}) = 0$$

And if we let the cross-relaxation times $T_{HF,a}, T_{HF,b}$ and T_{FF} separately tend to infinity, we arrive at the two-spin-bath model described in section 3.1.1.

Appendix A.2 shows how the above system can be solved in general. In the following the behaviour of this system shall be demonstrated. To study the influence of some of the system parameters, a simulation was done with the values stated. The experiments will be discussed in terms of protons and fluorines, although no reason other than convenience leads to this choice.

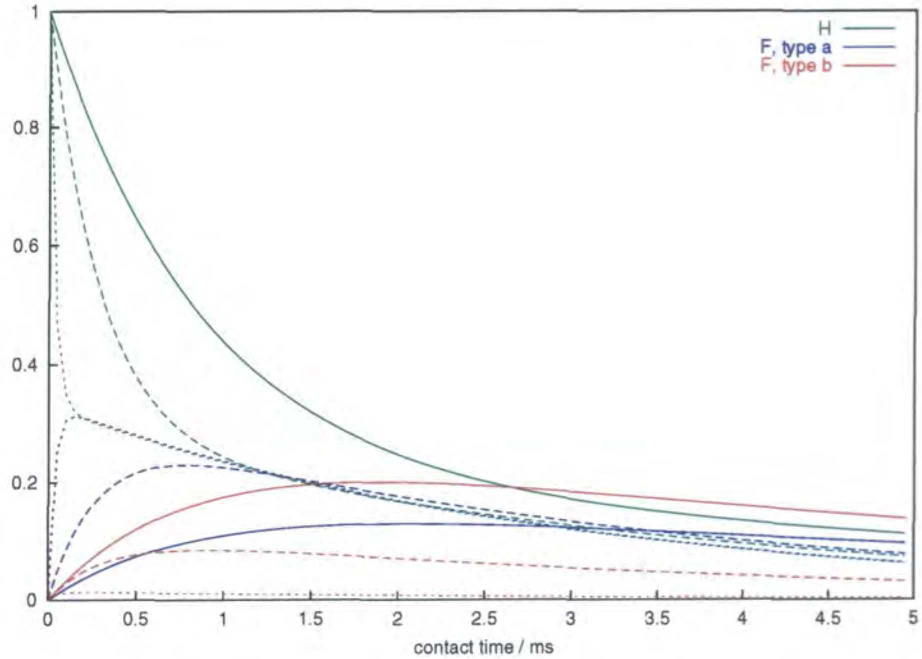

Figure 3.4: Simulation of a system of three spin baths. Parameters are $T_{1\rho}^{H} = 5$ ms, $T_{1\rho}^{F,a} = 5$ ms, $T_{1\rho}^{F,b} = 5$ ms, $T_{HF,b} = 3$ ms, $T_{FF} = 10$ ms, $\epsilon_{HF,a} = 2$ and $\epsilon_{HF,b} = 1$. $T_{HF,a}$ was varied: 5 ms (solid), 1 ms (dashed) and 0.1 ms (dotted)

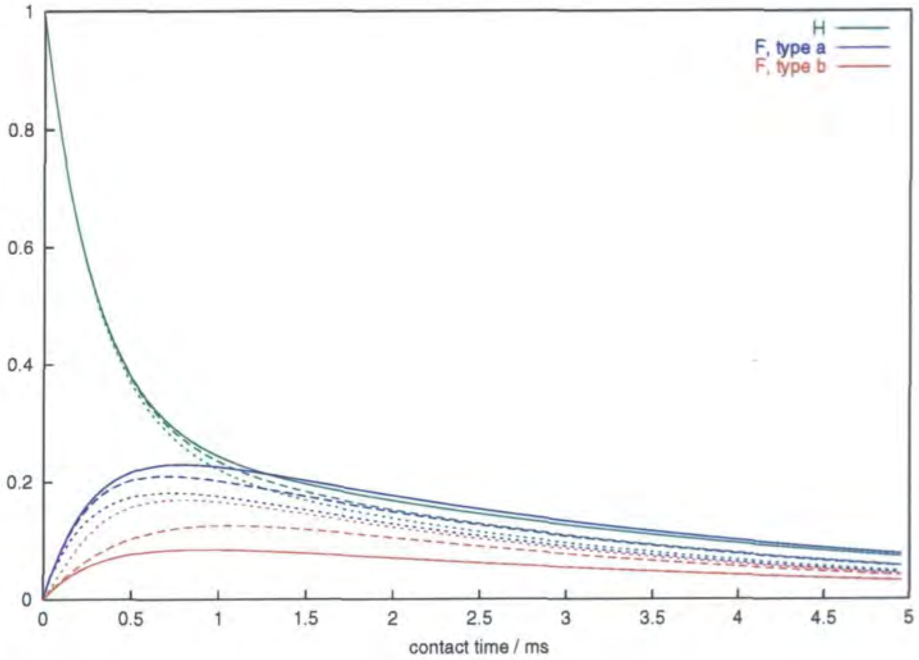

Figure 3.5: Simulation of a system of three spin baths. Parameters are $T_{1\rho}^{H} = 5$ ms, $T_{1\rho}^{F,a} = 5$ ms, $T_{1\rho}^{F,b} = 5$ ms, $T_{HF,a} = 1$ ms, $T_{HF,b} = 3$ ms, $\epsilon_{HF,a} = 2$ and $\epsilon_{HF,b} = 1$. T_{FF} was varied: 10 ms (solid), 1 ms (dashed) and 0.1 ms (dotted)

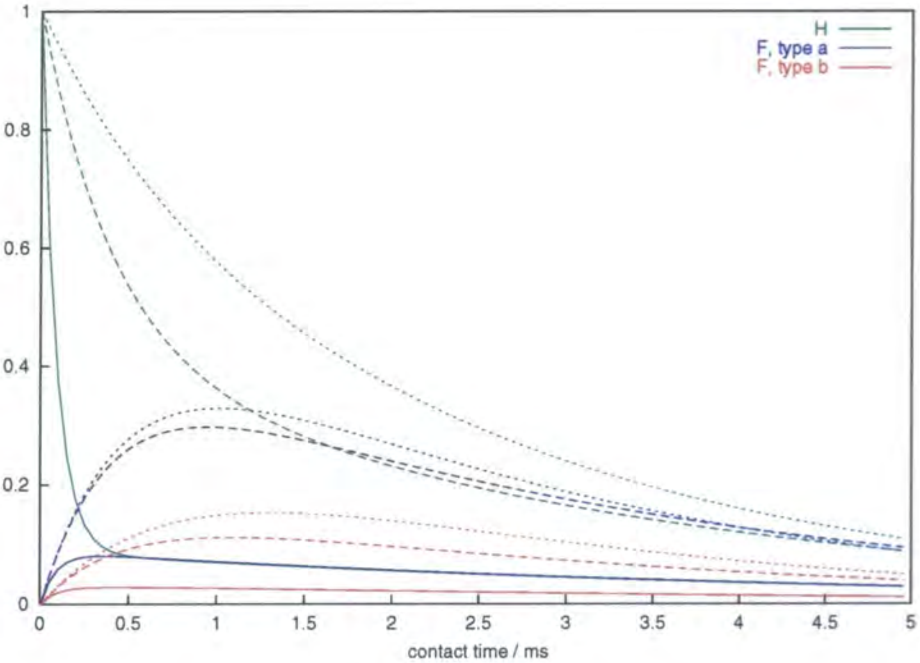

Figure 3.6: Simulation of a system of three spin baths. Parameters are $T_{1\rho}^{H} = 5$ ms, $T_{1\rho}^{F,a} = 5$ ms, $T_{1\rho}^{F,b} = 5$ ms, $T_{HF,a} = 1$ ms, $T_{HF,b} = 3$ ms, $T_{FF} = 10$ ms and $\epsilon_{HF,b} = 1$. $\epsilon_{HF,a}$ was varied: 10 (solid), 1 (dashed) and 0.1 (dotted)

Figure 3.3 demonstrates the influence of $T_{1\rho}$ for the protons, the source of magnetisation in the standard CP experiment. As can be seen, the shorter the value of $T_{1\rho}^{H}$, the faster the magnetisation of protons dies away, as expected. Correspondingly, the fluorine magnetisation of the two fluorine baths reaches its maximum earlier and at a lower level. The ratio of the magnetisations of the two fluorines is only marginally influenced.

Figure 3.4 shows the influence of a particular cross-relaxation parameter. Obviously, shorter $T_{HF,a}$ lead to a faster decrease of the proton magnetisation and a more rapid increase in the magnetisation of the fluorine of type *a*. Hand in hand with the faster drainage of proton magnetisation goes a slower increase in the magnetisation of fluorines of type *b*. However, if a very short cross-relaxation time between the two kinds of fluorines would have been chosen, magnetisation of the two types of fluorines would increase. Fluorines *b* would get their magnetisation through fluorines *a* and also increase more rapidly with decreasing $T_{HF,a}$.

The effect of shorter cross-relaxation times between the two fluorines is sketched in Figure 3.5. The faster this process of cross relaxation is possible, i.e. the shorter T_{FF} is, the closer the curves for the two fluorines get. In the limit of $T_{FF} = 0$ this would lead to the two-spin-bath case.

The relative heat capacity ϵ has already been introduced in the two-spin case. If we had different types of protons, for instance one type closely bound and the other at a distance, it would be necessary to introduce an 'effective' ϵ. This should not be necessary if the system under observation is fully described by the three-spin model. The ratio of fluorines per proton should truly reflect these ϵ. The influence of different values for the relative heat capacity are depicted in Figure 3.6. The bigger the relative heat capacity of fluorines of the type a, $\epsilon_{HF,a}$, the more difficult it gets to cool this bath, i.e. to increase $\beta_{F,a}$. Thus, the proton magnetisation is heated much faster, i.e. β_H decreases more rapidly. Surprisingly, the ratio of intensities between the two fluorine baths does not change very much if the heat capacity is changed.

Of course, it is not feasible to determine seven parameters (three spin-lattice relaxation times in the rotating frame, three cross-relaxation times and two arbitrary intensities, which are determined by receiver amplifiers etc.) from one fit to a CP curve. That is why measuring these parameters independently from each other has to be tried.

A parameter which can be measured separately is the spin-lattice relaxation time. This can be readily done for protons either directly or indirectly via CP with a constant contact time. But if one tries to measure $T_{1\rho}$ of fluorine, already three parameter come to play. The relaxation process is not only governed by two spin-lattice relaxation times, $T_{1\rho}^{F,a}$ and $T_{1\rho}^{F,b}$, but also by homonuclear cross polarisation expressed by the cross-relaxation time T_{FF}. In essence, this is a case of cross polarisation with initial conditions different from the standard CP experiment. The two initial magnetisations are at maximum rather than one at maximum and one zero.

This would lead to a double-exponential decay instead of a single-exponential, with decay rates depending on all three relaxation times. However, cross relaxation has only a subtle influence, because the two magnetisations start at maximum. In order to measure T_{FF} it is much more sensible to work with a different scheme. If the two magnetisations have opposite signs in the beginning of the experiment, cross relaxation would play a much greater role, thus being at our disposal for scrutiny.

An experiment of that kind is a derivative of the selective polarisation experiment (SPI). To get comparable conditions the magnetisation exchange has to be performed

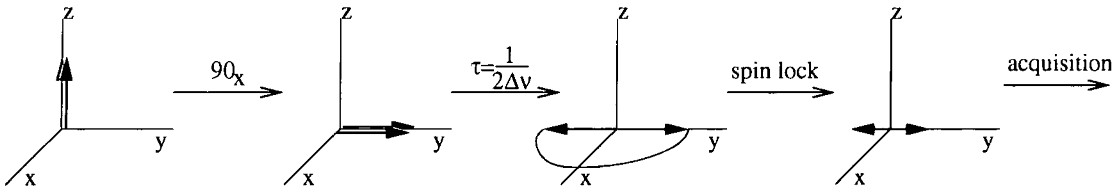

Figure 3.7: Vector representation of magnetisation vectors in a selective polarisation inversion in the rotating frame. Irradiation is performed on resonance for the vector of magnetisation which is marked red.

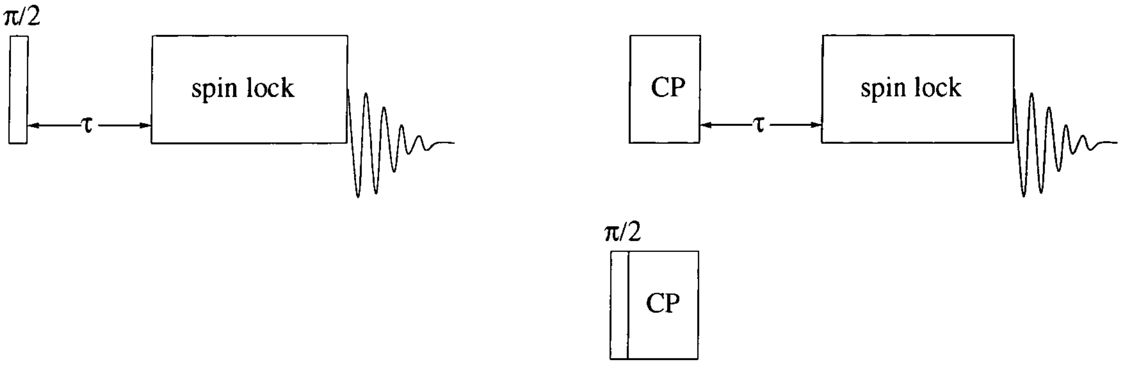

(a) (b)

Figure 3.8: Pulse sequence for selective polarisation inversion in the rotating frame. (a) creation of magnetisation directly with a single 90° pulse and (b) transfer of magnetisation from another set of nuclei for background suppression and in order to take advantage of shorter T_1's

in the rotating frame rather than aligning magnetisation vectors along the z-axis and letting them exchange in the laboratory frame. The selection of the nuclei is based on a difference in chemical shift.

Figure 3.7 depicts the manipulation of the vectors of magnetisation during the selective polarisation inversion in the rotating frame. The corresponding pulse sequence is depicted in Figure 3.8. Initially, both magnetisations are tipped into the xy-plane. Because they have different chemical shifts, they precess at different frequencies in the rotating frame. Presuming their chemical shift difference is $\Delta\nu$ and irradiation is on resonance for one of the two nuclei, the two vectors will be out of phase by 180° after a time $\tau = \frac{1}{2\Delta\nu}$. If spin locking starts at that point we have the desired situation, where the two magnetisations start with a maximal difference in magnetisation.

3.1.4 Theory of Transient Oscillations

Let us now turn our attention to the short-time behaviour of cross polarisation. Müller, Ernst and co-workers were the first to observe what they called transient oscillations in a CP experiment on a single crystal of ferrocene[MKBE74]. They assumed a model which essentially incorporates two proton spin reservoirs (I), one of which is in direct contact to the directly-bonded carbon (S) and exchanges magnetisation in a coherent fashion. The other (bigger) spin bath exchanges magnetisation via spin diffusion with the directly-bonded protons, which results in a damping of the dipolar oscillations mentioned above. We shall turn our attention to these oscillations without considering spin diffusion and $T_{1\rho}$-relaxation but extending the case to powders and MAS. We follow a theoretical description of Levitt et al.[LSE86]. We will limit our observations to the special case of a spin-pair ($k = 1$). However the following introducing definitions will cover the general case of k I spins interacting with one S spin.

We start from the Hamiltonian in the 'doubly rotating' interaction frame, as usual after the high-field truncation. This Hamiltonian has been dealt with in section 3.1.2. Note, however, that in equation 3.6 already two transformations to the lab-frame Hamiltonian have been applied. We will perform the 'tilting' transformation T here after some simplification of the Hamiltonian in the rotating frame.

$$\mathcal{H} = \mathcal{H}_I + \mathcal{H}_S + \mathcal{H}_{IS} + \mathcal{H}_{II} \tag{3.11}$$

where $\mathcal{H}_I = \sum_k \Omega_k I_{kz} + \omega_{1I} \sum_k I_{kx}$ and $\mathcal{H}_S = \Omega_S S_{kz} + \omega_{1S} D_x$ describe the spin reservoirs of I and S spins. Furthermore, the heteronuclear dipolar interaction is given by $\mathcal{H}_{IS} = \sum_k b_k 2 I_{kz} S_z$ where

$$b_k = -\frac{\mu_0 \gamma_I \gamma_S \hbar}{4\pi r_k^3} \frac{1}{2} (3\cos^2 \Theta_k - 1) \tag{3.12}$$

and the homonuclear interaction between I spins $\mathcal{H}_{II} = \sum_j \sum_k d_{jk} (2 I_{jz} I_{kz} - \frac{1}{2}(I_j^+ I_k^- + I_j^- I_k^+))$, with the dipolar coupling constant

$$d_{jk} = -\frac{\mu_0 \gamma_I^2 \hbar}{4\pi r_{jk}^3} \frac{1}{2} (3\cos^2 \Theta_{jk} - 1) \tag{3.13}$$

To simplify the calculations we will neglect resonance offsets: $\Omega_k = \Omega_S = 0$. For the time being we will also neglect homonuclear interactions: $d_{jk} = 0$.

It is convenient to write the Hamiltonian in a frame rotated about the y-axis defined by the following transformation

$$A \to A^T : A^T = \exp(i\frac{\pi}{2}(\sum_k I_{ky} + S_y)) A \exp(-i\frac{\pi}{2}(\sum_k I_{ky} + S_y))$$

which leads to the transformed Hamiltonian $\mathcal{H} = \mathcal{H}_I^T + \mathcal{H}_S^T + \mathcal{H}_{IS}^T$. With the above mentioned simplifications, the respective terms are:

$$\begin{aligned}
\mathcal{H}_I^T &= \sum_k \omega_{1I} I_{kz} \\
\mathcal{H}_S^T &= \omega_{1S} S_z \\
\mathcal{H}_{IS}^T &= \sum_k b_k 2 I_{kx} S_x
\end{aligned}$$

It is quite instructive to have a look at the special case with $k = 1$ and to write out these equations in matrix notation. If we take the Pauli spin matrices and denote the identity with $\mathbf{1}$.

$$l_x = \frac{1}{2}\begin{pmatrix} 0 & 1 \\ 1 & 0 \end{pmatrix}, \; l_y = \frac{1}{2}\begin{pmatrix} 0 & -i \\ i & 0 \end{pmatrix} \text{ and } l_z = \frac{1}{2}\begin{pmatrix} 1 & 0 \\ 0 & -1 \end{pmatrix}$$

we can write the spin matrices for two spin $\frac{1}{2}$ particles via the tensor product:

$$I_x = l_x \otimes \mathbf{1} = \frac{1}{2}\begin{pmatrix} 0 & 0 & 1 & 0 \\ 0 & 0 & 0 & 1 \\ 1 & 0 & 0 & 0 \\ 0 & 1 & 0 & 0 \end{pmatrix} \qquad S_x = \mathbf{1} \otimes l_x = \frac{1}{2}\begin{pmatrix} 0 & 1 & 0 & 0 \\ 1 & 0 & 0 & 0 \\ 0 & 0 & 0 & 1 \\ 0 & 0 & 1 & 0 \end{pmatrix}$$

$$I_y = l_y \otimes \mathbf{1} = \frac{1}{2}\begin{pmatrix} 0 & 0 & -i & 0 \\ 0 & 0 & 0 & -i \\ i & 0 & 0 & 0 \\ 0 & i & 0 & 0 \end{pmatrix} \qquad S_y = \mathbf{1} \otimes l_y = \frac{1}{2}\begin{pmatrix} 0 & -i & 0 & 0 \\ i & 0 & 0 & 0 \\ 0 & 0 & 0 & -i \\ 0 & 0 & i & 0 \end{pmatrix}$$

$$I_z = l_z \otimes \mathbf{1} = \frac{1}{2}\begin{pmatrix} 1 & 0 & 0 & 0 \\ 0 & 1 & 0 & 0 \\ 0 & 0 & -1 & 0 \\ 0 & 0 & 0 & -1 \end{pmatrix} \qquad S_z = \mathbf{1} \otimes l_z = \frac{1}{2}\begin{pmatrix} 1 & 0 & 0 & 0 \\ 0 & -1 & 0 & 0 \\ 0 & 0 & 1 & 0 \\ 0 & 0 & 0 & -1 \end{pmatrix}$$

With these definitions we get a Hamiltonian of the shape

$$\mathcal{H}^T = \frac{1}{2}\begin{pmatrix} \omega_{1I} + \omega_{1S} & 0 & 0 & b \\ 0 & \omega_{1I} - \omega_{1S} & b & 0 \\ 0 & b & -\omega_{1I} + \omega_{1S} & 0 \\ b & 0 & 0 & -\omega_{1I} - \omega_{1S} \end{pmatrix}.$$

If we write, for reasons of brevity, $\Omega = \omega_{1I}+\omega_{1S}$ and $\Delta = \omega_{1I}-\omega_{1S}$ we can decompose the Hamiltonian into two parts $\mathcal{H}^T_\Omega = \begin{pmatrix} \Omega & b \\ b & -\Omega \end{pmatrix}$ and $\mathcal{H}^T_\Delta = \begin{pmatrix} \Delta & b \\ b & -\Delta \end{pmatrix}$, or in general in terms of spin $\frac{1}{2}$ operators for the respective subspace[3]:

$$\mathcal{H}^T_\chi = \chi I^\chi_z + b I^\chi_x \text{ where } \chi = \Omega, \Delta \tag{3.14}$$

Actually, these matrices are still of order 4×4, with zeroes at the appropriate positions. The aim now is to diagonalise $\mathcal{H}^T$ or, separately, $\mathcal{H}^T_\Omega$ and $\mathcal{H}^T_\Delta$. This can be done by rotation about the y-axis by a certain angle Θ^χ:

$$(\mathcal{H}^T_\chi)_D = e^{i\Theta^\chi I^\chi_y} \mathcal{H}^T_\chi e^{-i\Theta^\chi I^\chi_y}$$

With the form of the Hamiltonian given in equation 3.14 we can explicitly write for the transformed Hamiltonians:

$$(\mathcal{H}^T_\chi)_D = (\chi \cos\Theta^\chi + b \sin\Theta^\chi) I^\chi_z + (b \cos\Theta^\chi - \chi \sin\Theta^\chi) I^\chi_x \tag{3.15}$$

The off-diagonal elements in $(\mathcal{H}^T_\chi)_D$ are due to I^χ_x (remember I^χ_z is already diagonal). Thus, we can readily find a condition for diagonalisation:

$$\tan\Theta^\chi = \frac{b}{\chi}$$

Let us introduce a variable $\omega^\chi_e = \sqrt{b^2+\chi^2}$. We can now substitute the trigonometric functions in equation 3.15

$$\sin\Theta^\chi = \frac{b}{\omega^\chi_e} \quad \text{and} \quad \cos\Theta^\chi = \frac{\chi}{\omega^\chi_e} \tag{3.16}$$

Substituting this into equation 3.15 leads to

$$(\mathcal{H}^T_\chi)_D = (\chi\frac{\chi}{\omega^\chi_e} + b\frac{b}{\omega^\chi_e}) I^\chi_z = \omega^\chi_e I^\chi_z \tag{3.17}$$

Now that the Hamiltonian is transformed into a suitable frame of reference, the initial density matrix needs to be determined. It is then allowed to evolve under the calculated Hamiltonian and is used to determine the observables. The initial density matrix is given by

$$\rho^T(0) = I_z = I^\Omega_z + I^\Delta_z.$$

---

[3] The explicit form of matrices representing these operators is given in Appendix B

We have to bear in mind that, although we start after a preparational $\frac{\pi}{2}_y$-pulse, we have to transform the magnetisation along the x-axis into the *tilted* 'doubly rotating' frame.

Evolution in time under the Hamiltonian $\mathcal{H}_\chi^T$ is described by the following equation:

$$\begin{aligned}
\rho_\chi^T(t) &= e^{-i\mathcal{H}_\chi^T t}\rho_\chi^T(0)e^{i\mathcal{H}_\chi^T t} \\
&= \underbrace{e^{-i\Theta^\chi I_y^\chi}\overbrace{e^{-i\mathcal{H}_\chi^T t}\underbrace{e^{i\Theta^\chi I_y^\chi}\rho_\chi^T(0)e^{-i\Theta^\chi I_y^\chi}}_{1.}e^{i\mathcal{H}_\chi^T t}}^{2.}e^{i\Theta^\chi I_y^\chi}}_{3.} \qquad (3.18)
\end{aligned}$$

The braces in this equation describe the succeeding transformation in space and time, namely:

1. Transformation into the D-frame, in which the Hamiltonian is diagonal:

   $$\rho_\chi^T(0) = I_z^\chi \qquad (\rho_\chi^T(0))_D = \cos\Theta^\chi I_z^\chi - \sin\Theta^\chi I_x^\chi$$

2. Evolution in time under the Hamiltonian $(\mathcal{H}_\chi^T)_D$ as given in equation 3.17:

   $$e^{-i\mathcal{H}_\chi^T t}(\rho_\chi^T(0))_D e^{i\mathcal{H}_\chi^T t} = \cos\Theta^\chi I_z - \sin\Theta^\chi(\cos\omega_e^\chi t\ I_x^\chi + \sin\omega_e^\chi t\ I_y^\chi)$$

3. Finally, transformation from the D-frame back into the tilted frame (denoted by T):

$$\begin{aligned}
\rho_\chi^T(t) = e^{-i\Theta^\chi I_y^\chi}[\ldots]e^{i\Theta^\chi I_y^\chi} &= \cos\Theta^\chi(\cos\Theta^\chi I_z^\chi + \sin\Theta^\chi I_x^\chi) \\
&\quad - \sin\Theta^\chi(\cos\omega_e^\chi t\ (\cos\Theta^\chi I_x^\chi - \sin\Theta^\chi I_z^\chi) + \sin\omega_e^\chi t\ I_y^\chi) \\
&= I_x^\chi(\cos\Theta^\chi\sin\Theta^\chi - \cos\Theta^\chi\sin\Theta^\chi\cos\omega_e^\chi t) \\
&\quad + I_y^\chi(-\sin\Theta^\chi\sin\omega_e^\chi t) \\
&\quad + I_z^\chi(\cos^2\Theta^\chi + \sin\Theta^\chi\cos\omega_e^\chi t) \qquad (3.19)
\end{aligned}$$

To monitor the magnetisation we have to calculate the expectation value of S_z (S_x in the non-tilted 'doubly rotating' frame). Introducing $M_{eq} = \mathrm{Tr}\{S_z^2\}$ as the normalisation factor we have:

$$\frac{M_S(t)}{M_{eq}} = \frac{\gamma_I}{\gamma_S}\frac{\mathrm{Tr}\{\rho^T(t)S_z\}}{\mathrm{Tr}\{S_z^2\}}$$

The product of $I^X_{x,y}$ with S_z does not contribute any diagonal terms. Furthermore, we find $\mathrm{Tr}\{I^\Delta_z S_z\} = -\frac{1}{2}\mathrm{Tr}\{S^2_z\}$ and $\mathrm{Tr}\{I^\Omega_z S_z\} = \frac{1}{2}\mathrm{Tr}\{S^2_z\}$. Thus, the observed magnetisation will be:

$$\frac{M_S(t)}{M_{eq}} = \frac{\gamma_I}{2\gamma_S}(-\cos^2\Theta^\Delta - \sin^2\Theta^\Delta \cos\omega^\Delta_e t + \cos^2\Theta^\Omega + \sin^2\Theta^\Omega \cos\omega^\Omega_e t)$$

It makes sense to substitute again the trigonometric functions as was done in equation 3.16. In the limit of $|\Omega| = |\omega_{1I} + \omega_{1S}| \gg b$ we may find

$$\cos^2\Theta^\Omega = \frac{\Omega^2}{\Omega^2 + b^2} \approx 1 \qquad \sin^2\Theta^\Omega = \frac{b^2}{\Omega^2 + b^2} \approx 0$$

and, finally,

$$\frac{M_S(t)}{M_{eq}} \approx \frac{\gamma_I}{2\gamma_S}\frac{b^2}{\Delta^2 + b^2}(1 - \cos\omega^\Delta_e t) \tag{3.20}$$

This result means that magnetisation is oscillating between the I spin and the S spin reservoirs. This process is, in practice, damped by spin diffusion. Supposing that irradiation is done on resonance($\Delta = \omega_{1I} - \omega_{1S} = 0$), it would be found that $\omega^\Delta_e = b$ and the frequency of oscillation directly yields the dipolar coupling constant b as given in equation 3.12. If we were to observe cross polarisation in a powder and not in a single crystal, as Müller and co-workers did, we would find a distribution of these coupling constants. This distribution leads to destructive interference and a rapid damping of these oscillations. A powder average of the form

$$\frac{M_{S,\mathrm{powder}}(t)}{M_{eq}} = \int_0^{\frac{\pi}{2}} \frac{\gamma_I}{2\gamma_S}(1 - \cos(\kappa t(3\cos^2\Theta - 1))\sin\Theta \, d\Theta$$

yields the solution for dipolar oscillation in CP experiments of a powder sample. Figure 3.9 presents the dipolar oscillations calculated by this formula. The constant κ comprises all but the angle-dependent part of the coupling constant b (cf. equation 3.12).

3.1.4.1 Magic Angle Spinning

So far we have only considered the static powder case. Let us examine the assumptions made. In fact, only the dipolar coupling constant, which is the only geometry-dependent variable, becomes time-dependent as we spin the sample. The term $3\cos^2\Theta - 1$ can readily be expanded (see also [SM94] pp. 110):

$$\begin{aligned} b(t) &= -\frac{\mu_0\gamma_I\gamma_S\hbar}{4\pi r_k^3}\frac{1}{2}(\sqrt{2}\sin 2\beta\cos(\gamma + \omega_r t) + \sin^2\beta\cos 2(\gamma + \omega_r t)) \\ &= \delta_1\cos(\gamma + \omega_r t) + \delta_2\cos 2(\gamma + \omega_r t) \end{aligned} \tag{3.21}$$

The constant angle of the inter-nuclear vector to the axis of rotation is denoted by β. The angle $\gamma + \omega_r t$ describes the time-dependent angle of rotation with the angular rotation frequency ω_r. The azimuthal angle γ can be eliminated, thus saving one tedious transformation. This angle appears only as an initial 'phase' of rotation of the rotor. Without limiting our derivation to a special case, we can set $\gamma = 0$. δ_1 and δ_2 summarise the constants before the time-dependent cosines.

Again, it is useful to apply some transformation to the Hamiltonian prior to the actual calculation of observed magnetisation. In this case it will prove sensible to use a rotating frame with the rotation frequency $n\omega_r/2\pi$, with $n = 0, \pm1, \pm2$. If we denote the Hamiltonian in this new frame of reference by $\mathcal{H}^R_\chi(t)$ we obtain:

$$\begin{aligned}\mathcal{H}^R_\chi(t) &= -n\omega_r I^X_z + e^{in\omega_r t I^X_z}\mathcal{H}^T_\chi(t)e^{-in\omega_r t I^X_z} &\quad(3.22)\\ &= -n\omega_r I^X_z + \chi I^X_z + \delta_1 \cos\omega_r t\ \cos n\omega_r t\ I^X_x - \delta_1 \cos\omega_r t\ \sin n\omega_r t\ I^X_y\\ &\quad + \delta_2 \cos 2\omega_r t\ \cos n\omega_r t\ I^X_x - \delta_2 \cos 2\omega_r t\ \sin n\omega_r t\ I^X_y &\quad(3.23)\end{aligned}$$

In zeroth order we can calculate an average Hamiltonian over one rotor period.

$$\overline{\mathcal{H}^R_\chi} = \frac{1}{t_r}\int_0^{t_r} \mathcal{H}^R_\chi(t)dt \qquad \text{where } t_r = \frac{2\pi}{\omega_r}$$

Depending on $n = \pm1$ or $n = \pm2$ we obtain, after integrating equation 3.23, terms with either δ_1 or δ_2, because products of cosines with different frequencies average to zero. Thus, we may write

$$\overline{\mathcal{H}^R_\chi} = (\chi - n\omega_r)I^X_z + \frac{\delta_n}{2}I^X_x \qquad (3.24)$$

If we compare this sum with the expression given in equation 3.14 we find that merely the substitution of constants, $\chi \leftrightarrow \chi - n\omega_r$ and $b \leftrightarrow \frac{\delta_n}{2}$, reduces the MAS-Hamiltonian to the already solved static Hamiltonian. To diagonalise the Hamiltonian by rotation about the y-axis with an angle Θ^X we follow the same procedure as before and get:

$$\omega^X_e = \sqrt{\frac{\delta^2_n}{4} + (\chi - \omega_r n)^2}, \qquad \sin\Theta^X = \frac{\delta_n}{2\omega^X_e} \qquad \text{and} \qquad \cos\Theta^X = \frac{\chi - n\omega_r}{\omega^X_e}$$

$$\text{with} \qquad \delta_1 = \frac{\mu_0\gamma_I\gamma_S\hbar}{4\pi r^3_k}\frac{1}{2}\sqrt{2}\sin 2\beta = \kappa_1 \sin 2\beta \qquad (3.25)$$

$$\text{and} \qquad \delta_2 = \frac{\mu_0\gamma_I\gamma_S\hbar}{4\pi r^3_k}\frac{1}{2}\sin^2\beta = \kappa_2 \sin^2\beta$$

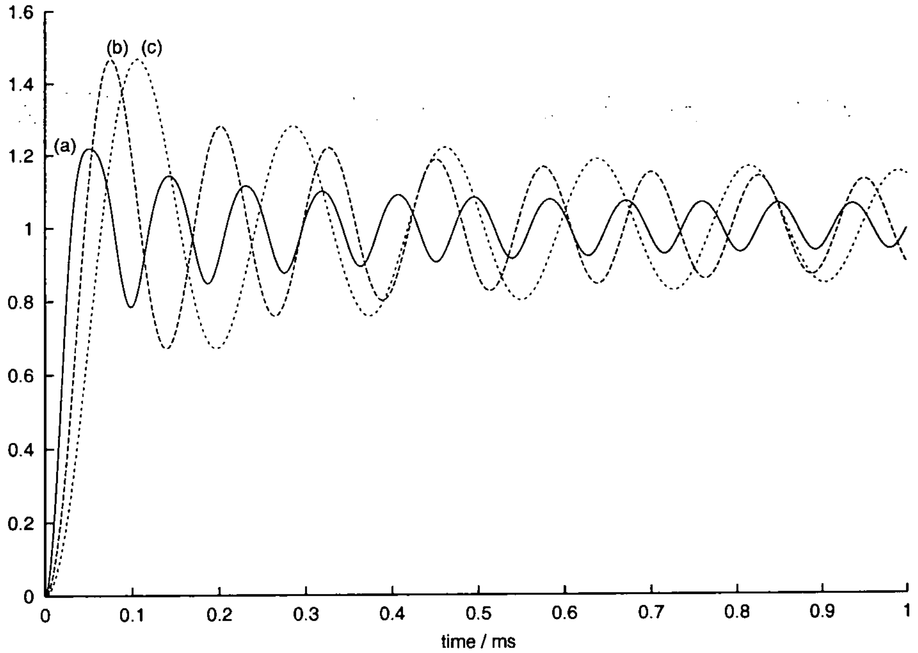

Figure 3.9: Simulation of dipolar oscillations of S spin reservoir magnetisation in a powder. (a) static, on resonance (b) MAS, $\Delta = \pm 1\omega_r$, (c) MAS, $\Delta = \pm 2\omega_r$. The parameters for the dipolar coupling constant are $\gamma_C = 6.728 \cdot 10^7$ rad $\mathrm{T}^{-1}\mathrm{s}^{-1}$, $\gamma_H = 26.752 \cdot 10^7$ rad $\mathrm{T}^{-1}\mathrm{s}^{-1}$, $r = 1.1$ Å. This results in oscillation frequencies (a) $\omega_{osc} = \kappa = 71.3 \times 10^3$ rad s^{-1}, (b) $\omega_{osc} = \omega_e^{\Delta} = \frac{\kappa_1}{2} = 50.4 \times 10^3$ rad s^{-1}, (c) $\omega_{osc} = \omega_e^{\Delta} = \frac{\kappa_2}{2} = 35.6 \times 10^3$ rad s^{-1}.

where we have introduced the angle-independent κ_1 and κ_2 for convenience. The initial density matrix is again given by

$$\rho^T(0) = I_z = I_z^{\Omega} + I_z^{\Delta} = \rho^R(0)$$

and evolves under time similar to $\rho^T(0)$ according to equation 3.18

$$\begin{aligned} \rho_\chi^R(t) &= e^{-i\overline{\mathcal{H}_\chi^R}t}\rho_\chi^R(0)e^{i\overline{\mathcal{H}_\chi^R}t} \\ &= e^{-i\Theta_\chi I_y^\chi}e^{-i\overline{\mathcal{H}_\chi^R}t}e^{i\Theta_\chi I_y^\chi}\rho_\chi^R(0)e^{-i\Theta_\chi I_y^\chi}e^{i\overline{\mathcal{H}_\chi^R}t}e^{i\Theta_\chi I_y^\chi} \end{aligned} \qquad (3.26)$$

This gives essentially identical expressions for the density matrix $\rho_\chi^R(t)$ as in 3.19. Now we need to transform this matrix from the rotating frame R back into the tilted rotating frame T. This reverse transformation (cf. 3.22) is given by:

$$\rho_\chi^T(t) = e^{-in\omega_r t I_z^\chi}\rho_\chi^R(t)e^{in\omega_r t I_z^\chi}$$

The rotation operator $e^{-in\omega_r t I_z^\chi}$ will leave terms with I_z unchanged. On the other hand, terms with I_x and I_y will split into components of I_x and I_y (which will make the equations rather cumbersome). But to calculate the observed magnetisation we

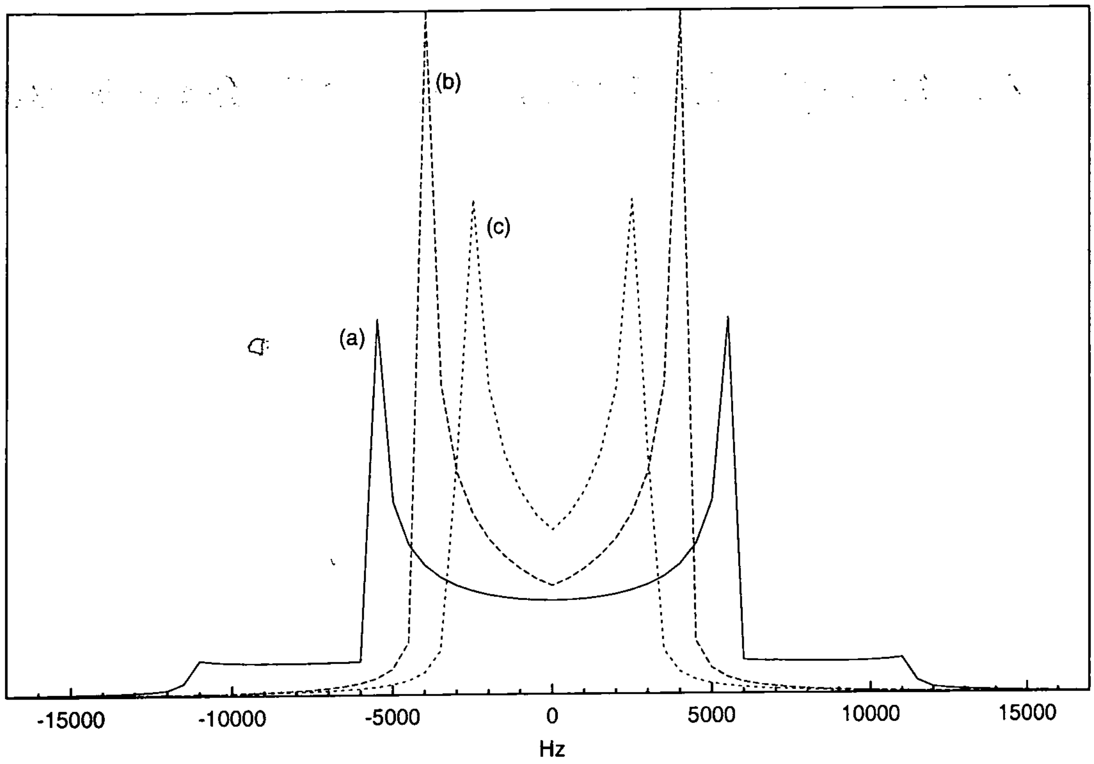

Figure 3.10: Fourier transformation of the simulated dipolar oscillations in a powder shown in Figure 3.9, with dipolar coupling constants as before but converted to kHz: static powder, on resonance, $\kappa = 11.3$ kHz (a); MAS, $\Delta = \pm 1\omega_r$, $\frac{1}{2}\kappa_1 = 8.0$ kHz (b); MAS, $\Delta = \pm 2\omega_r$, $\frac{1}{2}\kappa_2 = \frac{1}{2\sqrt{2}}\kappa_1 = 5.7$ kHz (c)

only need to consider terms contributing to $\mathrm{Tr}\{\rho^T(t)S_z\}$. Thus, we simply ignore terms in I_x and I_y and take the identical solution from equation 3.20, substituting ω_e^χ and χ in the appropriate way as described above:

$$\begin{aligned} \frac{M_S(t)}{M_{eq}} &\approx \frac{\gamma_I}{2\gamma_S}\sin^2\Theta^\Delta(1-\cos\omega_e^\Delta t) \\ &\approx \frac{\gamma_I}{2\gamma_S}\frac{\frac{\delta_n^2}{4}}{\frac{\delta_n^2}{4}+(\Delta-n\omega_r)^2}\left(1-\cos\sqrt{\frac{\delta_n^2}{4}+(\Delta-n\omega_r)^2}\;t\right) \end{aligned} \tag{3.27}$$

The graphical representation of this equation after calculating the powder average can be seen in Figure 3.9 in comparison with the static case. Note the two different oscillation frequencies for the two different rotational resonance conditions $n = \pm 1$ and $n = \pm 2$.

From these considerations we can conclude that it is in principle possible to determine dipolar coupling constants, and hence interatomic distances, by measuring transient oscillations in cross polarisation experiments. The system should meet the following conditions:

- The system should consist of a spin pair. It will be far more difficult to obtain solutions, let alone analytic expressions, for the case of more than two interacting spins.
- The systems should be rigid. A mobility of the order of or greater than ω_e clearly leads to a scaling of the coupling constant depending on the type of motion.
- Sources which damp oscillation, namely spin diffusion, interaction with surrounding spins and B_1 inhomogeneities, have to be neglected.

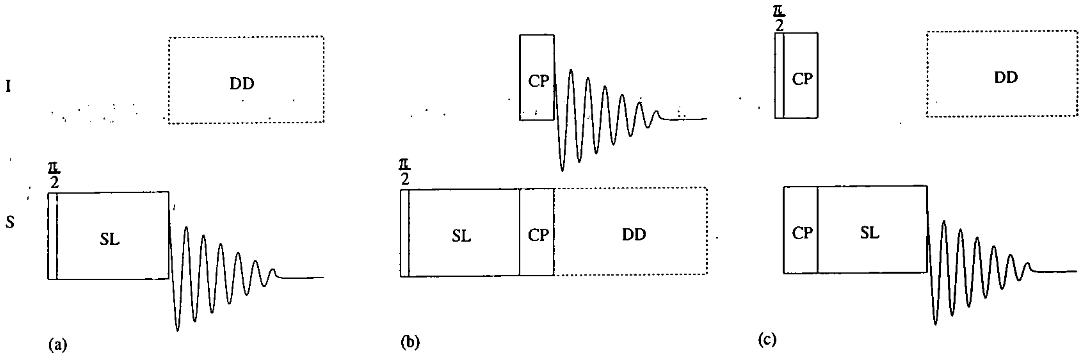

Figure 3.11: Schematic representation of the pulse sequences utilised to measure $T_{1\rho}^{S}$ by varying the time for the spin lock (a) direct measurement after spin lock (SL), (b) indirect measurement at the other channel after CP, (c) direct measurement but creation of magnetisation by CP rather than 90 ° pulse. Decoupling during acquisition is optional.

3.2 Experiments

In this section cross-polarisation experiments of fluoro compounds will be discussed. Experimental aspects of the theory of the preceding sections will be considered more closely. As mentioned in section 3.1.3, it is not feasible to yield all relaxation parameters of a system described by three spin baths by just one single fit. It has to be tried to gain knowledge of these values by manipulating the spin system and thus extracting the relaxation parameters piecewise.

3.2.1 Spin-Lattice Relaxation in the Rotating Frame

The first kind of value which is accessible without the complicating fact of heteronuclear cross relaxation is the spin-lattice relaxation parameter in the rotating frame, $T_{1\rho}$. In principle, there are three different methods of measuring this value, which are depicted in Figure 3.11.

Direct observation without CP (Figure 3.11a) is probably the simplest method but suffers from possible influence of a background signal, which will decay at its own characteristic rate. The indirect observation (Figure 3.11b) has the advantage of suppressing the background signal. Furthermore, it allows the measurement $T_{1\rho}$ values separately for different sites provided that the channel the signal is detected in gives the necessary spectral resolution. This is often the case for $T_{1\rho}^{H}$ detected at the carbon channel. Direct observation after CP (Figure 3.11c) is also used to suppress background signals. Also it avoids long recycle delays necessitated by high

number of components	direct (Fig 3.11a)		indirect (Fig 3.11b)			
	$T_{1\rho}^{H}$ in ms	relative intensity	$T_{1\rho}$(CFH) in ms	relative intensity	$T_{1\rho}$(CF_2) in ms	relative intensity
one	4.7±0.1	100%	5.3	100%	5.5	100%
two	6.7±0.1	(66±2)%	6.2	85%	6.1	91.5%
	1.4±0.05	(34±2)%	1.6	15%	0.9	8.5%

Table 3.1: $T_{1\rho}^{H}$ obtained directly and indirectly via the ^{19}F spectrum (CP: t_c = 0.5 ms) at 12 kHz MAS, with no decoupling during acquisition. Spin-lock field, B_1, was equivalent to 83 kHz.[4]

number of components	direct (Fig 3.11a)				direct (Fig 3.11c)	
	$T_{1\rho}$(CFH) in ms	relative intensity	$T_{1\rho}$(CF_2) in ms	relative intensity	$T_{1\rho}^{F}$(CFH) in ms	$T_{1\rho}^{F}$(CF_2) in ms
one	5.1	100%	4.3±0.1	100%	5.1	4.8
two	6.5	64%	6.5±0.7	(58±7)%	–	–
	3.0	36%	2.1±0.3	(42±7)%	–	–

Table 3.2: $T_{1\rho}^{F}$ obtained directly by spin lock lock at 12 kHz MAS, with no decoupling during acquisition. Spin-lock field, B_1, was equivalent to 83 kHz.[4]

values of T_1 of the nuclei of interest.

Tables 3.1 and 3.2 summarise values for spin-lattice relaxation in the rotating frame obtained for PTrFE.

$T_{1\rho}^{H}$ of proton was measured by the method of direct observation and indirect observation via CP from ^{19}F. As expected, the spectral resolution of the fluorine spectrum does not give different decay rates because only one kind of proton is present in the polymer chain. It becomes apparent most in the direct observation that a single-exponential fit does not reflect all the features of the relaxation mechanism (see Figure 3.12). Therefore, the results of a double-exponential fit are given in the second and third rows of the table. However, it should be mentioned that multi-exponential fits with exponents differing by less than one order of magnitude are prone to result in unreliable data. Furthermore, as has been shown by theoretical calculations by Mabboux et al.[MBTN97] and numerical simulations by Kenwright

---

[4] Errors given are asymptotic standard errors, giving the 95%-confidence interval. They should exemplify the quality of the parameters obtained from the fit.

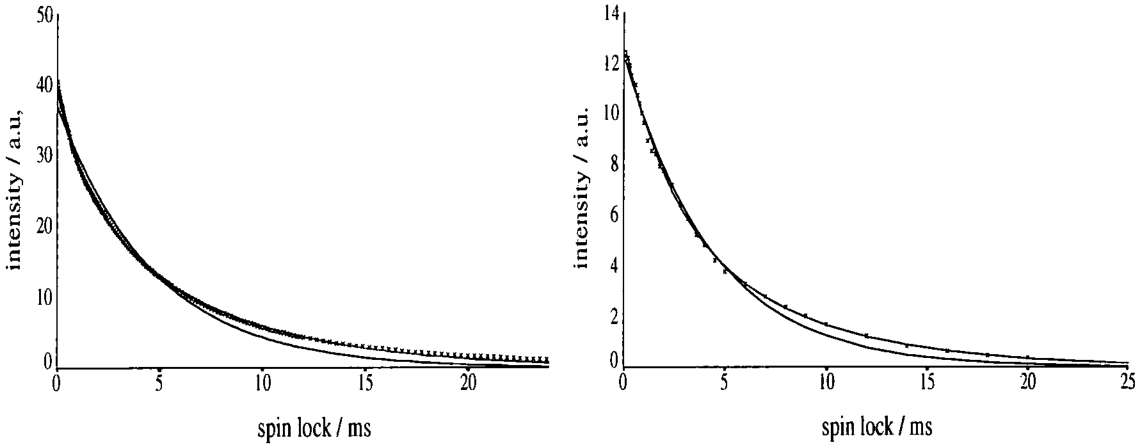

Figure 3.12: Direct measurement of $T_{1\rho}^{H}$ (left) and $T_{1\rho}^{F}$ (right). Experimental data (×) with single-exponential fit (solid black) and double-exponential (solid red) fit.

et al.[KPS86], two-component systems do not necessarily show two-exponential decays in T_1 and $T_{1\rho}$ data. Moreover, exponents of multi-exponential fits can not be connected with regions of different mobilities in a simplistic way. However, from the data presented it can still be inferred that at least a rigid component and a smaller mobile component are present.

$T_{1\rho}^{F}$ of fluorine was measured by two direct ways of observation, one of which directly polarises the fluorine spins (90°-pulse at the fluorine channel, see Figure 3.11a) and the other uses polarisation via cross polarisation from protons prior to the spin lock (see Figure 3.11c). The signal-to-noise ratio of the data of the latter experiment did not allow a reliable two-exponential fit. However, the data of the two methods yield quite similar results fot the single-exponential fit. This is due to the fact that the background signal, which would obscure the measured intensities, is weak compared to the strong fluorine signal of PTrFE.

3.2.2 Homonuclear Cross Relaxation

As proposed in section 3.1.3, an experiment to investigate homonuclear cross relaxation can be devised. This experiment, sketched in Figure 3.8 on page 44, was performed for fluorine. Two different experimental conditions were chosen. The standard MAS rate for PTrFE, ν_r, was 12 kHz. This allows observation of the fluorine resonances without overlapping of spinning sidebands and inherent peaks. Figure 3.13 shows the experimental results of the off-rotational-resonance condition,

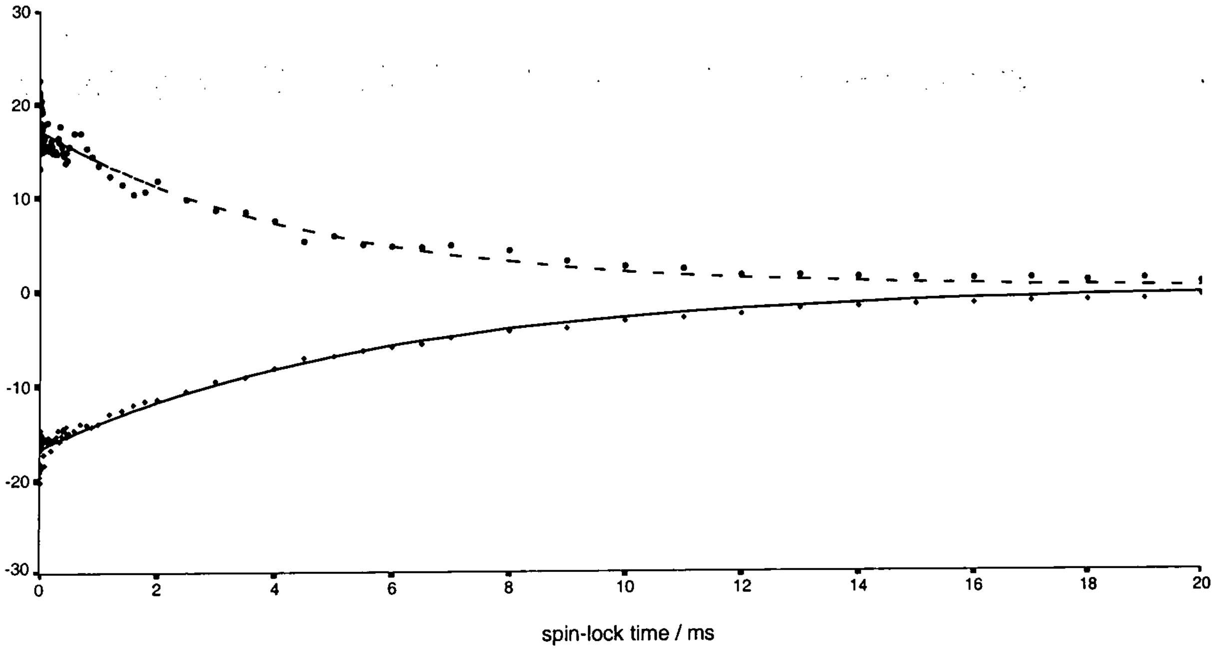

Figure 3.13: Selective polarisation inversion in the rotating frame (SPIRoF) of PTrFE at MAS 12 kHz. contact time 1 ms, delay between contact and spin lock τ =28 μs. Top curve: CF_2 fluorines (dashes); bottom curve: CFH fluorines (solid)

i.e. ν_r =12 kHz.

The results of the same experiment under the condition of rotational resonance are depicted in Figure 3.14. That means that an integer multiple of the spinning speed equals the chemical shift difference of the fluorine resonances. The experiment presented above is analogous to the rotational resonance experiment[RLG88] with longitudinal exchange of Zeeman order. The rotor-driven spin diffusion in the rotating frame is scaled by a factor of two and the relaxation is governed by $T_{1\rho}$ because the experiment is performed in the rotating frame. The limit of the spinning speed did not allow matching the rotational resonance condition $n = 1$ which corresponds ν_r =17 kHz due to the very big chemical shift difference of PTrFE. However, spinning speeds of 8.5 kHz, corresponding to $n = 2$, are well within the range of the HF MAS probe used. A drastic change compared to the off-resonance case described above can be noted.

The two data sets presented in Figures 3.13 and 3.14 were fitted with exponential decays, the results of which are summarised in the following table.

off-resonance, 12 kHz MAS		on-resonance, 8.5 kHz MAS	
CF_2	CFH	CF_2	CFH
4.6 ms	5.1 ms	490 μs	350 μs

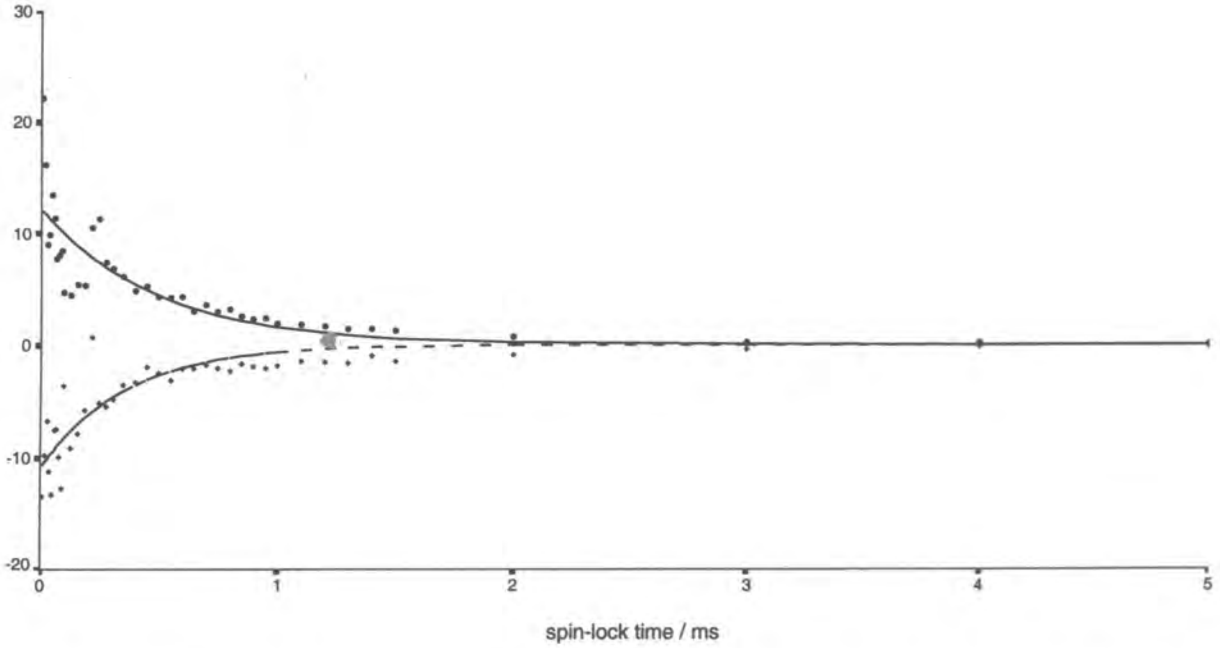

Figure 3.14: Selective polarisation inversion in the rotating frame (SPIRoF) of PTrFE at MAS 8.5 kHz, same conditions as in Figure 3.13

In Figure 3.13 decay rates of the two fluorine signals are observed in the range of $T_{1\rho}^{F}$ measured before. That means that no substantial cross relaxation occurs, i.e $T_{FF} \rightarrow \infty$. In the case of the on-rotational-resonance condition, however, the observed decay rates are much faster. As explained in section 3.1.3, we are facing the situation of two spin baths with two separate spin-lattice relaxation times and one cross-relaxation time, T_{FF}. The initial conditions, $\beta_{F,a}(0) > 0$ and $\beta_{F,b}(0) < 0$, differ from the standard CP case described at the beginning of this chapter (section 3.1.1). Still, the solutions to this system of two ordinary differential equations are a superposition of two exponentials. It has not been tried to perform this fit because of the low signal-to-noise ratio. Nevertheless, the fast decay, approximated by one exponential, reveals the main feature of the dynamics. As will be shown in the next section, the values presented are slightly bigger than cross-relaxation parameters for proton-fluorine interaction under Hartmann-Hahn matching conditions.

The conclusions from these two experiments are that homonuclear cross relaxation amongst fluorine spins is negligible under off-rotational-resonance conditions. However, if on-resonance conditions are met, this fluorine-fluorine cross relaxation becomes important. These two limits are demonstrated very clearly in the case of PTrFE, which has two distinct regions of resonance in the fluorine spectrum. Other

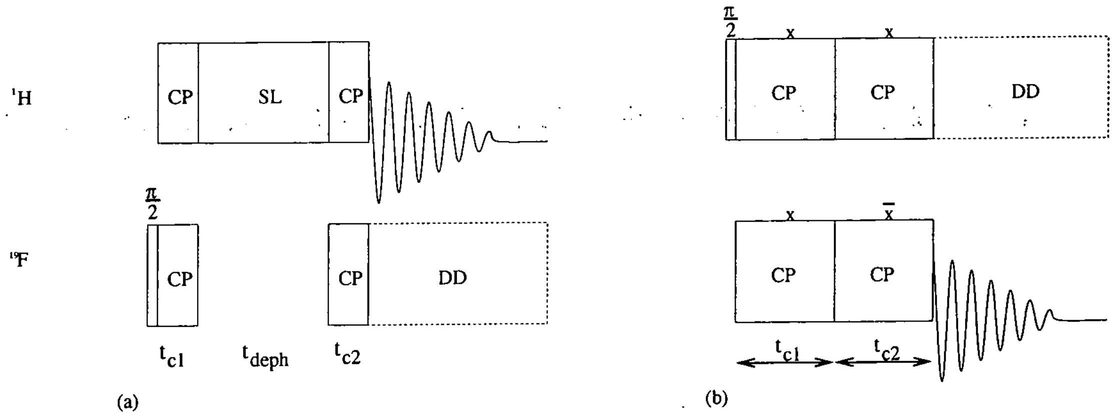

Figure 3.15: Schematic diagram of the pulse sequences used for CP drain (a) and Inversion-recovery cross polarisation (b)

fluoro compounds with a broader overlap of spectral bands due to a small spread in chemical shift or low mobility resulting in broad lines meet the on-resonance conditions for a very broad range of spinning speeds. For these, it will be much more difficult to eliminate the influence of homonuclear relaxation, e.g. by very fast spinning.

3.2.3 Heteronuclear Cross Relaxation

After considering homonuclear cross relaxation the heteronuclear relaxation between fluorine and proton will be examined. Two experiments, CP drain and inversion-recovery cross polarisation (IRCP), were used to scrutinise the short-time behaviour of cross-polarised systems.

The CP-drain pulse sequence is depicted in Figure 3.15a. In order to circumvent problems of proton background from the probe, essentially a double-CP experiment has been devised: The proton spins are polarised by CP from fluorine and spin locked for a time, t_{deph}, during which the fluorine spins dephase. Magnetisation is then transferred back to fluorine during a variable contact time, t_{c2}. The remaining magnetisation of the protons is monitored in the proton channel, optionally during fluorine decoupling. It should be pointed out that this pulse-sequence favours rigid regions insofar that the magnetisation of mobile domains decays more rapid during the spin-lock hold at the proton channel. This is of no influence in the case of PTrFE as this kind of selection does not work, as shown in section 2.2.1.

The results of the CP-drain experiment are shown in Figure 3.16. As can be seen, the experimental data are very well-fitted by a double-exponential decay describing

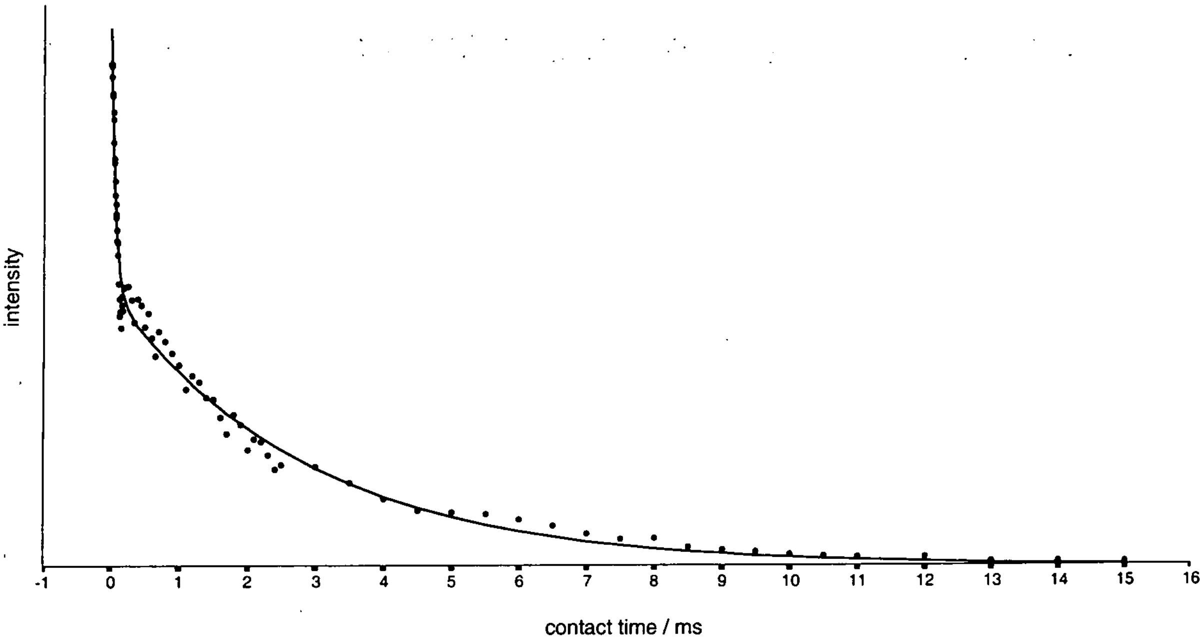

Figure 3.16: Remaining proton magnetisation after cross polarisation to fluorine as a function of the second contact time $t_{c,2}$. Results of fit: rapid decay with a time constant of 62 μs and a longer decay of 2.9 ms. Experimental conditions: MAS 12 kHz, initial contact time for polarisation of protons via CP from fluorine $t_{c,1}$ =0.4 ms, dephasing time of fluorine t_{deph} =5 ms

in first approximation the cross-relaxation between proton and fluorine and the spin-lattice relaxation of fluorine. The two decay rates are 62 μs for the first rapid decay and 2.9 ms for the longer decay. The second value seems short compared with the measurements listed in Table 3.1. This problem will be addressed in the next section.

Another approach to investigate short-time cross-polarisation behaviour is the inversion-recovery cross-polarisation pulse sequence (IRCP), originally introduced by Melchior[Mel81]. It is depicted in Figure 3.15b. The usual experimental condition for this experiment, as used for instance by Hirschinger and Reinheimer[HH94, RHGG97], involves a moderate cross-polarisation time, t_{c1}, before the phase of the spin-lock of either channels is shifted by 180°.

However, experiments on PTrFE show that only short contact times, $t_{c1} < 150$ μs, allow the observation of the expected behaviour of a signal inversion. This is readily explained by the comparatively small heat capacity of the protons in connection with a short $T_{1\rho}^{H}$. If t_{c1} is chosen too long, the remaining proton magnetisation is not big enough to invert the fluorine magnetisation during any contact time t_{c2}.

The results of the IRCP experiment on PTrFE are depicted in Figure 3.17. The

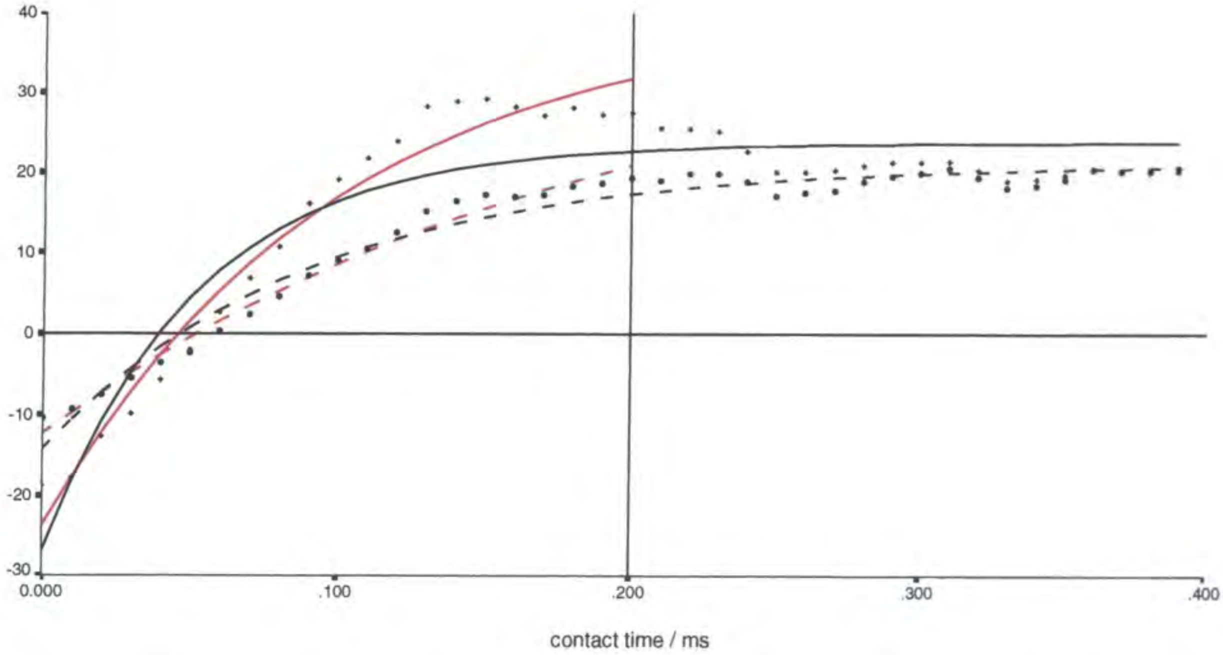

Figure 3.17: Experimental result and fit of IRCP experiment. Cross-relaxation times, T_{HF}, are estimated from the fit to $a \cdot e^{-t/T_{HF}} + b$: 50 μs for the CFH fluorine (solid) and 90 μs for the CF_2 fluorine (dashed). The same fit for the first points with $t_{c,2} < 200$ μs: 100 μs for the CFH fluorine (solid red) and 190 μs for the CF_2 fluorine (dashed red). Experimental conditions: initial contact time $t_{c,1} = 70$ μs, MAS at 12 kHz

two cross-relaxation parameters differ significantly in their size. The one for the CFH fluorine is shorter than that for the CF_2 group because the internuclear distance is shorter for the CFH group. It should be noted that the development of the fluorine magnetisation is not very well described by an exponential rise. Instead, a slight 'overshoot' becomes apparent. This is caused by a coherent polarisation transfer rather than an incoherent one. The latter can be described by the spin temperature approach whereas the former has to be accounted for by other methods. One of these is the treatment of transient oscillations between spin pairs (see section 3.1.4). To capture the coherent exchange rate better, a second fit to the data given for $0 < t_{c,2} < 200$ μs was tried. The results for T_{HF} are 100 μs and 190 μs for the CFH and CF_2 fluorine, respectively. An overshoot of the fluorine magnetisation can still be noted.

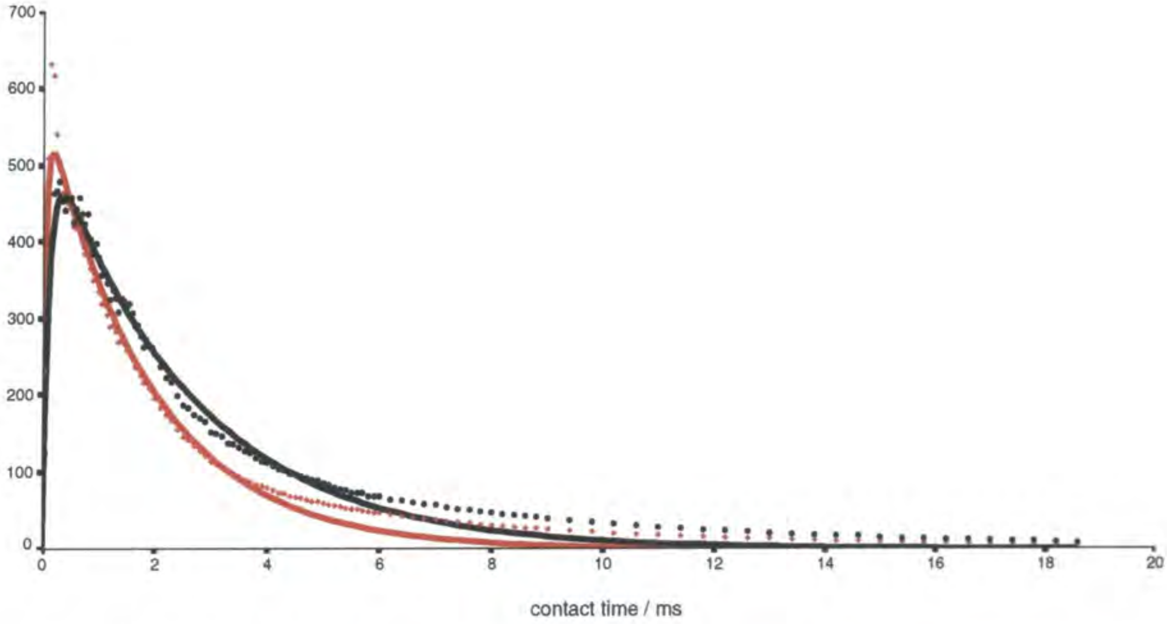

Figure 3.18: Variable contact-time cross-polarisation experiment of PTrFE. CFH fluorine magnetisation (red) and CF_2 magnetisation black. Solid curves are fits with the two-exponential equation derived from the spin-temperature model. Fitted exponents are, for CF_2 fluorine: $\alpha = 2.6$ ms and $\beta = 110$ μs; for CFH fluorine: $\alpha = 1.9$ ms and $\beta = 53$ μs. Equation see text.

3.2.4 Cross Polarisation of Two Spin Baths

To relate the results of the three-spin-bath model given in the next section, the model of two spin baths following from the description of Demco et al.[DTW75, Meh83] will be applied to the ^{1}H→ ^{19}F CP experiments. Figure 3.18 shows the experimental data fitted with a function of the form

$$I(t_c) = a(e^{-t/\alpha} - e^{-t/\beta})$$

In the limit of low abundance of the S spins ($\epsilon \to 0$) and long spin-lattice relaxation in the rotating frame ($T_{1\rho}^S \to \infty$) it can be shown that $\alpha = T_{1\rho}^H$ and $\beta = T_{HF}$. However, for the more general case the equations given in appendix A.1 have to be applied. With α and β given by the fit, one has to solve these equations for T_{HF} and either $T_{1\rho}^F$ or $T_{1\rho}^H$. Note that one of the spin-lattice relaxation values has to be fixed in order to get an unequivocal system of equations. Table 3.3 summarises the results obtained from the fits and the calculation.

As can be seen, no satisfying result for either of the spin-lattice relaxation times can be obtained, if the other is set constant. Moreover, only complex values for $T_{1\rho}$ satisfy the general Mehring equation given in the appendix if T_{HF} is set constant.

CF$_2$ fluorine			CFH fluorine			
$T_{1\rho}^H$	$T_{1\rho}^F$	T_{HF}	$T_{1\rho}^H$	$T_{1\rho}^F$	T_{HF}	
in ms		in μs	in ms		in μs	
4.6	2.2	450	*4.6*	1.6	220	$T_{1\rho}^H$ from Table 3.1
1.1	*4.3*	480	0.6	*5.1*	230	$T_{1\rho}^F$ from Table 3.2

Table 3.3: Fit parameters for cross polarisation of two spin baths. Fixed parameters are printed in *italics*. Experimental conditions: MAS 12 kHz, no decoupling during acquisition. The fits are displayed in Figure 3.18

3.2.5 Cross Polarisation of Three Spin Baths

As indicated in Appendix A.2, it is impractical to work with the general analytical solution to the system of ordinary differential equations presented in section 3.1.3. Many commonly used fit algorithms, such as the Levenberg-Marquardt algorithm, rely on the availability of analytical expressions for the fitted functions. Therefore a different method of fitting the parameters has to be found. The algorithm has to consist of the following steps:

1. Initialisation
2. Calculation of the residual sum of squares, χ^2, taking the current values of the parameters.
3. Change of the parameters in an appropriate way. This will, of course, change the matrix of coefficients, $\mathbf{A}$.
4. (Numerical) solution of the eigenvalue problem of the new matrix $\mathbf{A}$ as described in appendix A.2.
5. Back to step 2 unless an end criterion (e.g. no further improvement in the fit) is met.

It is worth mentioning that during every loop an eigenvalue problem has to be solved. This turns out to be a very time-expensive routine of fitting. Nonetheless, this method is justified as it can very easily be adapted to an algorithm, which is less prone to get stuck in local rather than global minima of the cost function χ^2 and is less sensitive to the initial guesses. In the present case the method of simulated annealing was used[5]. This is comparable to the process of slow annealing of a crystal melt in order to reach the global energy minimum – the perfect crystal lattice. The procedures used involved monitoring the development of χ^2 together with the change of the parameters. Thus, it was possible to estimate the dependence of χ^2 on the change of a particular parameter.

As mentioned before, eight parameters determine the magnetisation curve. It is, of course, beyond credibility to fit these parameters to one CP curve. This is not necessary, as the preceding sections were aimed at determining some of these parameters separately. The reliability of the fit was further improved by simultaneously fitting three curves of magnetisation, the two fluorine-peak intensities for the CFH and the CF_2 site observed in a variable contact-time experiment and the proton magnetisation measured with the CP-drain experiment.

The summary of the results of the fit with varying conditions is presented in Table 3.4. In the first row the results of a completely free fit are shown. Very soon during the fit procedure T_{FF} starts to diverge. This is in agreement with the results from the SPIRoF experiment discussed in section 3.2.2. There it was found that under off-rotational-resonance condition (MAS 12 kHz) no homonuclear cross relaxation between fluorines occured.

In order to determine cross-relaxation parameters independently from previous measurements it was tried to leave the spin-lattice relaxation parameters fixed at values determined from separate experiments (section 3.2.1). The second row shows the results of that fit. As expected and measured above, fluorine-fluorine relaxation tends to infinity. The values for proton-fluorine cross-relaxation are slightly larger than the values determined from the IRCP experiment in section 3.2.3. Still they are within experimental error. Figure 3.19 shows the corresponding magnetisation curves with their fit. Apparently, the spin-lattice relaxation parameters in the rotating frame are estimated too high while the rise characteristics of the two curves are described quite well. The fit of the remaining proton magnetisation (not shown) is of comparable quality to the fit displayed in Figure 3.16.

The opposite attempt, determination of $T_{1\rho}^{H}$, $T_{1\rho}^{F,a}$ and $T_{1\rho}^{F,b}$, turned out to be more complicated. To start with, cross-relaxation parameters were fixed to certain values.

---

[5] As this method is rather unusual, the programme code is partly listed in Appendix C.

χ^2	$T_{1\rho}^{H}$	$T_{1\rho}^{F,a}$	$T_{1\rho}^{F,b}$	$T_{HF,a}$	$T_{HF,b}$	T_{FF}	
	in ms			in μs			
112378	48	3.2	0.9	430	220	diverges	every parameter free
773509	*4.6*	*4.3*	*5.1*	290	140	diverges	fixed spin-lattice relaxation parameters
425317	diverges	4.5	0.9	*90*	*50*	∞	fixed cross-relaxation parameters
250770	diverges	4.1	0.9	*190*	*100*	∞	fixed cross-relaxation parameters
166310	diverges	4.1	0.8	*290*	*140*	∞	fixed cross-relaxation parameters
262465	*2.9*	5.9	1.1	*190*	*100*	∞	fixed cross-relaxation parameters and $T_{1\rho}^{H}$
261023	*4.6*	5.0	1.0	*190*	*100*	∞	fixed cross-relaxation parameters and $T_{1\rho}^{H}$

Table 3.4: Fit parameters for cross polarisation of three spin baths. Fixed parameters are printed in *italics*. Experimental conditions: MAS 12 kHz, no decoupling during acquisition, details for CP-drain experiment see Figure 3.16

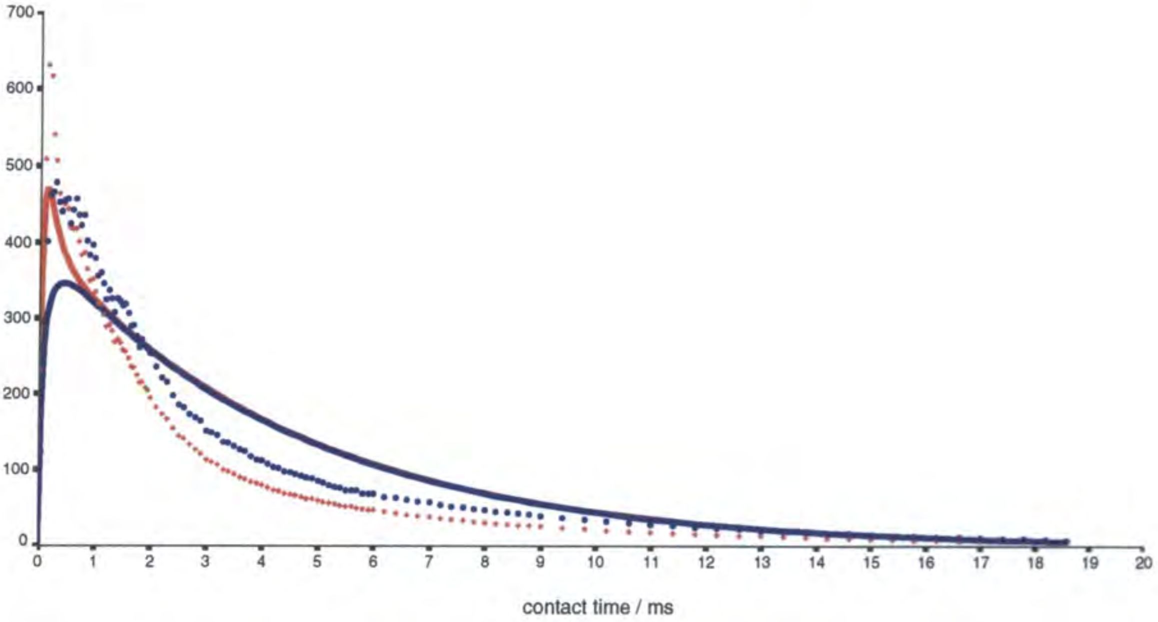

Figure 3.19: Variable contact-time cross-polarisation experiment of PTrFE. CFH fluorine magnetisation (red) and CF_2 magnetisation blue. Solid curves are fits determined by parameters given in Table 3.4 row 2. Note that $T_{1\rho}$ values are fixed, which leads to the inappropriate fit for the decay.

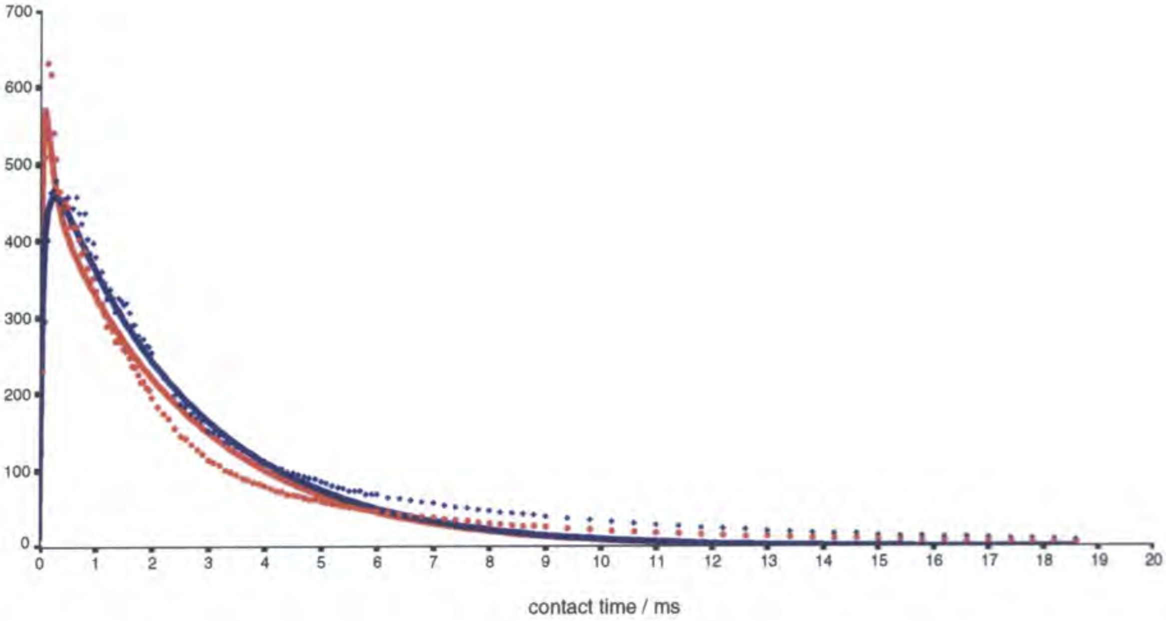

Figure 3.20: Variable contact-time cross-polarisation experiment of PTrFE. CFH fluorine magnetisation (red) and CF_2 magnetisation blue. Solid curves are fits determined by parameters given in Table 3.4 row 7.

For all cases T_{FF} was set to infinity. Values for $T_{HF,a}$ and $T_{HF,b}$ were determined from the IRCP experiment(see Figure 3.17)and the results are displayed in rows three and four of Table 3.4. The results shown in row five are fitted with fixed $T_{HF,a}$ and $T_{HF,b}$ taken from row one of Table 3.4. The result always seemed to be the same. The two values for $T_{1\rho}^{F,a}$ and $T_{1\rho}^{F,b}$ levelled off at their respective values of around 4 ms and 1 ms. Only $T_{1\rho}^{H}$ diverged. Closer scrutiny yielded that χ^2 was influenced by less than 1% if $T_{1\rho}^{H}$ was changed from 5 to 50 ms. Consequently, $T_{1\rho}^{H}$ can not be determined that way.

That is why a fit with constant $T_{1\rho}^{H}$ was tried, the result of which is presented in rows six and seven of Table 3.4. A comparison of the quality of the fit with trials of free $T_{1\rho}^{H}$ shows that a fixed $T_{1\rho}^{H} = 4.6$ ms increases the cost function, χ^2, by less than 4%. As this value complies with previous results it must be accepted as the value for $T_{1\rho}^{H}$. Figures 3.20 and 3.21 present the same experimental data as in Figure 3.19 and 3.16, respectively, but with the fitted curves the parameters of which are listed in row seven of Table 3.4. As can be seen, reasonable fits have been found.

Nonetheless, the dissatisfyingly short $T_{1\rho}^{F,b}$ calls for an explanation. If sufficiently long cross-relaxation times are paired with spin-lattice relaxation in the rotating frame at different rates for different sorts of nuclei, the inherently different $T_{1\rho}$'s

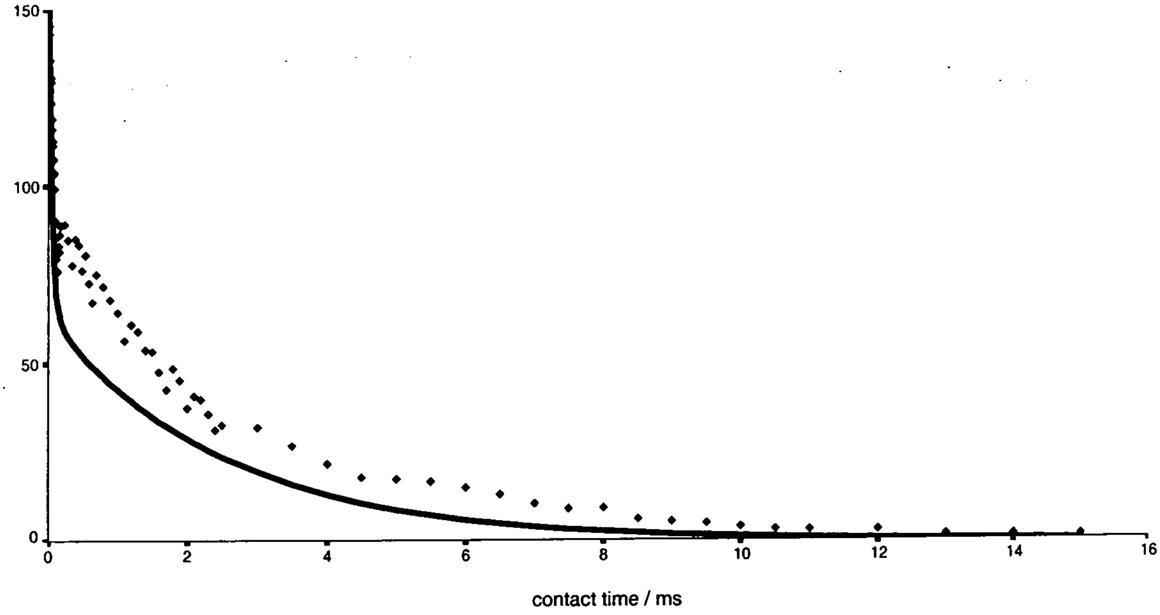

Figure 3.21: Variable contact-time cross-polarisation drain experiment of PTrFE. Experimental conditions as in Figure 3.16. Fit determined by parameters given in Table 3.4 row 7.

will manifest themselves in characteristic decays for the respective spin bath. If one of the spin baths were to relax quicker than another and the spin baths were in mutual contact via short values of T_{HF} or T_{FF}, then the latter spin bath would relax partly 'through' the faster relaxing nucleus. The experimental observation would be an averaged $T_{1\rho}$ for the two different nuclei, although the observed decay would exhibit features of a non-single-exponential function. Notwithstanding that complicated flow of magnetisation, the three-spin-bath model is designed to account for such mechanisms. Equally, though, an additional feature in the CP-curve, which in first order might be approximated by a single-exponential decay, can cause this model to produce false values. As known from previous experiments, $T_{1\rho}$ values for protons and fluorines of PTrFE are all about the same magnitude. The short value of $T_{1\rho}^{F,b} \approx 1$ ms can be attributed to the rapid and transient decay after the initial transient increase in magnetisation for cross-polarisation times $t_c < 0.5$ ms. It can not be ascribed in a simplistic manner to one sort of spins.

The results of the spin-temperature approach for describing the CP dynamics of PTrFE can be summarised as follows. Homonuclear cross relaxation is negligible for systems not matching the rotational-resonance condition, as has been shown by the SPIRoF experiment and results from the fits of the three-spin-bath model to experimental curves of the variable contact-time experiment and the CP drain. Heteronuclear cross relaxation can be determined by CP-drain and IRCP. Both experiments show that the thermodynamic approach reaches its limits at very short times as coherent transfer occurs. In practise, the fits give shorter cross relaxation times than expected for spin systems in quasi equilibrium created e.g. by efficient spin diffusion. Experimental data prove and theoretical treatment shows that the rapidly transferred magnetisation decays again very fast in a non-exponential manner. To account for that with exponential decays, originating from the spin-temperature approach, shorter $T_{1\rho}$ values have to be assumed than would be measured with separate methods.

Consequently, the dynamics of ^{1}H→ ^{19}F CP of PTrFE is to be understood as a superposition of a transient behaviour detectable in the very early stage and a process describable by the thermodynamic approach. In essence, the rapidly damped transient oscillation is comparable to an FID of the static-proton type. This FID is extremely distorted by a 'baseline', the CP curve without transient effects, determined by relaxation parameters described by the spin-temperature model.

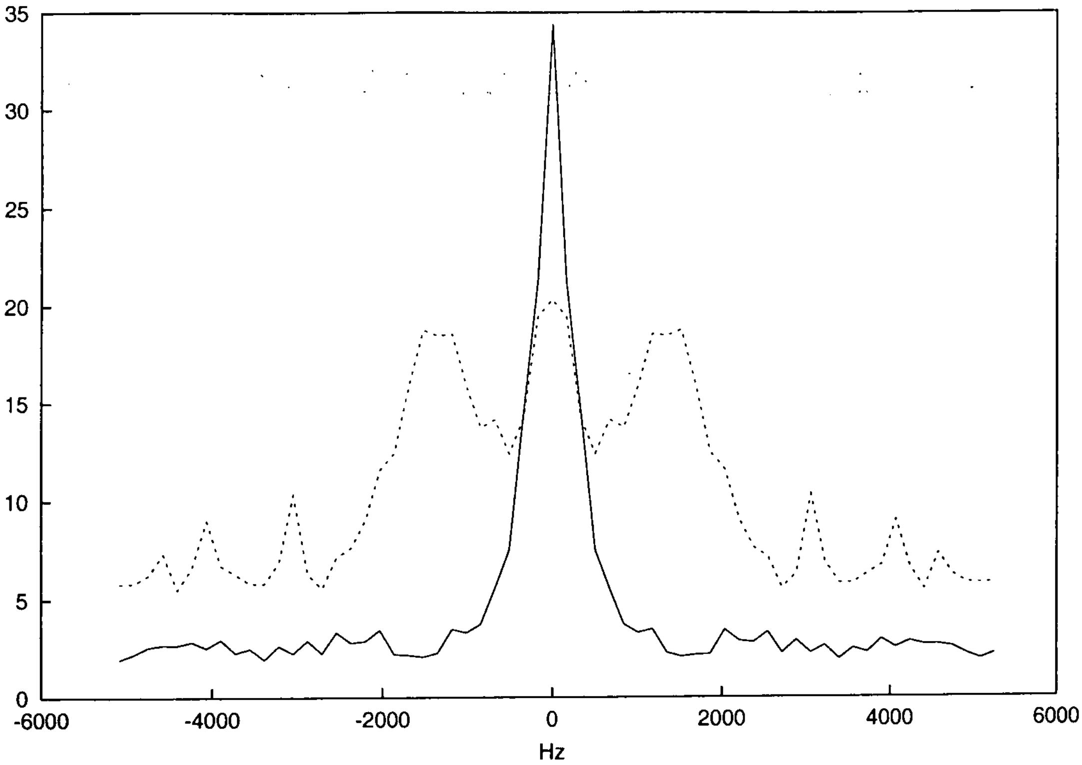

Figure 3.22: Fourier transformation of the dipolar oscillations in a powder of PTrFE at ambient temperature. The CFH carbon(dashed) exhibits a doublet with a peak separation of 3 kHz whereas the CF_2 carbon only has one peak.

3.2.6 Transient Oscillations

The theoretical treatment of coherent polarisation transfer resulting in transient oscillations during CP contact has been presented in section 3.1.4. As touched upon in the last chapter, coherent transfer during $^1H \rightarrow {}^{19}F$ CP can be observed in PTrFE. In principle, PTrFE presents us with three pairs of nuclei suitable for cross polarisation: $^1H \rightarrow^{19} F$, $^1H \rightarrow^{13} C$ and $^{19}F \rightarrow^{13} C$. However, a condition for observing dipolar oscillations which can be straightforwardly analysed is that a situation of more or less dilute spin pairs is present. This approximation is most valid for the case of $^1H \rightarrow {}^{13}C$ CP.

The analysis of the transient oscillation measured consists of the Fourier transformation of the integral intensity of the carbon peaks measured at equidistant intervals of contact time. Offsets, exponential rise and decay of the magnetisation curves lead to peaks at zero frequency with linewidths corresponding to the respective decay rates. An exponential fit has been subtracted from the magnetisation curves in order not to obscure the spectrum by spikes at zero frequency. Minor peaks still

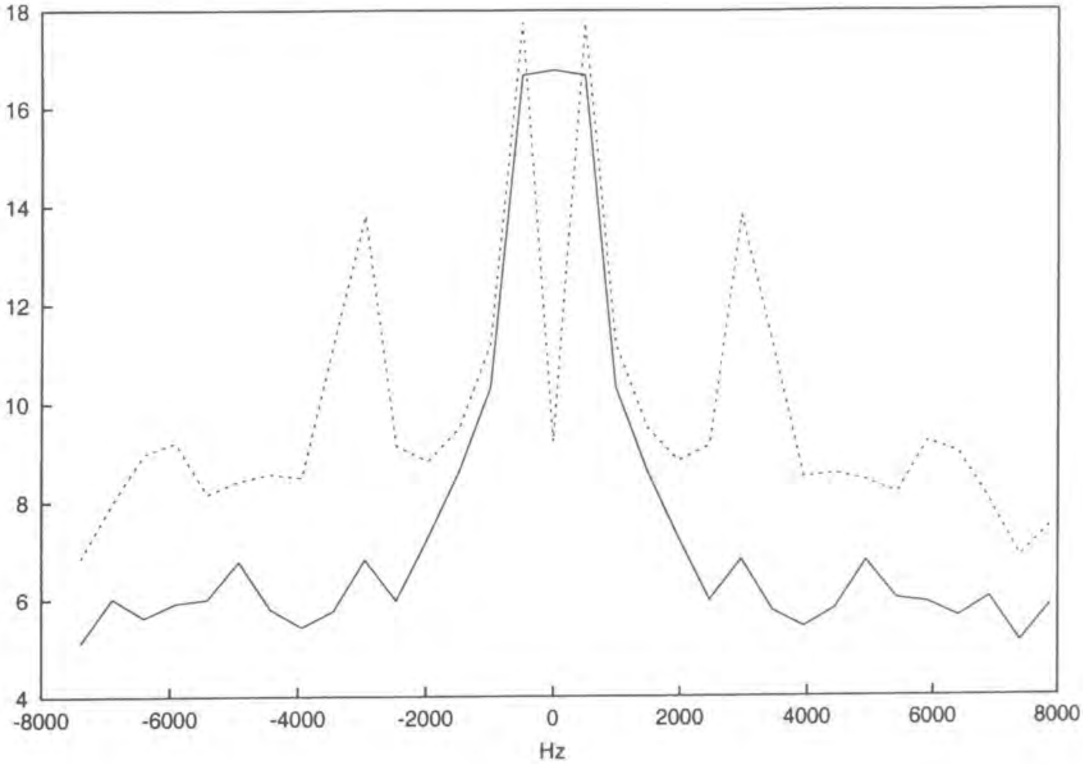

Figure 3.23: Fourier transformation of the dipolar oscillations in a powder of PTrFE at T=-30 °C. The CFH carbon(dashed) exhibits a doublet with a peak separation of 5.5 kHz and a central 'doublet' arising from incomplete correction of the baseline. The CF_2 carbon shows only one peak.

remaining at this position can be ignored for the purpose of our investigation. As pointed out by Hirschinger et al.[HH94, RHGG97], the IRCP experiment has the advantage of showing more pronounced oscillations while still being describable by the same theoretical model. That is why data from IRCP experiments were taken in order to determine dipolar coupling constants.

Figure 3.22 shows the Fourier transformation of the intensity curve in an IRCP experiment of the carbons at the CFH and CF_2 carbon. The CF_2 carbon shows a peak at zero frequency. The CFH carbon, however shows a clear doublet with a peak separation of 3 kHz. This corresponds to a proton–carbon distance of 1.5 Å evaluated using equation 3.25 on page 50. Surely, this distant is too long, if it is compared with the bond distances given in Table 2.2. Nonetheless, a coupling constant of that size is possible if one allows for molecular motion (for instant chain rotation) which leads to a scaling depending on the type of motion.

To test this hypothesis it was attempted to freeze out this motion. The same experiment was repeated at a lower temperature, $T = -30$ °C(nominal). Prior

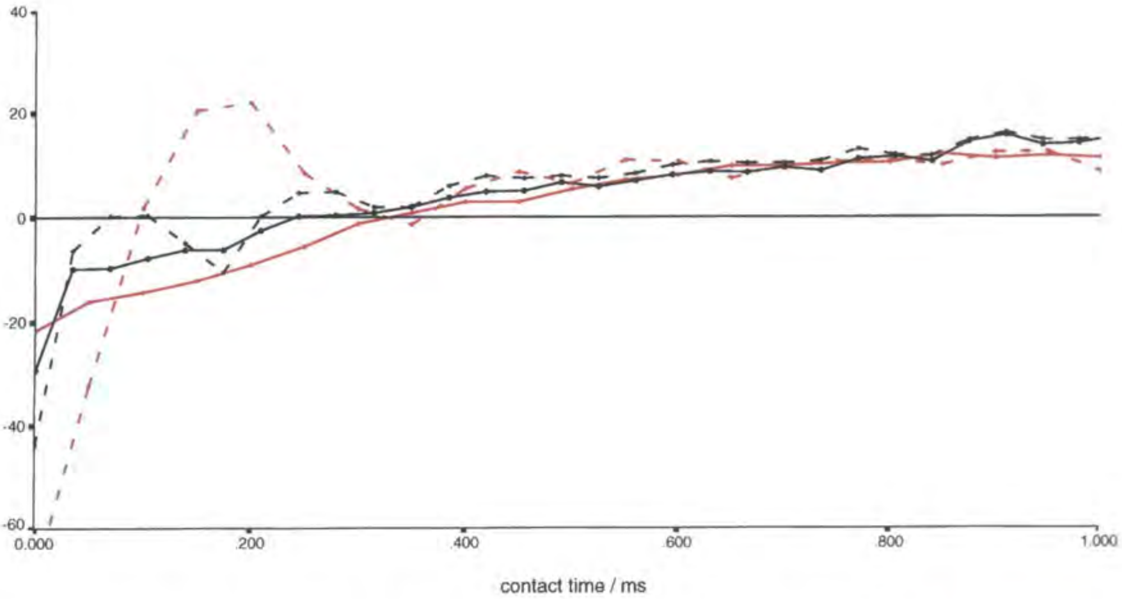

Figure 3.24: Comparison of the contact-time dependence of the dipolar oscillation in a powder of PTrFE. The CFH carbon(dashed) exhibits oscillations whereas the CF_2 carbon (solid) shows only an incoherent polarisation by the distant proton. The experiment has been performed at ambient temperature (red) and $T = -30$ °C (black). Fourier transformations of the plots can be seen in Figures 3.22 and 3.23, respectively.

to Fourier transformation an exponential function was subtracted. Although this does not fully describe the 'incoherent' offset, major peaks at zero frequency can be avoided.

The separation of 6 kHz for the CFH carbon powder doublet corresponds to a internuclear distance of 1.2 Å between fluorine and carbon. Although this is still slightly larger than the theoretical value gained from ab initio calculations (see Table 2.2 in section 2.2), it is within experimental error. That means that chain rotation, which is most likely to cause a scaling of the coupling constant by a factor of 2, has stopped in PTrFE at temperatures at -30 °C.

3.3 Summary

In the course of this chapter a three-spin-bath model was developed and applied to poly(trifluoroethylene) (PTrFE). As shown by the theoretical treatment, this model is suitable for a range of experiments of the cross-polarisation type. It was pointed out that the model relies on the input of data from separate experiments determining certain parameters and eliminating the influence of others. The cross-polarisation dynamics in PTrFE were fitted reasonably with this model. However, some of the parameters, in particular $T_{1\rho}^{F,b}$, did not agree with separate experiments performed before. This could be explained by the transient effect of a coherent magnetisation exchange. This coherent exchange has been described theoretically by others and was exploited for distance measurements in PTrFE by carefully studying early-stage ^{1}H→ ^{13}C CP. Also, the onset of motion, probably chain rotation, between −30°C and ambient temperature could be detected.

As mentioned above, cross polarisation in systems with abundant I and S spins consists of coherent as well as incoherent exchange. Models for both limits have been presented in the past and have proved to deliver a wealth of information about the systems involved. It appears that cross-polarisation dynamics of fluoro compounds can be tackled from two sides:

- Systems which approach either of the limits would be a good starting point to study the already known models for the special case of ^{1}H→ ^{19}F CP. These limits can be reached to a certain extent by changing experimental conditions, such as high spinning speeds to suppress spin diffusion or rotational resonance conditions to favour homonuclear spin diffusion.

- A model combining both features, that of the coherent and incoherent exchange, should be devised. A start might be the deconvolution of the CP curve into a transient 'FID-like' part and a thermodynamically describable curve ('baseline'). Parameters for this peeling could be won from separate experiments.

Chapter 4

NMR of Polyanilines

4.1 Introduction

Polyaniline (PANi) has been of great scientific interest because of its promising properties, such as processibility and conductivity, which suggests applications as a material for electrodes of secondary batteries, electrical and optical devices, and electrochromic devices. Polymers of the PANi-family can be processed, are air stable (in most of the relevant cases) and possess interesting electrical and optical properties[Mon92]. Their structure is shown schematically in Figure 4.1.

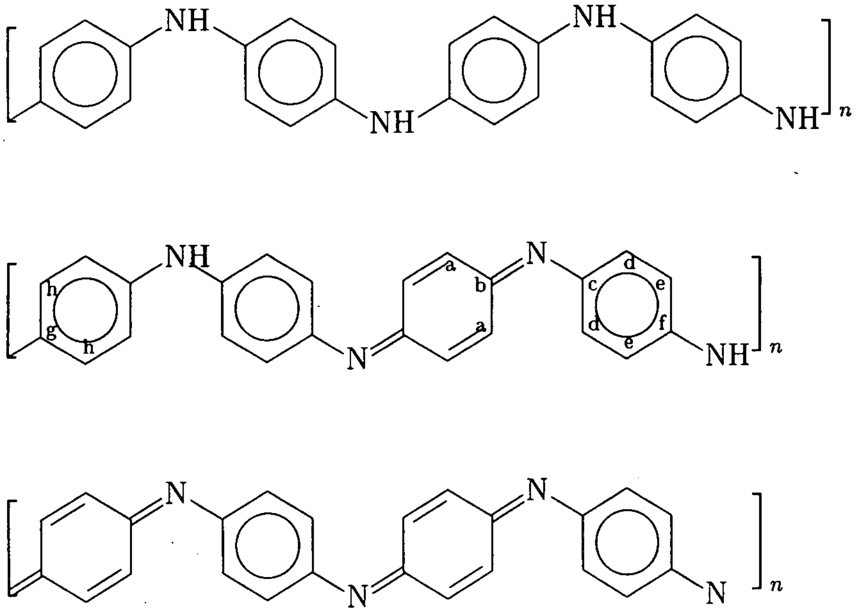

Figure 4.1: Chemical structure of Polyanilines: top: leucoemeraldine base (LEB), middle: emeraldine base (EB), bottom: pernigraniline base (PNB)

If we adopt the notation of Kaplan et al.[KCRM88] the unprotonated forms of PANi can be represented as follows:

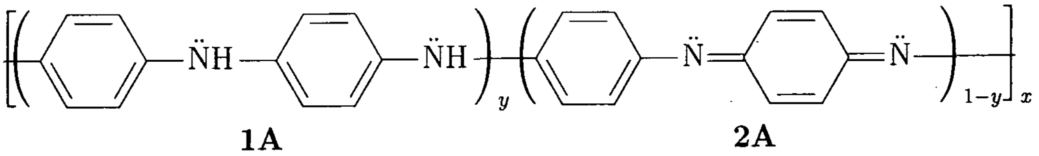

The six basic repeat unit building blocks are designated by **1**: reduced or **2**: oxidised, followed by **A**: amine/imine base, **S'**: monoprotonated salt, or **S"**: diprotonated salt. Different values for y describe the three principal oxidation states of the family of polyanilines:

- fully reduced leucoemeraldine base (LEB: $y = 1$, consecutive **1A** units),
- partially oxidised emeraldine base (EB: $y = 0.5$, alternating[1] **1A** and **2A** units), and
- fully oxidised pernigraniline base (PNB: $y = 0$, consecutive **2A** units).

These polymers can also exist in their corresponding protonated (salt) forms.

The reduced polymer, leucoemeraldine base, which is insulating, exhibits interesting optical properties. Its simple structure makes it ideally suited as model substance. Work on LEB is complicated by the fact that LEB is easily oxidised to emeraldine salt and to PNB by air.

A great deal of experimental work has been and still is devoted to emeraldine base and its salt, emeraldine salt (ES), because of its excellent environmental stability and conductivity. ES is the highly conducting form of PANi. It exhibits metallic-like optical absorption and reflection spectra. Conductivities up to 967±30 S/cm in drawn films (cf. conductivity of copper $6 \cdot 10^5$ S/cm) have been reported[APA+97], which is some 14 orders higher than in the insulating emeraldine base form. This can be even higher (ca. 2000 S/cm) in drawn fibres[AM98]. The transition from non-conducting to conducting polymer occurs under protonation (with acids such as HCl or camphorsulphonic acid, CSA) of the emeraldine base whereby the number of electrons along the chain remains constant.

---

[1] It is not trivial that we should expect *alternating* units. Kaplan et al.[KCRM88] showed by solid-state ^{13}C NMR that this is indeed the case for chemically polymerised aniline similar to the compounds described in this chapter.

Pernigraniline base, the fully oxidised material, contains alternating benzenoid and iminoquinoid moieties. It is insulating but shows remarkable optical properties.

4.2 Synthesis of Polyaniline

Polyaniline can be synthesised either chemically or electrochemically. Because the former leads to longer polymer chain lengths, it was decided to follow this route. The scheme of reaction described in detail by Adams et al.[AM97] was the one which was chosen for preparation of samples for the work reported in this chapter. Powder, films and solutions of LEB and EB have been produced as follows.

4.2.1 Emeraldine Base

Aniline hydrochloride (25.92 g, 0.2 mol) was dissolved in water (200 g) and stirred. Lithium chloride (LiCl, 42.04 g, 0.992 mol) was added in order to allow the solution to be cooled to -25^{o}C without freezing. 10 drops of HCl (37%) were added to bring the pH down to ~1. The solution was cooled to -25^{o}C and stirred at 300 rpm. Ammonium persulfate ($(NH_4)_2S_2O_8$, 57.05 g, 0.25 mol) was diluted with water (solution made up to 160 g). The oxidant solution produced was added with an peristaltic pump over a time of about 14 hours. The reaction was then continued for another seven hours. The reaction mixture was filtered using a Buchner funnel and flask. The filter cake was washed with deionised water before it was stirred in ammonium hydroxide solution (33%), followed by rewashing in deionised water and drying under vacuum for 24 hours to give a dark brown powder, which corresponds to 95% yield based on the aniline starting material (M_w = 90.93 g mol^{-1}, 17.2 g of PANi(EB) powder obtained). The vacuum-dried powder has been used for solid-state NMR experiments as is.

In order to produce films of emeraldine base, the powdered polymer was dissolved in anhydrous N-methyl-2-pyrrolidinone (NMP) and homogenised. A deep blue solution was obtained. A drop of the solution was deposited onto the substrates (quartz-glass) and dried under vacuum for 12 hours to give films of blue colour. These films could be peeled off if free-standing films were needed (e.g. for some light-excitation experiments under NMR observation)

For solution-state NMR measurements the samples were prepared by dissolving the emeraldine base powder (0.025 g) in NMP (5.00 g) and dimethyl sulfoxide-d_6 (DMSO-d_6, 0.75 g) and homogenising in a glove box under a nitrogen atmosphere for 3 minutes. 0.6 g of the solution was transferred to a 5 mm NMR tube. The solution was quite viscous and was therefore diluted further with DMSO-d_6 (0.075 g) (final concentration of the solid 1.85% by mass).

4.2.2 Leucoemeraldine Base

Solid leucoemeraldine base was produced by adding hydrazine monohydrate in excess to emeraldine. This was carried out in a glove box in a nitrogen atmosphere. It was then ground for 30 minutes to permit close contact between the liquid and the solid polymer. After allowing the polymer to react for another 12 hours it was finally dried under vacuum for ten hours. The powder obtained had a colour between grey and very light blue. Normally, it oxidises under air within minutes to a green/black powder. Therefore, for solid-state NMR the powder was put into a 5mm glass tube, evacuated, and glass sealed.

Films of leucoemeraldine base were produced from the bulk polymer dissolved in NMP. A drop of the clear solution was deposited onto the substrates (quartz-glass) which were dried under vacuum for at least 12 hours in the same manner as the emeraldine base films. It was noted that the longer the films were dried under vacuum the slower they oxidise when exposed to air for a short period.

Solution-state NMR samples of leucoemeraldine base were produced by adding hydrazine monohydrate to the solution of emeraldine base (prepared for solution-state NMR as described in section 4.2.1) and stirring for ten minutes under nitrogen. The solution slowly turned from blue to grey/brown and became much less viscous. Approximately 1.2 g of this solution was added to a 5 mm diameter NMR tube, which was evacuated and glass sealed to prevent any air re-entering the tube. (Concentration of this solution ~4% leucoemeraldine base w/w)

4.3 Optical Experiments on Polyaniline

Considerable progress has been made in describing and understanding optical properties of PANi[Mon92]. However, for the present work UV/VIS-spectroscopy has not been used to scrutinise chemical structure and motion, as has been done by others. It has been used here merely as a tool to check the quality of the polyaniline produced. Thus, it was possible to ensure that further investigations could be consistently carried out on high-quality material.

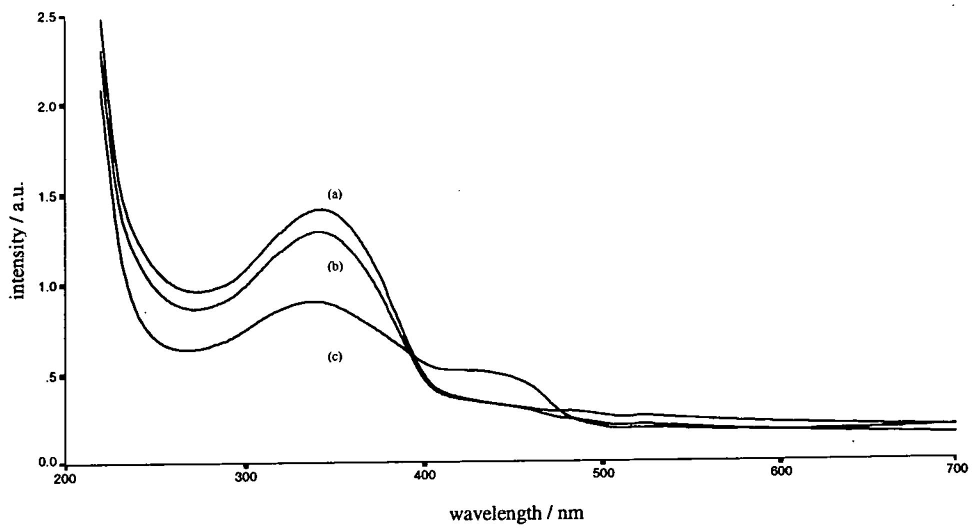

Figure 4.2: comparison of UV/VIS-spectra of differently prepared leucoemeraldine base films on quartz substrates. LEB in nitrogen atmosphere(a), LEB after exposure to air for 44 hours (b), LEB after exposure to air and then to nitric acid for a few seconds (c)

Figure 4.2(a) shows the UV/VIS spectrum of a film of leucoemeraldine base prepared as described in section 4.2.2. Curves (b) and (c) show the same film after exposure to air for 44 hours and to the vapour of nitric acid for a few second, respectively. During the first hours of air-exposure no change in the spectrum was noted. All spectra exhibit a prominent peak at 350 nm which is ascribed to the $\pi \rightarrow \pi^*$ transition of the benzenoid rings. The intensity of this peak is weakened by oxidisation of the polymer (curve (c)). Furthermore a peak in the visible spectrum at 440 nm appears, which indicates the build-up of leucoemeraldine salt. The transparent film turns green upon oxidisation.

Emeraldine base shows basically two distinct peaks in the recorded region, as shown in Figure 4.3. The first peak, which is again due to the $\pi \rightarrow \pi^*$ transition of the benzenoid rings, appears at 350 nm. The second broader band is to be found

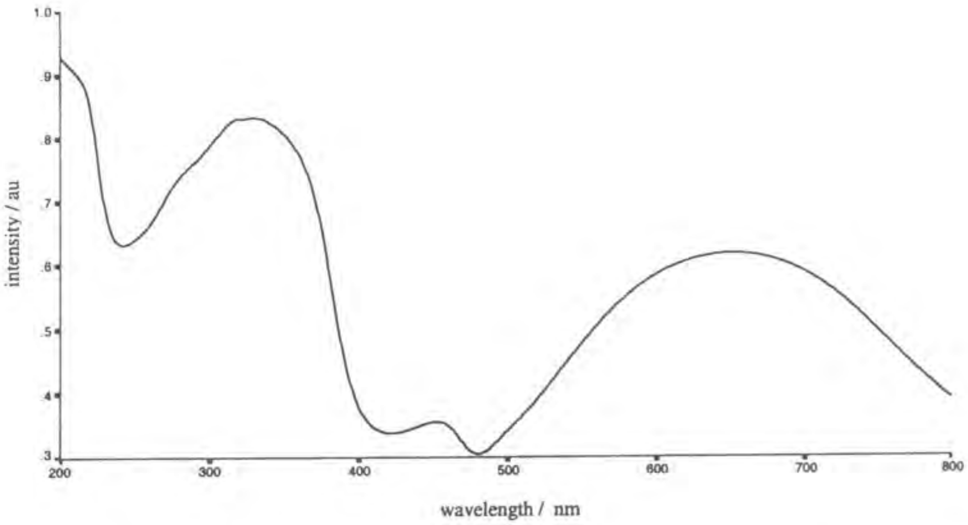

Figure 4.3: UV/VIS-spectrum of emeraldine base films on quartz substrates

around 650 nm and is ascribed to a transition of the iminoquinoid moiety. This has been postulated to be due to the formation of self-trapped excitons at iminoqinoid sites. This self-trapping mechanism is interesting because it is thought of as being formed by rotation of the benzene rings with respect to their neighbours. This extra degree of freedom along the polymer chain is introduced by the heteronuclear coupling between adjacent rings in the polyaniline backbone. The small peak at 450 nm and the shoulder at 290 nm is due to partial protonation as reported previously[Mon92]

4.4 Solution-State NMR

As a basis for further studies solution-state spectra have been measured. ^{1}H and ^{13}C spectra of leucoemeraldine and emeraldine base are similar to spectra found in the literature. Kenwright et al.[KFP$^+$92, KFP$^+$93] performed solution-state NMR studies on polyaniline (EB, and LEB) and could partially assign the carbon spectra. Furthermore, by comparing ^{13}C spectra of differently prepared EB, they proved that neither chain scissions nor crosslinking occurs during the reaction from EB to LEB and back.

Figures 4.4 and 4.5 show the solution-state carbon and proton spectra of emeraldine base prepared as described in section 4.2.1. The peak at 7.009 ppm can be ascribed to the ring protons of the aromatic rings. All the other peaks are due to the

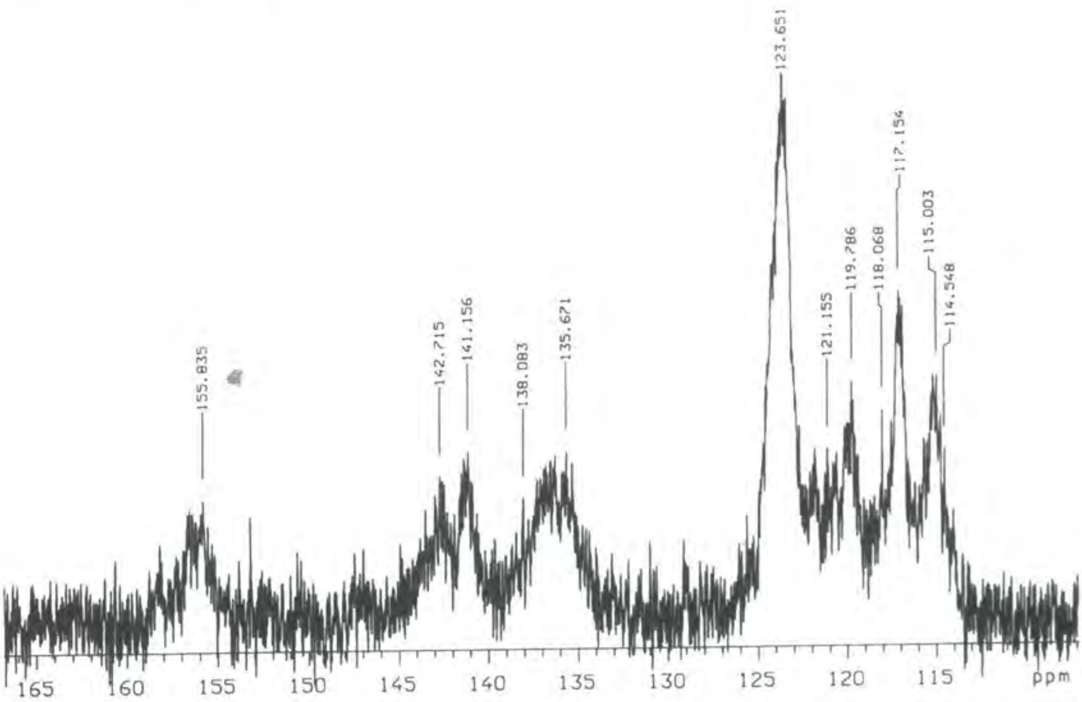

Figure 4.4: 100 MHz solution-state ^{13}C-spectrum of emeraldine base, solvent DMSO-d_6, spectral width 25kHz, 50000 transients, relaxation delay 1 s, ^{1}H-decoupled (WALTZ-16 modulated), pulse angle 58.1^o, line broadening 2 Hz, FT size 131072, referenced to TMS via acetone-d_6($\delta(^{13}C)$=29.8ppm).

solvent, NMP. Table 4.1 presents the ^{13}C chemical shift assignments of Kenwright et al.[KFP+92] on the basis of ^{13}C and ^{13}C-DEPT-90 spectra. The low signal-to-noise ratio in Figure 4.4 stems from a very low concentration of the substance (0.5% by mass as opposed to 10% used by Kenwright and others[KFP+92]). The assignments made are in agreement with the solid-state experiments of Kaplan et al.[KCRM88] based on CP and cross depolarisation spectra.

chemical shift / ppm	155	147	143	137	124	121	116
carbon label	b	c	f	a+g	a+e	d	h

Table 4.1: ^{13}C chemical shifts of emeraldine base assigned by Kenwright et el.[KFP+92], cf. labeling in Figure 4.1

Turning to the case of leucoemeraldine base the obvious difference is that far fewer peaks are present in the carbon spectrum. Figures 4.6 and 4.7 show the solution-state carbon and proton spectra of leucoemeraldine base prepared as described in section 4.2.2. The main features of the proton spectrum are again the peaks due to the solvent, NMP and DMSO-d_6. However, the two peaks at 7.529 ppm and

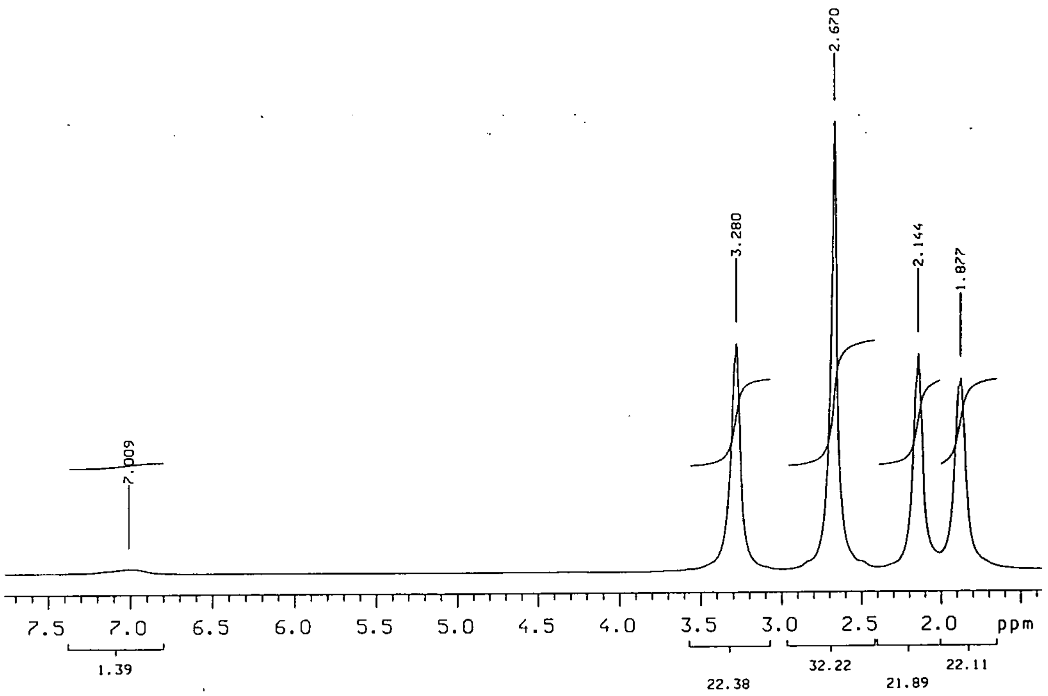

Figure 4.5: 400 MHz solution-state ^{1}H-spectrum of emeraldine base, solvent DMSO-d_6, spectral width 7 kHz, 32 transients, pulse angle 25.7^o, FT size 65536, line broadening 0.3 Hz, referenced to TMS via DMSO-d_6(δ(^{1}H)=2.49)

6.886 ppm are due to the NH group and the aromatic proton in LEB, respectively.

The two major peaks in the carbon spectrum at 137.6 ppm and 117.9 ppm can readily be assigned to the quaternary carbon and the tertiary carbon, respectively. This is in agreement with the proposed structure of LEB (see Figure 4.1).

It was assumed that the minor peaks around 137 ppm arise from imperfections in the polymer chain, such as incomplete reduction or polymerisation in the ortho or meta position rather than para. A prediction for chemical shifts of carbons has been made by using a chemical shift database[CDS]. Unfortunately, deviations of predicted chemical shifts are in the range of the observed chemical shift differences, which prohibits a detailed assignment.

Assuming that LEB as made has indeed the proposed structure, and that no chain scission etc. occurred during the oxidisation back to EB and that the carbon specta of EB and reoxidised LEB are essentially the same, it was concluded that EB has the proposed structure as well. Furthermore, Kaplan et al.[KCRM88] established that in fact imine and amine sites alternate in the polymer chain.

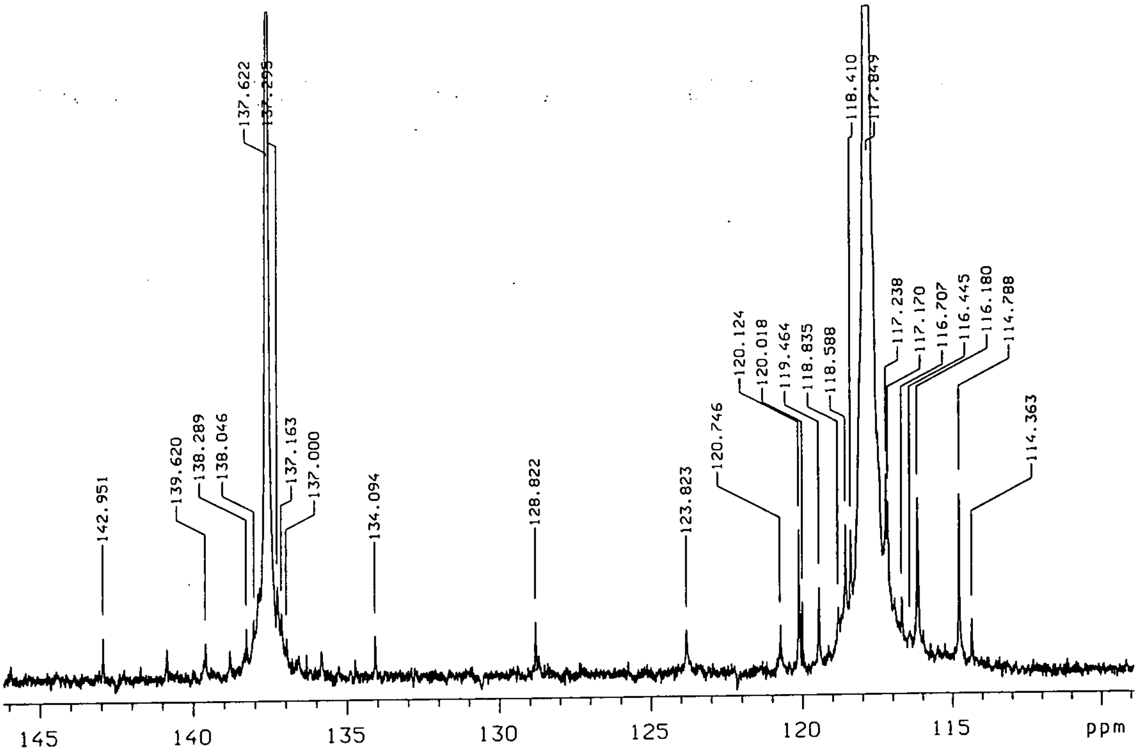

Figure 4.6: 100 MHz solution-state ^{13}C-spectrum of leucoemeraldine base, solvent DMSO-d_6, spectral width 25kHz, 50000 transients, relaxation delay 1 s, ^{1}H-decoupled (WALTZ-16 modulated), pulse angle 58.1^o, line broadening 0.8 Hz, FT size 131072, referenced to TMS via acetone-d_6

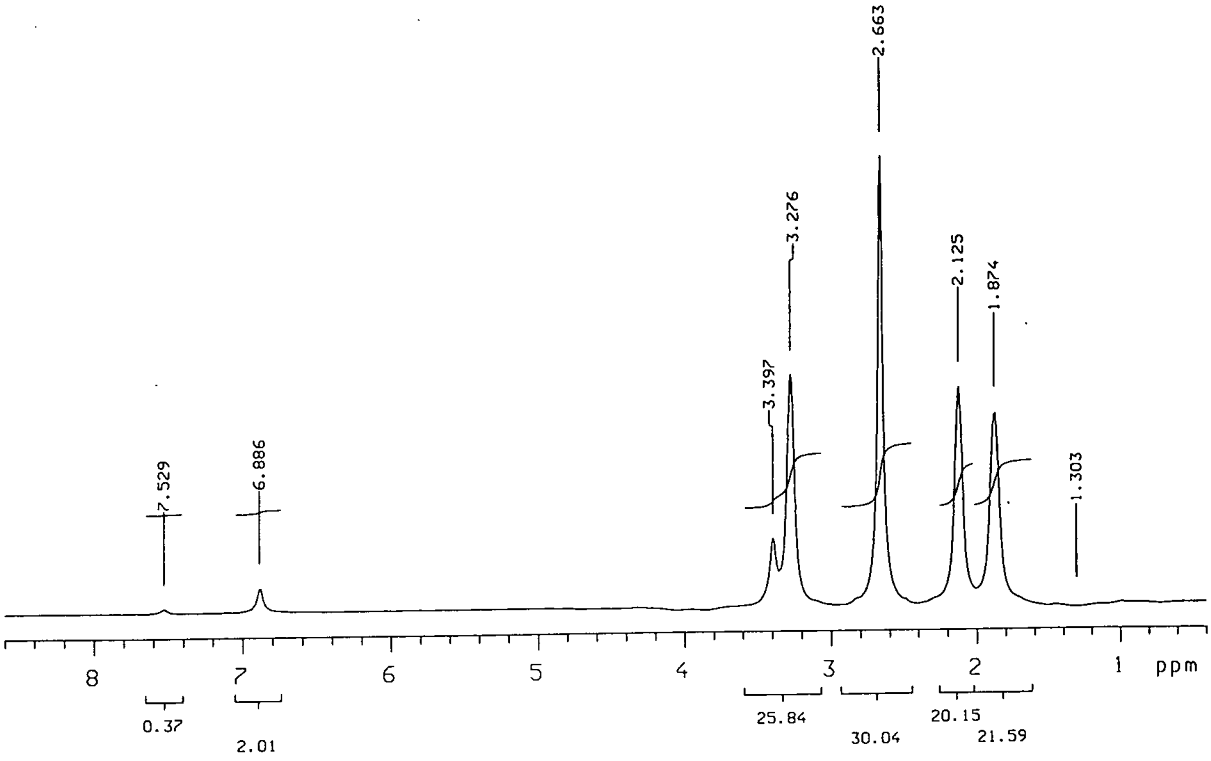

Figure 4.7: 400 MHz solution-state ^{1}H-spectrum of leucoemeraldine base, solvent DMSO-d_6, spectral width 7 kHz, 32 transients, pulse angle 25.7^o, FT size 65536, line broadening 0.3 Hz, referenced to TMS via DMSO-d_6

4.5 Solid-State NMR

4.5.1 Proton Spectra of Leucoemeraldine Base

A powder of leucoemeraldine, which had been sealed in a glass tube to prevent it from oxidation, was investigated by using static proton wideline NMR experiments. An MSL 100 with a static single-channel ^{1}H-probe was used.

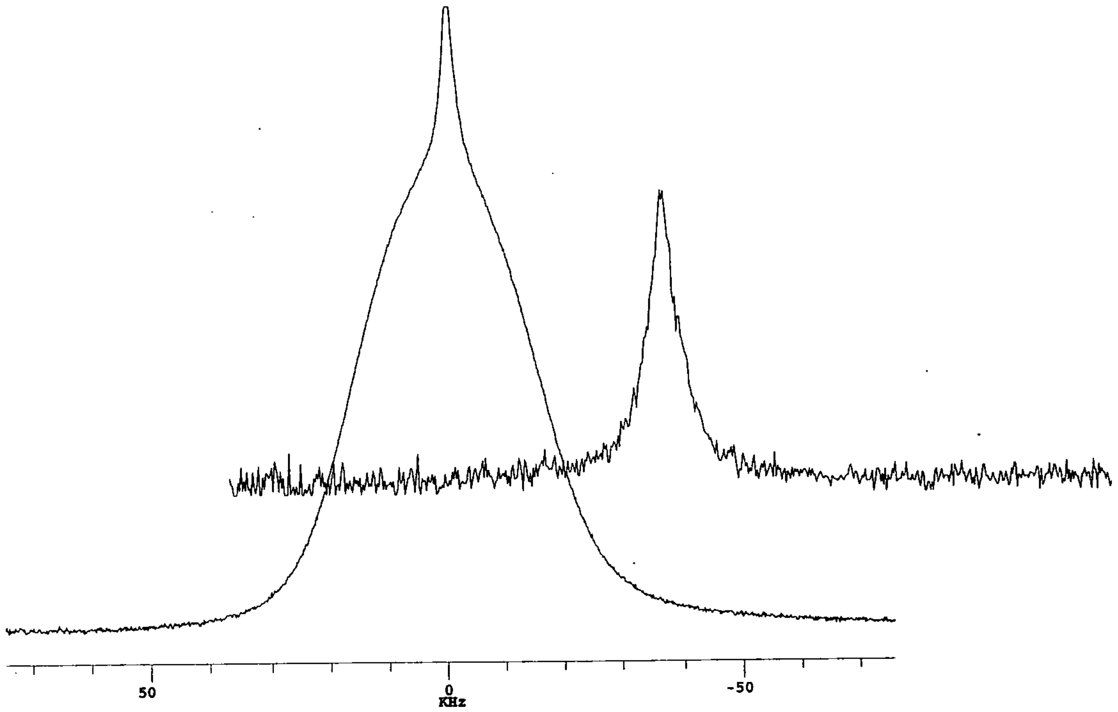

Figure 4.8: ^{1}H spectrum of leucoemeraldine base, static, comparison of single pulse (bottom) with solid echo (top) with τ=50 μs, six-fold vertical expansion, referenced to PDMSO 0 kHz

The spectrum of polyaniline in the leucoemeraldine form is shown in Figure 4.8. It consists of a broad Gaussian line and a rather narrow peak. If the on-resonance FID was looked at, a fast decaying signal causing a broad line and a more slowly decaying signal which gives rise to the comparatively narrow peak would be observed. After a 50 μs delay in the solid-echo experiment ($90^\circ_x - \tau - 90^\circ_y - \tau-$acq) only the narrow peak can be observed. Thus, the difference in T_2 gives us a tool to distinguish between the two sorts of nuclei, e.g. in a spin-diffusion experiment. The linewidth of the broad peak is 27 kHz, whereas the linewidth of the narrow peak as observed

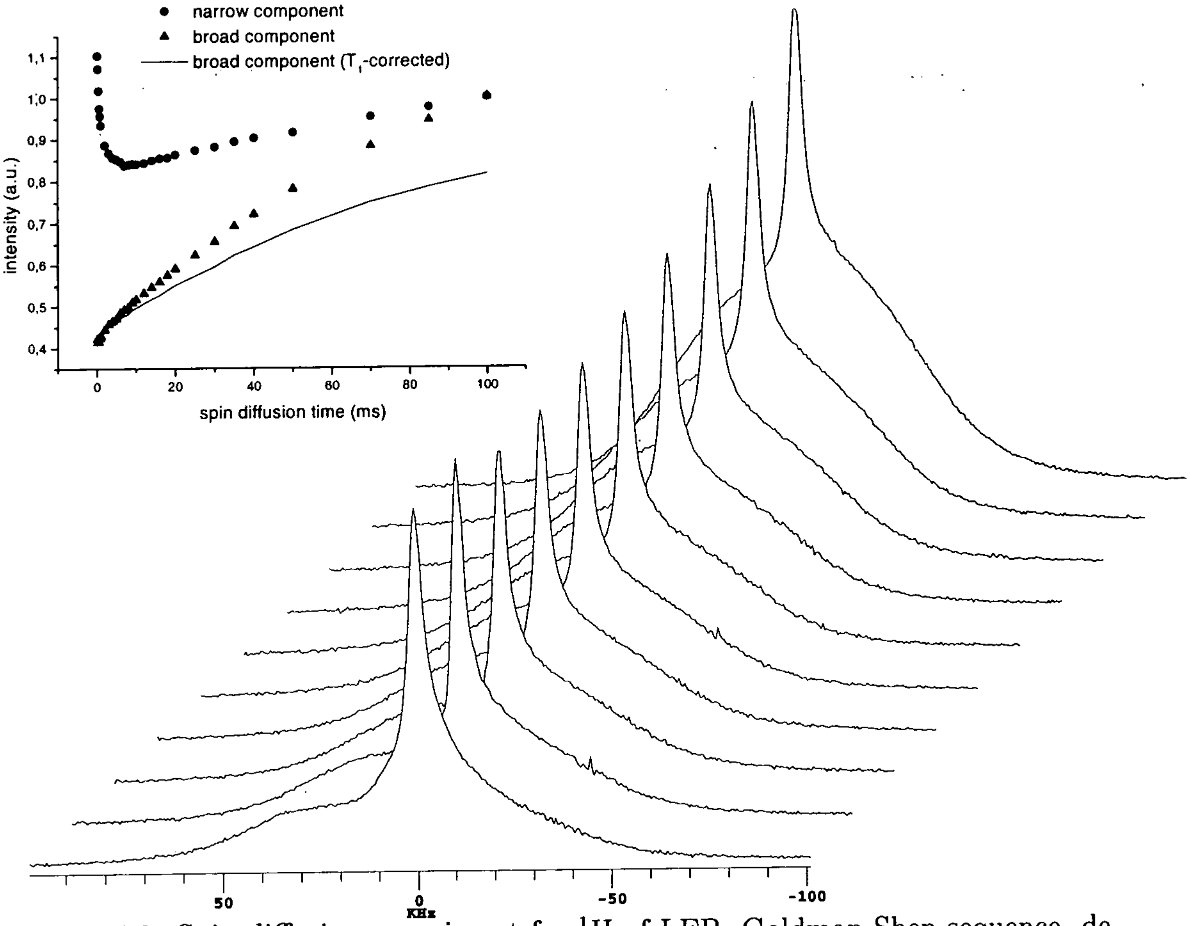

Figure 4.9: Spin-diffusion experiment for ^{1}H of LEB. Goldman-Shen sequence, description see text. first (selecting) echo time τ_1=50 μs; mixing times from front to back: τ_2=0.1, 0.6, 2, 5, 8, 12, 18, 30, 50, 100 ms; echo time for observation τ_3=5 μs; inset shows the deconvoluted intensities and the T_1-corrected build-up curve for the rigid component

with the echo delay is only approximately 5 kHz.

These two different linewidths suggest that there are two regions with different mobilities present. Heterogeneity in polymers can be caused by a number of reasons such as crystalline and amorphous domains above the glass transition or motional heterogeneity to mention just two. A spin-diffusion experiment is a technique to investigate such heterogeneities in a solid. The basic principle of Goldman-Shen experiments and modifications can be summarised as follows

1. Pulse the spin system into a predetermined non-equilibrium state by establishing magnetisation gradients among different domains.
2. Allow mixing to occur by means of spin diffusion between different spin systems.

3. Monitor the magnetisation of the domains and the effect of mixing, by a suitable detecting pulse sequence.

Thus, the sequence $\overbrace{90^\circ_x - \tau_1}^{1.} - \overbrace{90^\circ_{-x} - \tau_2}^{2.} - \overbrace{90^\circ_x - \tau_3 - 90^\circ_y - \tau_3 - \mathrm{acq}}^{3.}$, which is the above mentioned Goldman-Shen sequence with a solid-echo detection, was used. Figure 4.9 is a stack plot of spectra obtained by this method with a variable spin diffusion time τ_2. After 100 μs spin-diffusion time τ_2 mainly the narrow signal remains, whereas after τ_2 = 100 ms almost the whole signal (cf. Figure 4.8) has recovered.

On a closer look one may be surprised to see a rising intensity of the recorded spectrum instead of a constant total magnetisation (in accordance with energy conservation). The question, which arises, i.e. where does the magnetisation observed in the broad line come from, can be answered as follows: One source is, of course, spin diffusion from the domain which gives rise to the narrow 7 kHz line. The other must be magnetisation which is recovering during the mixing period τ_2, when magnetisation is aligned along the z-axis. Spin-lattice relaxation is responsible for the fact that the broad component rises faster and the narrow component does not decrease as fast as expected. If T_1 is of the order of the spin-diffsion time it is increasingly difficult to obtain reliable quantitative data, e.g. domain size or spin-diffusion constant. However, the curve with the longer T_1 can be corrected and shows the typical increase, as is caused by spin diffusion. This T_1-corrected build-up curve of the rigid component of LEB is shown in Figure 4.9.

Figure 4.10 shows a stack plot of T_1-experiments. Obviously there are different T_1 constants for the broad and narrow peak. The T_1-experiment for short inversion times τ (2,...,10 ms, see inset in Figure 4.10) shows a nulling of the narrow signal at 5 ms, whereas the broad signal exhibits a null time of τ=300 ms. This huge difference in T_1 promises to be a good means of selection for further studies (e.g. ^{1}H→ ^{13}C CP) even better than selection by different T_2. The spin-lattice relaxation parameters can be calculated from a fit to deconvoluted spectral intensities which is more exact than just using one data point, namely the null time. The fit gives the two values: 12 ms for the narrow, and 490 ms for the broad component.

The inversion-recovery experiment at high temperature (Figure 4.11) reveals that only a small 'T_1-heterogeneity' can be detected. It is found, after deconvoluting the

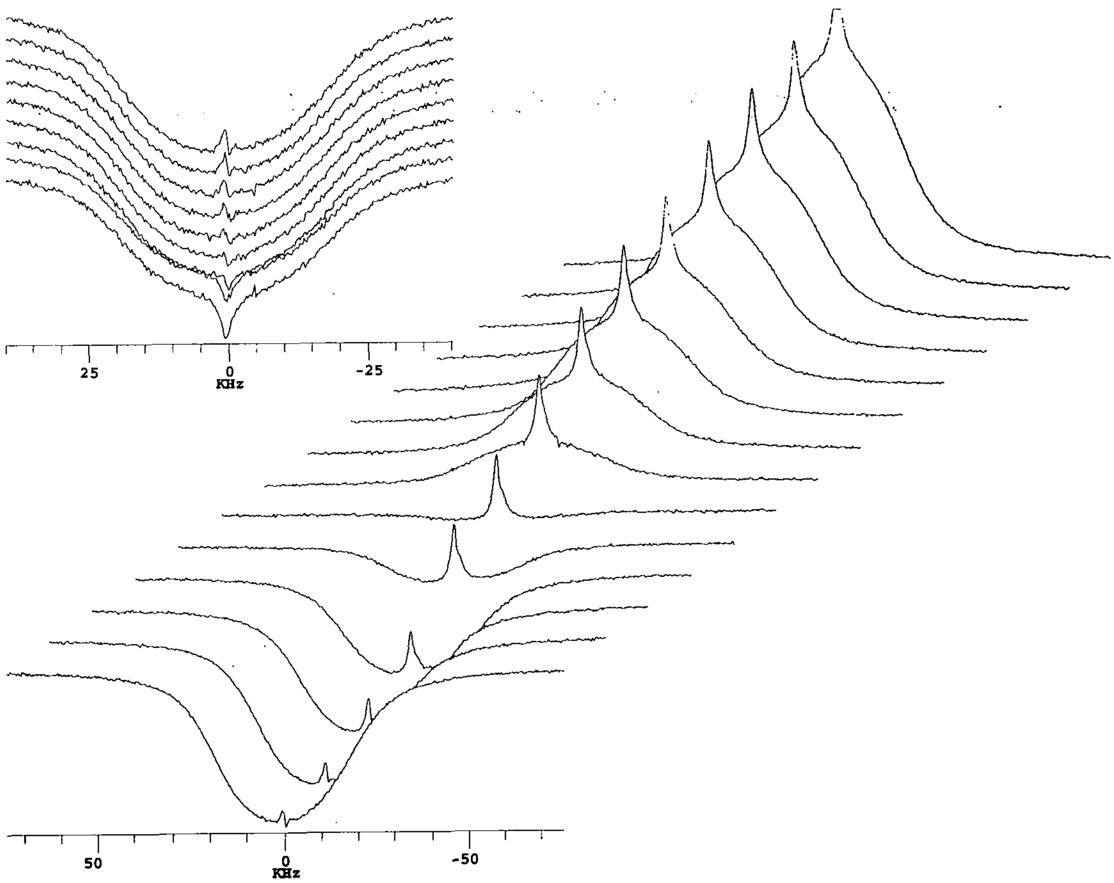

Figure 4.10: Inversion-recovery ^{1}H spectra of leucoemeraldine base at ambient temperature; Inversion time from front to back 10, 20, 50, 100, 200, 300, 500, 700, 900, 1100, 1400, 1700, 2000, 3000 ms; Inset shows the region of short recovery delays in greater detail: τ=2, 3, 4, 5, 6, 7, 8, 9, 10 ms

spectra with two gaussian peaks of different widths, that T_1's are much closer: 230 ms for the narrow, and 300 ms for the broad component.

A dependence of T_1 on correlation time with only one minimum can be assumed as a first approximation. Further, we could presume that the correlation times for these different regions are at either side of this minimum (the broad peak to longer τ's, and the narrow peak at the side of the fast correlation limit). Upon heating the sample, correlation times for both sites generally decrease, which brings the T_1 values closer. One has to acknowledge that the relation of T_1 might be much more complicated. However, still it can be inferred that such an opposite T_1-dependence of temperature is possible. The fact that the two measured intrinsic values for spin-lattice relaxation have not been averaged suggests that the domains show very large phase dimension.

The temperature dependence in the range from 294 K up to 375 K of proton

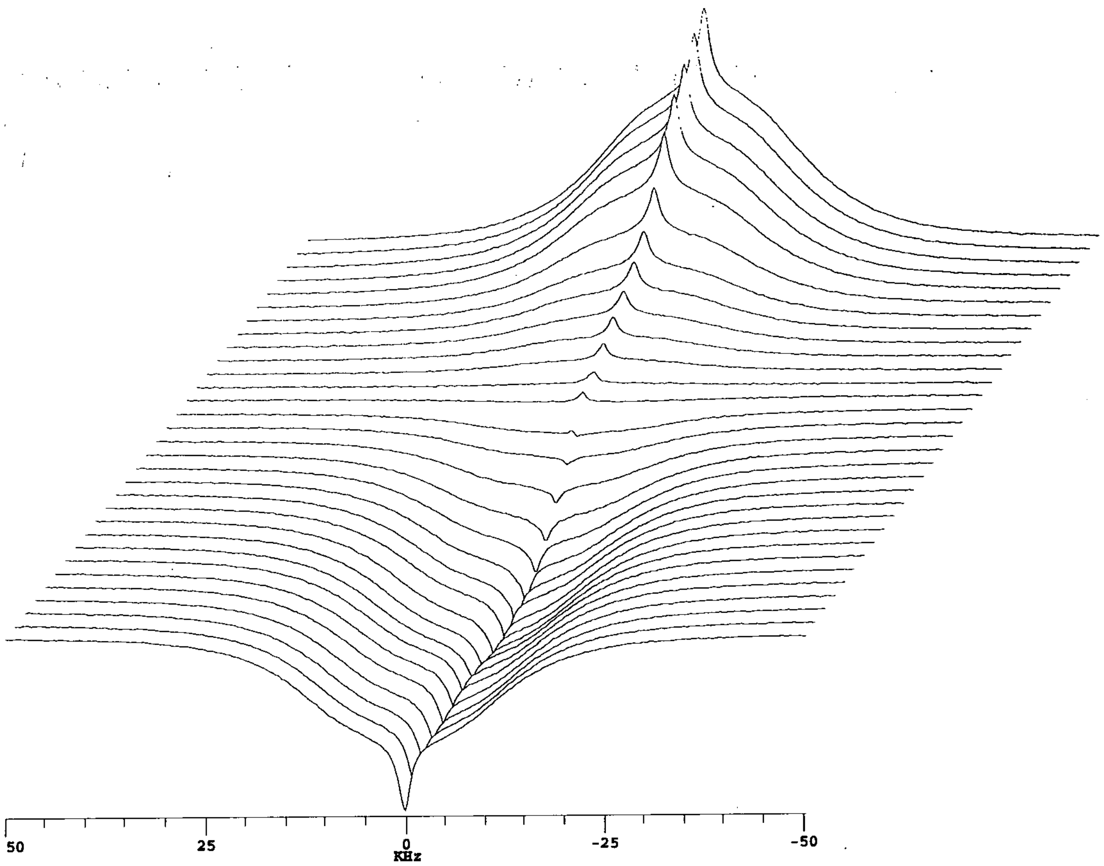

Figure 4.11: Inversion-recovery experiment of LEB as shown in Figure 4.10 but at high temperature T=375 K. τ=1, 2, 3, 4, 5, 6, 7, 8, 9, 10, 15, 20, 30, 50, 70, 100, 130, 160, 200, 250, 280, 310, 350, 400, 500, 700, 900, 1100, 1500, 3000 ms

broadline spectra for leucoemeraldine is displayed in Figure 4.12. The spectra have been recorded using a solid-echo pulse sequence with an echo time of 5 μs to overcome the effects of dead-time. Both the broad and the narrow signal seem to be narrowed at high temperatures. The inset shows the behaviour of only the narrow signal recorded with a 60 μs echo delay. Apparently, the signal intensity rises. The fact that we observe a stronger signal from sites with higher mobility must simply be caused by transformation of low-mobility domains into high-mobility domains activated by thermal motion. This weakens the argument of an impurity causing the mobile peak. (Although absorbed water, thermally activated, could cause the same behaviour.)

4.5.2 Proton Spectra of Emeraldine Base

The emphasis of the present work has been on measurements of leucoemeraldine. Although emeraldine is the conducting compound of the polyaniline family, LEB attracts considerable interest because it serves as a model compound due to its

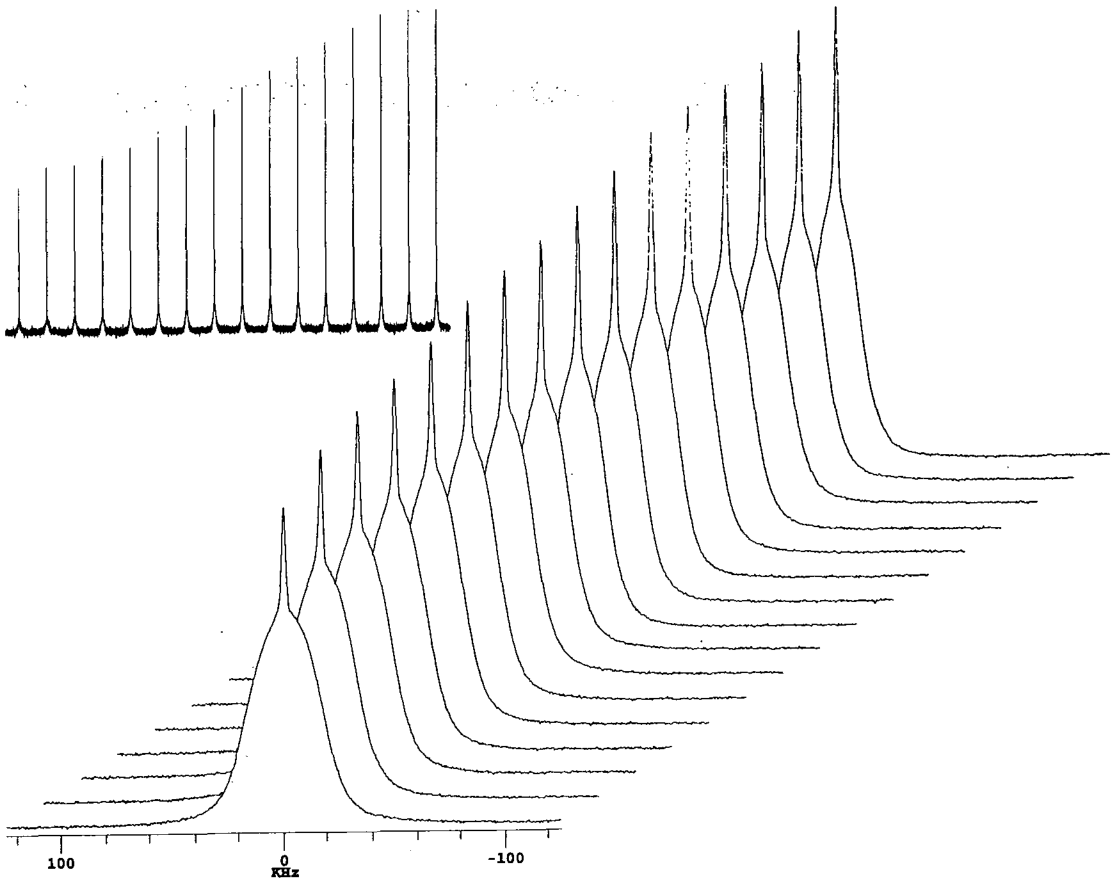

Figure 4.12: Variable temperature plot of ^{1}H solid echo for LEB, $\tau = 5$ μs. T=294, 305, 310, 315, 320, 325, 330, 335, 340, 345, 350, 355, 360, 365, 370, 375 K The inset shows the same temperature range but with a longer echo time $\tau = 60$ μs

simpler structure.

An interesting fact is that emeraldine base (the basis for production of leucoemeraldine by reduction with hydrazine) does not exhibit the pronounced behaviour of different T_1 values as leucoemeraldine does. Values of 125 ms and 150 ms were observed for the narrow and broad component respectively. When doing T_1-experiments one should bear in mind that under conditions of fast spin diffusion only an averaged T_1 is measured. Very small domains could not be detected by means of the T_1-experiment, which operates on a time scale comparable to spin diffusion times.

The chemical structure of emeraldine explains how motions of parts of the polymer are restricted: In leucoemeraldine a single phenyl-ring could rotate about its C2-axis. The double bonding between nitrogen and a quinoid ring in emeraldine base prohibits this relatively unhindered rotation (semi-rigid rod).

4.6 X-Ray Results

A good candidat for heterogeneous behaviour in polymers is partial crystallinity. The proton spectrum of polyethylene, for instance, shows features of a mobile and rigid component, which are attributed to amorphous and crystalline regions, respectively. Experiments have been performed in order to investigate this possibility for polyaniline.

Investigations on X-ray structures of PANi have been carried out by Epstein et al.[JEP+91, MPE+92]. Jozefowicz and others determined the unit cell structure of LEB[JEP+91]. Its space group is pseudoorthorhombic (P1), with parameters a=6.15 Å, b=4.3 Å, c=9.8 Å. The crystal structure is the same as that of emeraldine salt, prepared in conducting, doped, partially crystalline form. The coherence length has been estimated to be ≈50 Å.

Chacko et al.[CHGH98] showed too that LEB contains crystallites. They discovered an endotherm of LEB at 385...395°C and proved by results from X-ray, thermogravimetric analysis (TGA), differential scanning calorimetry (DSC) and light microscopy that this must be due to a melting transition of crystallites in LEB.

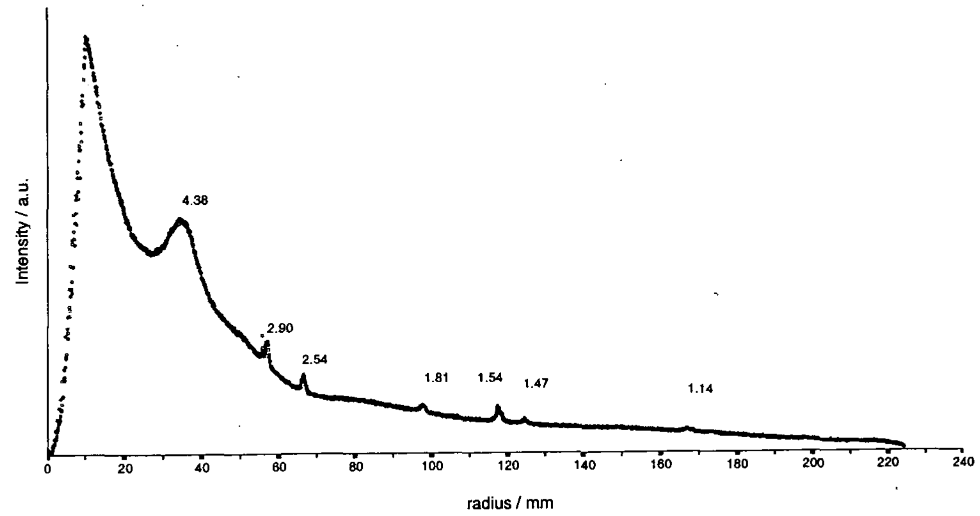

Figure 4.13: X-ray pattern of leucoemeraldine, numbers over peaks give calculated d-spacing

The heterogeneity observed and described in section 4.5.1 could at a first look be due to different relaxation behaviours in crystal and amorphous domains. A rough guess at the crystallinity from peak intensities of narrow and broad peak, however, leads to a ratio of mobile to rigid form of about 2...5%. This would imply a degree of crystallinity of over 90% which is highly unlikely.

Figure 4.13 presents the X-ray pattern of LEB measured on a rotating anode X-ray generator (details described in section 1.2). In order to estimate the crystallinity one would need to subtract the background signal. The remaining pattern should then contain only signals from amorphous and crystalline regions. The ratio of their corresponding areas would give a guess for the crystallinity. A background measurement was run, unfortunately, under different conditions so that this background subtraction could not be done. However, it became apparent that all sharp peaks, which are also to be seen in the LEB pattern, are due to reflections from the sample holder etc. Only the broad peak at low angles (d-spacing 4.38 Å) is from the actual sample. From its low intensity we can infer that the crystallinity is not higher than 90 %. Crystallinyties of polymers higher than 50 % as reported appear to be questionable. It is possible that local order in amorphous domains leads to such a high estimate of crystallinity as has been reported by Laridjani et al.[MPE$^+$92]. The ratio of intensity of mobile and rigid component observed with NMR indicates a proportion of less than 10 % of the mobile component. Thus it can be concluded that the difference of mobilities observed can not be explained by crystal and amorphous domains.

4.7 Light Excitation of Polyaniline-Films

4.7.1 Introduction and Basic Idea

As described in section 4.3, emeraldine base absorbs a broad band in the region of red light (ca. 600 nm) by means of a self-trapped excitonic polaron at the iminoquinoid site. Duke et al.[DCP86] interpreted this absorption band as being associated with the three-phenyl-ring exciton coupled to an approximately 90^o rotation of the quinoid moiety on which the excited electron resides, on the grounds of theoretical calculations. The experiments dealt with in this chapter are the first attempt to detect this rotation by means of NMR.

It was decided to perform proton wideline NMR on films of PANi. Static experiments have the advantage of easier excitation of the sample. Although it is already possible to irradiate spinning samples inside an MAS rotor, a lot of additional complications arise. As has been shown in section 4.5.1 and 4.5.2, the proton spectra of EB and LEB consists of a broad and narrow line. The line-broadening in ^1H spectra arises mainly from dipole-dipole interactions. This interaction can be averaged by (isotropic) motion, as is the case in liquids with linewidths down to a few Hz. If light-excitation induces motion in the polymer, this would contribute to motional averaging of homonuclear proton dipolar couplings, which should be detectable by narrowed lines or an increase of the ratio of narrow to broad signal-intensity.

A problem of measuring light-excited samples is the strong absorption of light by the surface of the samples. That is why (thin) films instead of powder have to be used in order to completely excite all regions within the sample. The absorption of the films used was estimated to be around 1.0 in the respective region of the electromagnetic spectrum (blue/red), which means that the whole sample was irradiated with light.

4.7.2 Experimental

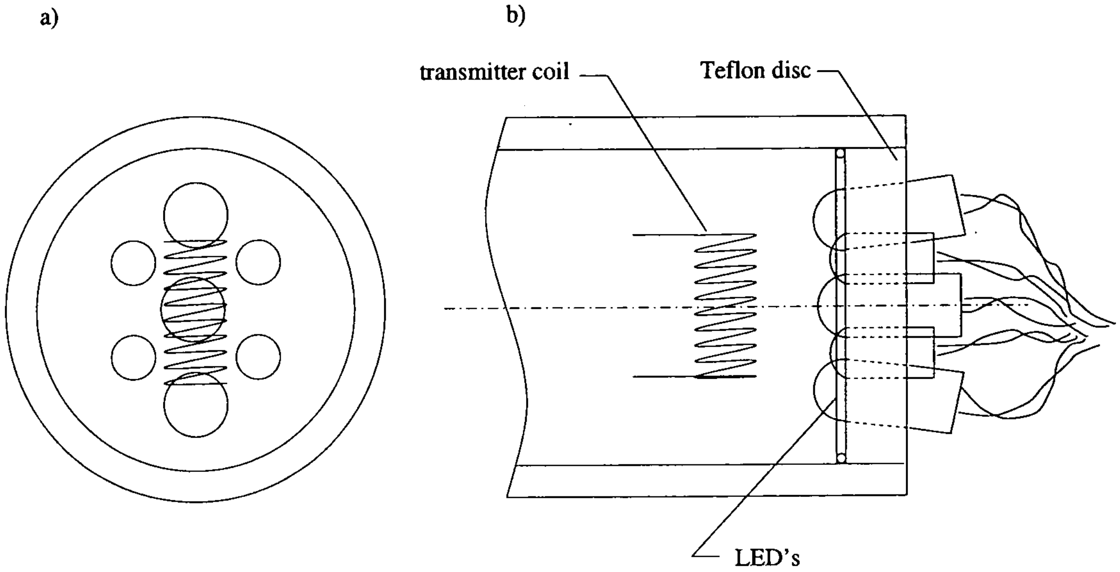

Figure 4.14: Sketch of the H-probe for the MSL 100 spectrometer, a) top-down and b) side-on view

The experimental setup is sketched in Figure 4.14. The sample, either a free-standing film or a film on a substrate, is mounted inside the transmitter coil (diameter ca. 5 mm). A disc of teflon functions as a holder for the seven light-emitting diodes of blue or red colour. This disc is mounted in the position where normally a ceramic disc is placed to allow the hot or cool gas to flow around the sample for variable temperature experiments. The wiring for the LED's is fed from above the cryomagnet. The light-emitting device (teflon disc, LED's, wiring) strongly influences the B_0 homogeneity and has to be compensated for by shimming. Spectra of the emeraldine base were recorded with blue or red light on, with and without the light-emitting device in the probe, and without a sample in the probe. A ^{1}H spectrum was recorded by acquiring 10000 transients each of 512 points with a pulse delay of 2 s.

4.7.3 Results and Discussion

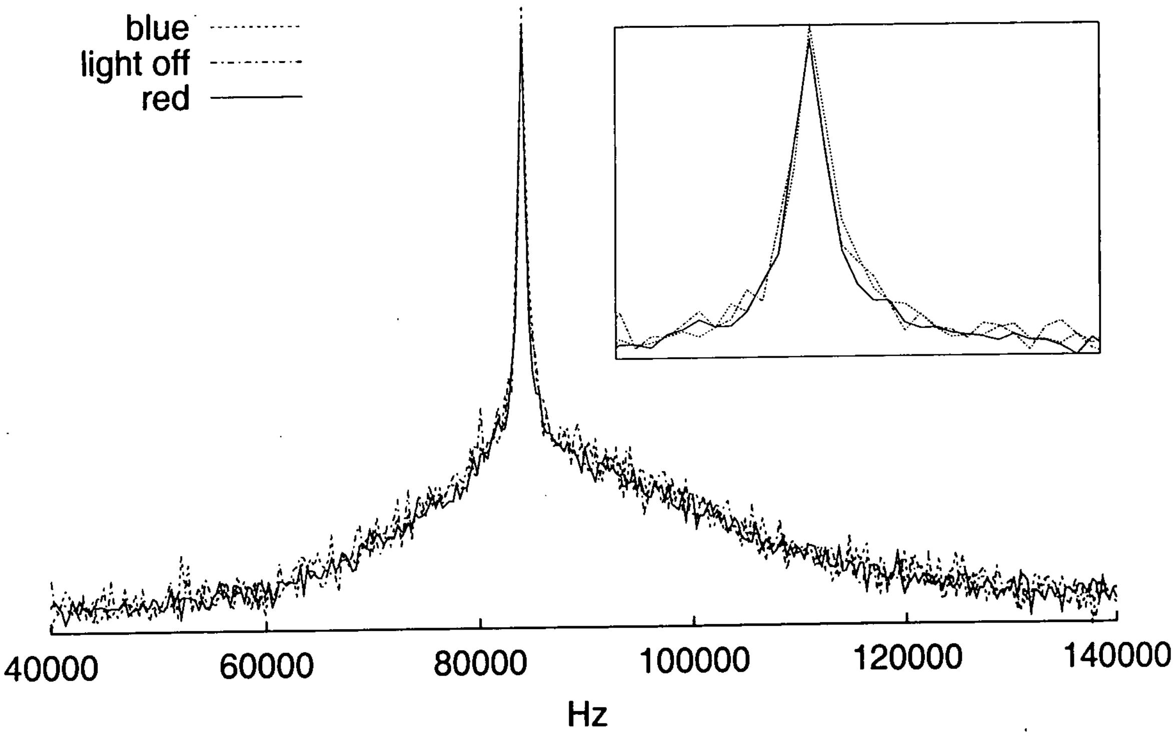

Figure 4.15: 100 MHz ^{1}H spectra of emeraldine base film irradiated with blue and red light, and with no excitation, 10000 transients, recycle delay 2 s

The three ^{1}H spectra of EB exhibit only small differences, as shown in Figure 4.15. In order to determine the effect of light excitation on linewidth a more reliable means to measure linewidth had to be devised. A lorentzian peak of the form

$$I(f) = \frac{a}{1 + (f - f_0)^2 * T_2^2} \tag{4.1}$$

was fitted to the narrow peak, where a is the arbitrary amplitude, f_0 the centre frequency, and T_2 the inverse of the linewidth at half peak height. The Levenberg-

Marquardt method for nonlinear regression was used on data points within 3 kHz to high and low frequencies of the main peak. A DC-offset correction was performed prior to fitting. The following table[2] reveals the results of the fit.

	light off	blue light on	red light on
linewidth at half height	2930 ± 170 Hz	2900 ± 140 Hz	2620 ± 80 Hz

No effect of irradiation at 400 nm(blue), in comparison to the spectrum without light excitation, is noted (both linewidths around 2.9kHz). However, excitation at 600 nm(red) leads to a small, but noticeable change in linewidth (ca. 2.6 kHz). This marginal effect confirms the expectation that irradiation at the red absorption band causes molecular motion.

Simple thermal excitation of the samples by the light irradiation could be ruled out by two precautions. Heat produced by the light sources was marginal because LED's were used. Furthermore, the samples was held in a constant stream of purge gas at ambient temperatures. The LED's were mounted over the sample allowing any heated air to escape.

4.8 Summary

In section 4.5.1 it has been shown that in leucoemeraldine there are two different regions present. They differ in their degree of mobility which results in different linewidths and different spin-lattice relaxation times, T_1. Throughout this work it has been tried to determine the source of this heterogeneity.

X-ray results presented in section 4.6 prove that the crystallinity of the polymer is not high enough in order to account for different mobilities.

Impurities in the LEB sample or in the bulk material EB, from which LEB was made, can be excluded on the grounds of solution-state NMR results. Other ways of contamination are water vapour absorbed by LEB or degeneration of the sample during sealing. The first is highly unlikely because the sample was dried for several hours under vacuum. The latter would imply that no spin diffusion from 'burned parts of the sample' to non-degraded parts of the sample could occur presuming that these domains are rather big and located very distant from each other. But

---

[2] Quoted deviations are standard errors derived from statistical calculations.

it has been demonstrated that spin diffusion appears (cf. Figure 4.9). Another reason against impurities is that the ratio of intensities obtained by deconvolution of proton spectra is higher at elevated temperatures. At ambient temperatures only 3 % mobile content is found in comparison with 7 % at 100 °C.

The latter findings suggest that the rigid component can be (reversibly) transformed to the mobile component. It may be that we have a heterogeneous local order in the amorphous phase of LEB. This local order has already been found in EB by Laridjani et al.[MPE+92]. They used a non-energy-dispersive X-ray diffraction technique. This local order might be heterogeneous throughout the amorphous region of the polymer and would then lead to the motional heterogeneity observed.

4.9 Further Work

At this stage of the light-excitation NMR experiments it seems to be imperative that spectral resolution and signal-to-noise ratio are improved. If films of a thickness of only 1 μm are used signal intensity will be naturally very low. This is in a region of sensitivity where the protons of water vapour start to measurably contribute to the signal. Apparently, just increasing the amount of sample does not solve the problem: A trade-off has to be made between higher signal-to-noise ratio (obtained by higher sample amount) and unwanted superposition of signals from excited and unexcited regions (due to the films being too thick).

With a view to the difficulties with the signal for proton NMR, carbon NMR of thin films seems to be out of reach at the moment, although, surely, useful information could still be gathered.

The increase in resolution could be obtained by spinning the sample at the magic angle. Light irradiation has been done under MAS with a different objective. A laser has been used to rapidly increase the temperature in a glass-sealed sample[EFMW95a, EFMW95b, EFMW96]. With lower laser intensity a sufficient excitation could be obtained. Problems arise from the usual sample handling under MAS (e.g. sealing in quartz glass, small sample amounts, the need to position the film under a small angle to the laser beam in order to fully irradiate its surface).

Another interesting experiment would be to measure the lifetime of these excitations, if the problems described so far could be circumvented. Up to now only continuous light has been used. The basic idea is to acquire the FID delayed after the light is switched off. The triggering of excitation is especially straightforward to implement when LED's are used as light sources since they are much easier to switch. Experiments with similar techniques involved have already been used to investigate fast switching processes in liquid crystals, liquid crystalline polymers and polymeric electrets[HRWK98]. Holstein et al. successfully applied synchronised electric pulses to orient their samples. This could be readily applied to light excitation.

By measuring the effect of a variable delay between the end of excitation and the beginning of acquisition, a lifetime of the excited state could be estimated. From other experiments this lifetime is known to be in the region of ms at ambient temperature. At lower temperatures this must rise to hours.

Bibliography

[Abr61] A. Abragam. *Principles of Nuclear Magnetism.* Oxford University Press, first edition, 1961.

[AM97] P.N. Adams and A.P. Monkman. Characterization of high molecular weight polyaniline synthesized at -40 degrees c using a 0.25:1 mole ratio of persulfate oxidant to aniline. *Synthetic Metals*, 87(2):165–169, 1997.

[AM98] P.N. Adams and A.P. Monkman. personal communication, 1998.

[APA+97] L. Abell, S.J. Pomfret, P.N. Adams, A.C. Middleton, and A.P. Monkman. Studies of stretched predoped polyaniline films. *Synthetic Metals*, 84(1-3):803–804, 1997.

[CDS] Chemical Database Service at Central Laboratory of the Research Councils Daresbury Laboratory. SpecInfo version 3.1.6.

[CHGH98] A.P. Chacko, S.S. Hardaker, R.V. Gregory, and T.W. Hanks. Melting transition in the leucoemeraldine form of polyaniline. *Polymer*, 39(14):3289–3293, 1998.

[CK84] R.E. Cais and J.M. Kometani. Synthesis of pure head-to-tail poly(trifluoroethylenes) and their characterization by 470-mhz f-19 nmr. *Macromolecules*, 17(10):1932–1939, 1984.

[CTKF96] J.R. Cheeseman, G.W. Trucks, T.A. Keith, and M.J. Frisch. A comparison of models for calculating nuclear magnetic resonance shielding tensors. *Journal of Chemical Physics*, 104(14):5497–5509, 1996.

[DCP86] C.B. Duke, E.M. Conwell, and A. Paton. Localized molecular excitons in polyaniline. *Chemical Physics Letters*, 131(1-2):82–86, 1986.

[DTW75] D.E. Demco, J. Tegenfeldt, and J.S. Waugh. Dynamics of cross relaxation in nuclear magnetic double resonance. *Physical Review B*, 11(11):4133–4151, 1975.

[EFMW95a] H. Ernst, D. Freude, T. Mildner, and I. Wolf. Laser-supported high-temperature MAS NMR - a new method for time-resolved in-situ studies of reaction steps in heterogeneous catalysis. *Studies in Surface Science and Catalysis*, 94:413–, 1995.

[EFMW95b] H. Ernst, D. Freude, T. Mildner, and I. Wolf. Temperature switched 2d mas nmr - a new method for time- resolved studies on catalytic reactions on solid-surfaces. *Zeitschrift für Physikalische Chemie-International Journal of Research in Physical Chemistry & Chemical Physics*, 189(Pt2):221–228, 1995.

[EFMW96] H. Ernst, D. Freude, T. Mildner, and I. Wolf. Laser-supported high-temperature mas nmr for time-resolved in- situ studies of reaction steps in heterogeneous catalysis. *Solid State Nuclear Magnetic Resonance*, 6(2):147–156, 1996.

[GFT+95] Revision E.2 Gaussian 94, M. J. Frisch, G. W. Trucks, H. B. Schlegel, P. M. W. Gill, B. G. Johnson, M. A. Robb, J. R. Cheeseman, T. Keith, G. A. Petersson, J. A. Montgomery, K. Raghavachari, M. A. Al-Laham, V. G. Zakrzewski, J. V. Ortiz, J. B. Foresman, J. Cioslowski, B. B. Stefanov, A. Nanayakkara, M. Challacombe, C. Y. Peng, P. Y. Ayala, W. Chen, M. W. Wong, J. L. Andres, E. S. Replogle, R. Gomperts, R. L. Martin, D. J. Fox, J. S. Binkley, D. J. Defrees, J. Baker, J. P. Stewart, M. Head-Gordon, C. Gonzalez, J. A. Pople, Gaussian, and Pittsburgh PA Inc. Gaussian 94, Revision E.2, 1995.

[GW83] U. Gaur and B. Wunderlich. *Journal of physical chemical reference data*, 12:29, 1983.

[HC68] D.K. Hindermann and C.D. Cornwell. *Journal of Chemical Physics*, 48:4148, 1968.

[HH62] S.R. Hartmann and E.L. Hahn. Nuclear double resonance in the rotating frame. *Physical Review*, 128(5):2042–2053, 1962.

[HH94] J. Hirschinger and M. Herve. Cross-polarization dynamics and spin-diffusion in some aromatic compounds. *Solid State Nuclear Magnetic Resonance*, 3(3):121–135, 1994.

[HHS97] P. Holstein, R. K. Harris, and B. J. Say. Solid-state ^{19}F NMR investigation of poly(vinylidene fluoride) with high-power proton decoupling. *Solid State Nuclear Magnetic Resonance*, 8:201–206, 1997.

[HM97] P. Holstein and G. A. Monti. personal communication, 1997.

[HRWK98] P. Holstein, J. Rauchfuss, M. Winkler, and G. Klotzsche. Study of fast switching processes due to electric and magnetic fields - an nmr approach. *Solid State Nuclear Magnetic Resonance*, 10(4):225–233, 1998.

[HSH97] P. Holstein, U. Scheler, and R.K. Harris. triple-channel solid-state nmr investigation of poly(vinylidene fluoride) polymorphs. *Magnetic Resonance in Chemistry*, 35(9):647–649, 1997.

[Hug98] E. Hughes. personal communication, 1998.

[JEP+91] M.E. Jozefowicz, A.J. Epstein, J.P. Pouget, J.G. Masters, A. Ray, Y. Sun, X. Tang, and A.G. Macdiarmid. X-ray structure of polyanilines. *Synthetic Metals*, 41(1-2):723–726, 1991.

[KCRM88] S. Kaplan, E.M. Conwell, A.F. Richter, and A.G. Macdiarmid. Solid-state c-13 nmr characterization of polyanilines. *Journal of the American Chemical Society*, 110(23):7647–7651, 1988.

[KFP+92] A.M. Kenwright, W.J. Feast, P.Adams, A.J.Milton, A.P.Monkman, and B.J.Say. Solution-state carbon-13 nuclear magnetic resonance studies of polyaniline. *Polymer*, 33(20):4192–4298, 1992.

[KFP+93] A.M. Kenwright, W.J. Feast, P.Adams, A.J.Milton, A.P.Monkman, and B.J.Say. Solution-state nmr studies of polyaniline. *Synthetic Metals*, 55-57:666–671, 1993.

[KPS86] A.M. Kenwright, K.J. Packer, and B.J. Say. Numerical simulations of the effects of spin-diffusion on nmr spin- lattice relaxation in semicrystalline polymers. *Journal of Magnetic Resonance*, 69(3):426–439, 1986.

[LC84] A.J. Lovinger and R.E. Cais. Structure and morphology of poly(trifluoroethylene). *Macromolecules*, 17(10):1939–1945, 1984.

[LSE86] M.H. Levitt, D. Suter, and R.R. Ernst. Spin dynamics and thermodynamics in solid-state nmr cross polarization. *Journal of Chemical Physics*, 84(8):4243–4255, 1986.

[MBTN97] P.Y. Mabboux, B. Beau, J.P. Travers, and Y.F. Nicolau. Non-exponential nmr relaxation in heterogeneously doped conducting polymers. *SYNTHETIC METALS*, 84(1-3):985–986, 1997.

[MDF82] V.J. Mcbrierty, D.C. Douglass, and T. Furukawa. Magnetic-resonance and relaxation in a vinylidene fluoride trifluoroethylene co-polymer. *Macromolecules*, 15(4):1063–1067, 1982.

[Meh83] M. Mehring. *Principles of High Resolution NMR in Solids.* Springer-Verlag, second edition, 1983.

[Mel81] M.T. Melchior. Poster b-29, presented at the 22nd experimental nmr conference in asilomar. 1981.

[MKBE74] L. Müller, A. Kumar, T. Baumann, and Richard R. Ernst. Transient oscillations in nmr cross-polarisation experiments in solids. *Physical Review Letters*, 32(25):1402–1406, 1974.

[Mon92] A.P. Monkman. Electroactivity in polyaniline. *Molecular Crystals and Liquid Crystals*, 218:777–784, 1992.

[MPE+92] M.Laridjani, J.P. Pouget, E.M.Scherr, A.G. MacDiarmid, M.E.Jozefowicz, and A.J.Epstein. Amorphography - the relationship between amorphous and crystalline order. 1. the structural origin of memory effects in polyaniline. *Macromolecules*, 25:4106–4113, 1992.

[Nal91] H. S. Nalwa. Recent developments in ferroelectric polymers. *Journal of Macromolecular Science-Reviews in Macromolecular Chemistry and Physics*, C31(4):341–432, 1991.

[OK83] Y. Oka and N. Koizumi. Pyroelectricity in polytrifluoroethylene. *Japanese Journal of Applied Physics*, 22(5):L281–L283, May 1983.

[OK84] Y. Oka and N. Koizumi. Formation of pyroelectricity in unoriented polytrifluoroethylene. *Japanese Journal of Applied Physics*, 23(6):748–753, June 1984.

[OK85] Y. Oka and N. Koizumi. Pyroelectricity in oriented polytrifluoroethylene. *Japanese Journal of Applied Physics*, 24(6):669–673, June 1985.

[OK86] Y. Oka and N. Koizumi. Ferroelectric order and phase transition in polytrifluoroethylene. *Journal of Polymer Science: Part B: Polymer Physics*, 24:2059–2072, 1986.

[RHGG97] P. Reinheimer, J. Hirschinger, P. Gilard, and N. Goetz. Cross-polarization dynamics and proton dipolar local field measurements in some organic compounds. *Magnetic Resonance in Chemistry*, 35(11):757–764, 1997.

[RLG88] D.P. Raleigh, M.H. Levitt, and R.G. Griffin. Rotational resonance in solid-state nmr. *CHEMICAL PHYSICS LETTERS*, 146(1-2):71–76, 1988.

[Sli57] W.P. Slichter. Nuclear magnetic resonance in some fluorine derivatives of polyethylene. *Nuclear Magnetic Resonance*, 24:173–185, 1957.

[Sli78] C.P. Slichter. *Principles of Magnetic Resonance.* Springer-Verlag Berlin Heidelberg New York, second edition, 1978.

[SLME94] S.A. Smith, T.O. Levante, B.H. Meier, and R.R. Ernst. Computer-simulations in magnetic-resonance - an object-oriented programming approach. *Journal of Magnetic Resonance Series A*, 106(1):75–105, 1994.

[SM94] E.O. Stejskal and J.D. Memory. *High Resolution NMR in the Solid State.* Oxford University Press, first edition, 1994.

[SRS94] K. Schmidt-Rphr and H.W. Spiess. *Multidimensional Solid-State NMR and Polymers.* Academic Press, first edition, 1994.

[Sut] C. D. Sutherland. Realignment of an imaging plate system for high pressure x-ray diffraction studies, 4th year project, Appendix II. Master's thesis, University of Durham, Dept. of Physics.

[TSC82] A.E. Tonelli, F.C. Schilling, and R.E. Cais. F-19 nmr chemical-shifts and the microstructure of fluoro polymers. *Macromolecules*, 15(3):849–853, 1982.

[TTK+84] K. Tashiro, K. Takano, M. Kobayashi, Y. Chatani, and H. Tadokoro. Structural study on ferroelectric phase-transition of vinylidene fluoride-trifluoroethylene copolymers(iii) dependence of transitional behavior on vdf molar content. *Ferroelectrics*, 57(1-4):297–326, 1984.

Appendix A

Systems of Coupled Differential Equations

A.1 Two Spin Baths

The solution to an ordinary differential equation (ODE) of the type

$$\dot{y}(t) = ay(t) \tag{A.1}$$

is given by

$$y(t) = Ce^{at} \, ,$$

where C has to be defined by boundary conditions. If we have a system of (two) coupled differential equations as in chapter 3 our aim is to 'decouple' these equations. This is done by finding (linear) transformation so that each of the formerly coupled equations becomes of the type A.1. Everyone of these equations can be solved separately in the above-stated fashion. The inverse transformation yields the initially sought solutions.

It appears useful to use a matrix representation of the system. We start with the system given in equation 3.2 and 3.3.

$$\frac{d\beta_F}{dt}(t) = -\frac{\beta_F}{T_{1\rho}^F} - \frac{\beta_F - \beta_H}{T_{HF}} \tag{A.2}$$

$$\frac{d\beta_H}{dt}(t) = -\frac{\beta_H}{T_{1\rho}^H} - \epsilon\frac{\beta_H - \beta_F}{T_{HF}} \tag{A.3}$$

These equations can be rewritten such that $\frac{d\tilde{\beta}}{dt} = \mathbf{A} \cdot \tilde{\beta}$ with

$$\tilde{\beta} = \begin{pmatrix} \beta_H \\ \beta_F \end{pmatrix} \quad \text{and} \quad \mathbf{A} = \begin{pmatrix} -\frac{1}{T_{1\rho}^H} - \frac{\epsilon}{T_{HF}} & \frac{\epsilon}{T_{HF}} \\ \frac{1}{T_{HF}} & -\frac{1}{T_{1\rho}^F} - \frac{1}{T_{HF}} \end{pmatrix} = \begin{pmatrix} a & b \\ c & d \end{pmatrix}$$

Now we have to diagonalise the matrix of coefficients, $\mathbf{A}$. We find the eigenvalues by solving the quadratic characteristic polynomial of $\mathbf{A}$ and obtain two solutions $\lambda_\pm$:

$$\lambda_\pm = \frac{a+d}{2}(1 \pm \sqrt{1 - 4\frac{ad-bc}{(a+d)^2}}) = -\frac{1}{T_{HF}}a_\pm = -\frac{1}{T_{HF}}a_0\ (1 \pm \sqrt{1 - \frac{a_1}{a_0^2}}) \quad \text{with}$$

$$a_0 = \frac{1}{2}\ (\frac{T_{HF}}{T_{1\rho}^F} + \frac{T_{HF}}{T_{1\rho}^H} + 1 + \epsilon) \quad \text{and} \quad a_1 = \frac{T_{HF}^2}{T_{1\rho}^F T_{1\rho}^H} + (\frac{1}{T_{1\rho}^H} + \frac{\epsilon}{T_{1\rho}^F})T_{HF}$$

It is now merely a matter of solving the systems of linear equations given by the boundary conditions and their application to the derivatives of β_H and β_F with:

$$\begin{aligned} \beta_F(0) &= C_{F,1} + C_{F,2} = 0 \\ \beta_H(0) &= C_{H,1} + C_{H,2} = \beta_{H,0} \qquad \text{and} \\ \dot{\beta}_F(0) &= C_{F,1}\frac{-a_+}{T_{HF}} + C_{F,2}\frac{-a_-}{T_{HF}} = \frac{\beta_{H,0}}{T_{HF}} \\ \dot{\beta}_H(0) &= C_{H,1}\frac{-a_+}{T_{HF}} + C_{H,2}\frac{-a_-}{T_{HF}} = \beta_{H,0}(-\frac{1}{T_{1\rho}^H} - \frac{\epsilon}{T_{HF}}) \end{aligned}$$

This is straightforwardly solved (substituting a_+ for a_- and vice versa using $2a_0 = a_+ + a_-$):

$$C_{F,1} = -\frac{\beta_{H,0}}{a_+ - a_-} \qquad \text{and} \qquad C_{F,2} = \frac{\beta_{H,0}}{a_+ - a_-}$$

$$C_{H,1} = -\frac{\beta_{H,0}}{a_+ - a_-}(1 + \frac{T_{HF}}{T_{1\rho}^F} - a_+) \qquad \text{and} \qquad C_{H,2} = \frac{\beta_{H,0}}{a_+ - a_-}(1 + \frac{T_{HF}}{T_{1\rho}^F} - a_-)$$

And we arrive at

$$\beta_F(t) = \beta_{H,0}\frac{1}{a_+ - a_-}(\exp(-\frac{a_- t}{T_{HF}}) - \exp(-\frac{a_+ t}{T_{HF}})) \tag{A.4}$$

$$\begin{aligned} \beta_H(t) &= \beta_{H,0}\frac{1}{a_+ - a_-}\left((1 + \frac{T_{HF}}{T_{1\rho}^F} - a_-)\exp(-\frac{a_- t}{T_{HF}})\right. \\ &\qquad \left. -(1 + \frac{T_{HF}}{T_{1\rho}^F} - a_+)\exp(-\frac{a_+ t}{T_{HF}})\right) \end{aligned} \tag{A.5}$$

Suppose we have more general initial conditions, as in the case of homonuclear cross polarisation described in section 3.1.3. We then have the following boundary conditions:

$$\begin{aligned}
\beta_F(0) &= C_{F,1} + C_{F,2} = \beta_{F,0} \\
\beta_H(0) &= C_{H,1} + C_{H,2} = \beta_{H,0} \qquad \text{and} \\
\dot{\beta}_F(0) &= C_{F,1}\frac{-a_+}{T_{HF}} + C_{F,2}\frac{-a_-}{T_{HF}} = -\frac{\beta_{F,0}}{T_{1\rho}^F} - \frac{\beta_{F,0} - \beta_{H,0}}{T_{HF}} \\
\dot{\beta}_H(0) &= C_{H,1}\frac{-a_+}{T_{HF}} + C_{H,2}\frac{-a_-}{T_{HF}} = -\frac{\beta_{H,0}}{T_{1\rho}^H} - \epsilon\frac{\beta_{H,0} - \beta_{F,0}}{T_{HF}}
\end{aligned}$$

which can be solved as:

$$\begin{aligned}
C_{F,1} &= \frac{-T_{1\rho}^F\,\beta_{F,0}\,a_- + \beta_{F,0}\,T_{HF} + T_{1\rho}^F\,\beta_{F,0} - T_{1\rho}^F\,\beta_{H,0}}{T_{1\rho}^F\,(a_+ - a_-)} \\
C_{F,2} &= \frac{a_+\,T_{1\rho}^F\,\beta_{F,0} - \beta_{F,0}\,T_{HF} - T_{1\rho}^F\,\beta_{F,0} + T_{1\rho}^F\,\beta_{H,0}}{T_{1\rho}^F\,(a_+ - a_-)} \\
C_{H,1} &= \frac{-T_{1\rho}^H\,\beta_{H,0}\,a_- + \beta_{H,0}\,T_{HF} - \epsilon T_{1\rho}^H\,(\beta_{F,0} - \beta_{H,0})}{T_{1\rho}^H\,(a_+ - a_-)} \\
C_{H,2} &= \frac{a_+\,T_{1\rho}^H\,\beta_{H,0} - \beta_{H,0}\,T_{HF} + \epsilon T_{1\rho}^H\,(\beta_{F,0} - \beta_{H,0})}{T_{1\rho}^H\,(a_+ - a_-)}
\end{aligned}$$

In the case of homonuclear cross polarisation, indices F and H have to be replaced by the two types of fluorine, e.g. F,a and F,b

A.2 Three Spin Baths

If we have a situation of the type described in section 3.1.3, where we introduced three spin baths all in mutual contact with each other and the surrounding lattice, the matrix of coefficients, **A**, becomes:

$$\mathbf{A} = \begin{pmatrix}
-\frac{1}{T_{1\rho}^H} - \frac{\epsilon_{HF,a}}{T_{HF,a}} - \frac{\epsilon_{HF,b}}{T_{HF,b}} & \frac{\epsilon_{HF,a}}{T_{HF,a}} & \frac{\epsilon_{HF,b}}{T_{HF,b}} \\
\frac{1}{T_{HF,a}} & -\frac{1}{T_{1\rho}^{F,a}} - \frac{1}{T_{HF,a}} - \frac{\epsilon_{FF}}{T_{FF}} & \frac{\epsilon_{FF}}{T_{FF}} \\
\frac{1}{T_{HF,b}} & \frac{1}{T_{FF}} & -\frac{1}{T_{1\rho}^{F,b}} - \frac{1}{T_{HF,b}} - \frac{1}{T_{FF}}
\end{pmatrix}$$

The solution for this system of ODEs are sums of three exponentials, which could be found analytically, because it is in principle possible to solve the characteristic polynomial up to a degree of four.

$$\beta_k(t) = a_{1,k} \cdot e^{\lambda_1 t} + a_{2,k} \cdot e^{\lambda_2 t} + a_{3,k} \cdot e^{\lambda_3 t}$$

with $\lambda_i = f_i(T_{1\rho}^{H}, T_{1\rho}^{F,a}, T_{1\rho}^{F,b}, T_{HF,a}, T_{HF,b}, T_{FF}, \epsilon_{HF,a}, \epsilon_{HF,b})$ and
$a_{i,k} = g_{i,k}(T_{1\rho}^{H}, T_{1\rho}^{F,a}, T_{1\rho}^{F,b}, T_{HF,a}, T_{HF,b}, T_{FF}, \epsilon_{HF,a}, \epsilon_{HF,b}, \text{boundary conditions})$

Suppose we have found a transformation matrix $\mathbf{T}$ which diagonalises the matrix of coefficients $\mathbf{A}$:

$$\mathbf{D} = \mathbf{T}^{-1}\mathbf{A}\mathbf{T}$$

The columns of this matrix $\mathbf{T}$ are given by the eigenvectors $\mathbf{v_1} \ldots \mathbf{v_3}$:

$$\mathbf{T} = (\mathbf{v_1}\mathbf{v_2}\mathbf{v_3})$$

Similarly to the two-spin-bath case, we can write in the eigenvector basis:

$$\dot{\tilde{\beta}}(t) = \mathbf{D}\tilde{\beta}(t)$$

with the solution

$$\tilde{\beta}(t) = e^{\mathbf{D}t} \cdot \mathbf{c}$$

where $\mathbf{c}$ is a constant column vector with elements determined by the initial conditions. We know that any vector $\mathbf{r}$ is transformed from the eigenvector basis into the initial basis by:

$$\mathbf{r} = \mathbf{T}\tilde{\mathbf{r}}$$

For $t = 0$, the initial conditions for cross-polarisation dynamics are given, and we can write:

$$\beta(0) = \mathbf{T}\tilde{\beta}(0) = \mathbf{T}\mathbf{c}$$

Thus, we can calculate the value of the vector of constants by solving this system of linear equations: $\mathbf{c} = \mathbf{T}^{-1} \cdot \beta(0)$ The final solution is given by putting all these pieces together:

- The exponential functions with exponents determined from the eigenvalues $\lambda_1 \ldots \lambda_3$ of the matrix of coefficients $\mathbf{A}$
- The transformation matrix $\mathbf{T}$ given by the eigenvectors.
- The constants determined by the initial conditions from a system of linear equations.

$$\beta(t) = \mathbf{T}\exp(\mathbf{D}t) \cdot \mathbf{T}^{-1} \cdot \beta(0) = \exp(\mathbf{A}t) \cdot \beta(0)$$

Appendix B

Spin $\frac{1}{2}$ Operators in Matrix Form

In section 3.1.4 we decomposed the Hamiltonian for two spin $\frac{1}{2}$ particles in two submatrices for flip-flop terms and flop-flop terms. To work with these Hamiltonians we had to define spin operators operating on the respective subspace, denoted by $\chi = \Omega, \Delta$. It is quite instructive to have a look at the explicit matrix representation of these operators:

$$I_x^{\Delta} = I_x S_x + I_y S_y = \frac{1}{2}(I_+ S_- + I_- S_+) = \frac{1}{2}\begin{pmatrix} 0 & 0 & 0 & 0 \\ 0 & 0 & 1 & 0 \\ 0 & 1 & 0 & 0 \\ 0 & 0 & 0 & 0 \end{pmatrix}$$

$$I_y^{\Delta} = I_y S_x - I_x S_y = \frac{i}{2}(I_- S_+ - I_+ S_-) = \frac{1}{2}\begin{pmatrix} 0 & 0 & 0 & 0 \\ 0 & 0 & -i & 0 \\ 0 & i & 0 & 0 \\ 0 & 0 & 0 & 0 \end{pmatrix}$$

$$I_z^{\Delta} = \frac{1}{2}(I_z - S_z) = \frac{1}{2}\begin{pmatrix} 0 & 0 & 0 & 0 \\ 0 & 1 & 0 & 0 \\ 0 & 0 & -1 & 0 \\ 0 & 0 & 0 & 0 \end{pmatrix}$$

$$I_x^{\Omega} = I_x S_x - I_y S_y = \frac{1}{2}(I_+ S_+ + I_- S_-) = \frac{1}{2}\begin{pmatrix} 0 & 0 & 0 & 1 \\ 0 & 0 & 0 & 0 \\ 0 & 0 & 0 & 0 \\ 1 & 0 & 0 & 0 \end{pmatrix}$$

$$I_y^\Omega = I_y S_x + I_x S_y = \frac{i}{2}(I_- S_- - I_+ S_+) \quad = \frac{1}{2}\begin{pmatrix} 0 & 0 & 0 & -i \\ 0 & 0 & 0 & 0 \\ 0 & 0 & 0 & 0 \\ i & 0 & 0 & 0 \end{pmatrix}$$

$$I_z^\Omega = \frac{1}{2}(I_z + S_z) \quad = \frac{1}{2}\begin{pmatrix} 1 & 0 & 0 & 0 \\ 0 & 0 & 0 & 0 \\ 0 & 0 & 0 & 0 \\ 0 & 0 & 0 & -1 \end{pmatrix}$$

Appendix C

Simulated Annealing Fitting Routine

The programme for fitting the solutions of the system of three ordinary differential equations has been written in C++ using the library for computer simluations $\hat{\hat{\Gamma}}$ [SLME94]. This package can handle complex variables, vectors and matrices in a very convenient way.

Different annealing schedules have been tested. The linear schedule succeded by the method of the steepest gradient proved to be a suitable choice for the present cost function χ^2.

```
#include <gamma.h>
/* matrix of coefficients for system of ODE's */
matrix A(3,3),T(3,3),D(3,3),D_exp(3,3);
col_vector beta(3),c(3),amp(3),v_complex(3);
double factor = 100;
double end_temp=50000,start_prob=0.4;
double H_amp=2270,o_H_amp=H_amp,d_H_amp=H_amp/factor,
       H_scale=0.09,o_H_scale=H_scale,d_H_scale=H_scale/factor,
       old_chi=1e100,new_chi=1e100,d_amp=1,
       Temp=10;
int numrows1=0,numrows2=0;
// data structures
double t[200],t_h[200],h[200],x[200],y[200];
double T_1rH=0.0046,T_1rFa=0.0043,T_1rFb=0.0051,//spin-lattice rel.times
       T_HFa=0.00341,T_HFb=0.0021,T_FF=0.73,    // cross-relaxation par.
       eps_HFa=2.,eps_HFb=1.;                   // rel. heat capacities
double o_T_1rH=T_1rH,o_T_1rFa=T_1rFa,
       o_T_1rFb=T_1rFb, o_T_HFa=T_HFa,
       o_T_HFb=T_HFb,o_T_FF=T_FF;
double d_T_1rH=T_1rH/factor,d_T_1rFa=T_1rFa/factor,
       d_T_1rFb=T_1rFb/factor, d_T_HFa=T_HFa/factor,
       d_T_HFb=T_HFb/factor,d_T_FF=T_FF/factor;
/*theoretical fit function; calculation of matrix etc.*/
```

```
void calc_fit()
{ A(0,0)=-1/T_1rH-eps_HFa/T_HFa-eps_HFb/T_HFb;
  A(0,1)=eps_HFa/T_HFa;
  A(0,2)=eps_HFb/T_HFb;
  A(1,0)=1.0/T_HFa;
  A(1,1)=-1.0/T_1rFa-1/T_HFa-eps_HFb/eps_HFa/T_FF;
  A(1,2)=eps_HFb/eps_HFa/T_FF;
  A(2,0)=1.0/T_HFb;
  A(2,1)=1.0/T_FF;
  A(2,2)=-1.0/T_1rFb-1.0/T_HFb-1.0/T_FF;
 /* initial condition */
 beta(0)=H_amp;beta(1)=0;beta(2)=0;
 diag(A,D,T); //diagonalisation of a into D
 c=inv(T)*beta;
}
/*residual sum of squares*/
double chi_square()
{double chi=0;
 for(int i=0;i<numrows1;i++)
   { D_exp(0,0)=exp(D(0,0)*t[i]);
     D_exp(1,1)=exp(D(1,1)*t[i]);
     D_exp(2,2)=exp(D(2,2)*t[i]);
     D_exp.set_type(d_matrix_type);
     v_complex=T*D_exp*c;
     chi+=(Re(v_complex(1))-x[i])*(Re(v_complex(1))-x[i]);
     chi+=(Re(v_complex(2))-y[i])*(Re(v_complex(2))-y[i]);
   }
 for(int i=0;i<numrows2;i++)
   { D_exp(0,0)=exp(D(0,0)*t_h[i]);
     D_exp(1,1)=exp(D(1,1)*t_h[i]);
     D_exp(2,2)=exp(D(2,2)*t_h[i]);
     D_exp.set_type(d_matrix_type);
     v_complex=T*D_exp*c;
     chi+=(H_scale*Re(v_complex(0))-h[i])
         *(H_scale*Re(v_complex(0))-h[i]);
   }
 return(chi);
}
main (int argc,char* argv[])
{FILE *f_in1,*f_in2,*f_out1,*f_out2,*f_out3;
 String fname1,fname2,f_out_name1,f_out_name2;
 int which_par=1;

  /*initialisation*/
[...] //reading in of experimental data from files etc.
 int counter=0;
 /*loop of fit*/
 cout<<"start fit"<<endl;
 while (counter<100000)
```

```
   {if(counter%100==1){
       [...]  // write parameter and variables
              // for monitoring the fit routine
   }
     counter++;
     /*determine fit function*/
     calc_fit();
     old_chi=new_chi;new_chi=chi_square();
// the parameters which are fixed have to be commented out
// at places marked with (**)
     if((new_chi>old_chi) &&
        ((double)rand()/RAND_MAX>start_prob*(1-1.0/end_temp*counter))
       )
       {//reject alterations
        //(**)
         switch(which_par)
           {case 0: H_amp=o_H_amp; break;
            case 1: H_scale=o_H_scale;break;
    [...] // other variables analogously modified
            case 7: T_FF=o_T_FF;break;
           }
         new_chi=old_chi;
       }
     else
       {//accept alteration
        //(**)
       switch(which_par)
         {case 0: o_H_amp=H_amp; break;
          case 1: o_H_scale=H_scale;break;
    [...] // other variables analogously modified
          case 7: o_T_FF=T_FF;break;
         }
       }
     /* alter parameters */
     which_par++;
     which_par=which_par%8;
     //(**)
     switch(which_par) {
     case 0: o_H_amp=H_amp;
             H_amp+=d_H_amp*(.5-(double)rand()/RAND_MAX);
             break;
     case 1: o_H_scale=H_scale;
             H_scale+=d_H_scale*(.5-(double)rand()/RAND_MAX);
             break;//scaling of proton channel
    [...] // other variables analogously modified
     case 7: o_T_FF=T_FF;
             T_FF+=d_T_FF*(.5-(double)rand()/RAND_MAX);
             break;//T_FF
     }
```

```
    }
 for(int i=0;i<numrows1;i++)
   {// output experimental and fitted curves
    D_exp(0,0)=exp(D(0,0)*t[i]);
    D_exp(1,1)=exp(D(1,1)*t[i]);
    D_exp(2,2)=exp(D(2,2)*t[i]);
    D_exp.set_type(d_matrix_type);
    v_complex=T*D_exp*c;
    fprintf(f_out1,"%lf %lf %lf %lf %lf %lf\n",t[i],x[i],y[i],
    H_scale*Re(v_complex(0)),Re(v_complex(1)),
    Re(v_complex(2)));
   }
 cout<<"fit finished"<<endl;
}
```